

Electronic Thesis and Dissertation Repository

---

12-9-2016 12:00 AM

## Static Magnetic Field Interactions of Medical Devices in The MRI Environment

Spencer Baird Parent, *The University of Western Ontario*

Supervisor: Dr. Blaine A. Chronik, *The University of Western Ontario*

A thesis submitted in partial fulfillment of the requirements for the Master of Science degree in Medical Biophysics

© Spencer Baird Parent 2016

Follow this and additional works at: <https://ir.lib.uwo.ca/etd>



Part of the [Other Physics Commons](#)

---

### Recommended Citation

Parent, Spencer Baird, "Static Magnetic Field Interactions of Medical Devices in The MRI Environment" (2016). *Electronic Thesis and Dissertation Repository*. 4347.  
<https://ir.lib.uwo.ca/etd/4347>

This Dissertation/Thesis is brought to you for free and open access by Scholarship@Western. It has been accepted for inclusion in Electronic Thesis and Dissertation Repository by an authorized administrator of Scholarship@Western. For more information, please contact [wlsadmin@uwo.ca](mailto:wlsadmin@uwo.ca).

## Abstract

**Background:** The current procedures and guidelines for testing medical devices require that conservative testing be carried-out using the “worst-case” device or device configuration for each interaction (force, torque, heating, et cetera) of importance, and the results of those tests be used to inform regulatory labeling for that device. One of the most difficult elements of carrying out the above procedure is the determination of what represents a “worst-case” device or device configuration. A simulation “pipeline” would enable a systematic procedure for identification of the worst-case device or device configuration for magnetic force from an otherwise impossibly large set of options.

**Methods:** Using a combination of computational and analytic methods, a comprehensive capacity to simulate and predict the static magnetic field interactions, specifically magnetic force, experienced by any medical device in any MRI-relevant environment is developed. This computational model is validated through comparison to derived analytic solutions and experimental testing performed in accordance to ASTM F2052-15.

**Results:** Through analytic validation, it is found that the computational model of magnetic force is ideal for use on materials with magnetic susceptibility less than  $10^4$  ppm, such as medical implant-grade metals. Experimentally, the computational model of force correctly predicted the force on two steels of magnetic susceptibility  $<10^4$  ppm within less than 1% difference than the current testing procedure.

**Conclusion:** The computational model of force is recommended for use in medical device testing applications as a way to identify what represents a “worst-case” device or device configuration.

## Keywords

Magnetic Resonance Imaging, Device Safety, Magnetic Force, Magnetic Susceptibility, COMSOL

## Co-Authorship Statement

The work presented in Chapter 2 has been submitted as an abstract to the International Society of Magnetic Resonance in Medicine (ISMRM).<sup>1</sup> It is the intention of the authors to publish this work. Parent led the research developing the computational model and deriving the analytic solution. Handler reviewed the analytic model. Drozd aided in solving the analytic model. Chronik was responsible for overall supervision of this research.

The work presented in Appendix E has been submitted as an abstract to the International Society of Magnetic Resonance in Medicine.<sup>2</sup> It is the intention of the authors to publish this work. Parent led the research, produced all scripts and simulations, and performed all analysis. Handler reviewed all scripts while providing suggestions on improvements that were crucial in the success of this research. McCurdy aided in the production of scripts to iteratively run the simulations in a pipeline, and scripts to visualize the data. Chronik was responsible for overall supervision of this research.

The work presented in Appendix F was accepted and presented as a poster at ISMRM 2016.<sup>3</sup> It is the intention of the authors to publish this work. Parent led the research, produced all scripts and simulations, and performed all analysis. Handler constructed the NMR probes, reviewed all scripts, and aided in the derivation of the field broadening equation. Chronik was responsible for overall supervision of this research.

---

<sup>1</sup> Parent, S., Handler, W., Drozd, J., & Chronik, B. A. (2017). Analytic Validation of a Computational Model of Magnetic Force in Linear Magnetic Materials. In *ISMRM*. (2683). Hawaii.

<sup>2</sup> Parent, S., Handler, W., McCurdy, C. M., & Chronik, B. A. (2017). Computational Analysis of Main Field Homogeneity in Presence of Non – Linear Magnetic Steel. In *ISMRM*. (2694). Hawaii.

<sup>3</sup> Parent, S., Handler, W., & Chronik, B. A. (2016). Investigation of systematic errors in NMR field probes. In *ISMRM*. (5936). Singapore.

## Acknowledgments

I would like to acknowledge my sincere gratitude to my supervisor Prof. Blaine Chronik for his guidance, support, encouragement, and for allowing me the opportunity to conduct research as a member of the xMR laboratory at Western University. I am grateful for the opportunities he has provided, the skills I have gained and the educational experience I received. The time spent in this lab under his supervision has been invaluable to my growth in both a personal and professional setting.

I would like to acknowledge Dr. William Handler. Although not an official thesis supervisor the work presented in this thesis would not be possible without his guidance, support, encouragement and overall patience. His mentorship throughout the course of this thesis has been a countless source of direction.

To my advisory committee, Drs. Tamie Poepping and Jean Théberge, for their time, suggestions and helpful advice.

I would like to acknowledge Colin McCurdy, Justin Peterson, Daniel Martire and all the members of the xMR lab for their help throughout this thesis.

To Frank van Sas and Brian Dalrymple for their assistance in machining the steel rods, and aid in constructing the NMR probes used in the completion of this thesis.

I wish to thank all my friends and family that pretended to know what I was talking about for the past two years.

I would like to acknowledge the following sources of funding: NSERC and MITACS.

## Table of Contents

<b>Abstract</b> .....	i
<b>Co-Authorship Statement</b> .....	ii
<b>Acknowledgments</b> .....	iii
<b>Table of Contents</b> .....	iv
<b>List of Figures</b> .....	viii
<b>List of Appendices</b> .....	xvii
<b>List of Abbreviations and Symbols</b> .....	xviii
<b>Chapter 1: Introduction</b> .....	1
1.1 Motivation .....	1
1.2 Medical Devices in the MR Environment.....	3
1.2.1 Medical Devices .....	3
1.2.2 Dangers in MRI .....	4
1.2.3 Medical Device Interactions .....	4
1.2.4 Classification of Medical Devices .....	6
1.2.5 Current Medical Device Testing.....	7
1.3 Physics of Electromagnetism .....	7
1.3.1 Fundamental Electromagnetic Concepts .....	8
1.3.2 Magnetic Susceptibility and Permeability .....	10
1.3.3 Magnetic Materials .....	11
1.3.4 Magnetic Force .....	15
1.4 Magnetic Resonance Imaging .....	16
1.4.1 Magnetic Resonance Imaging .....	16
1.5 MRI systems.....	17
1.5.1 Main Magnet.....	18
1.6 Computational Methods .....	21
1.7 Research Objectives and Thesis Organization .....	22
<b>Chapter 2: Methodology</b> .....	24
2.1 Computational Model of Magnetic Force .....	24
2.2 Analytic Validation of a Computational Model of Magnetic Force .....	25
2.3 Experimental Validation of a Computational Model of Magnetic Force.....	28
<b>Chapter 3: Results</b> .....	33
<b>Chapter 4: Discussion and Conclusion</b> .....	44
4.1 Analytic Validation .....	44

4.2 Experimental Validation .....	45
4.3 Conclusion.....	48
4.4 Future Work .....	49
<b>References .....</b>	<b>51</b>
<b>Appendix A: ASTM F2052-15 Magnetic Force Deflection Test.....</b>	<b>58</b>
<b>Appendix B: Derivation of Magnetic Force Equation.....</b>	<b>60</b>
<b>Appendix C: Certificates of Tests for Stainless Steel Rods.....</b>	<b>65</b>
<b>Appendix D: Measured Magnetic Field Data for 3T MRI System .....</b>	<b>69</b>
<b>Appendix E: Investigation of the Effects of Foreign Magnetic Materials Positioned Outside an MRI System on the Main Field Homogeneity of that System .....</b>	<b>70</b>
E.1 Magnet Design.....	71
E.1.1 Methods for Modeling of Helmholtz Coil .....	71
E.1.2 Methods for Modeling Actively Shielded MRI Magnet .....	72
E.1.3 Results for Modeling of Helmholtz Coil.....	72
E.1.4 Results for Modeling Actively Shielded MRI Magnet .....	75
E.2 Investigation of Main Field Homogeneity in Presence of Foreign Materials .....	77
E.2.1 Methods.....	77
E.2.2 Results .....	79
E.3 Discussion.....	85
E.4 Conclusion .....	88
<b>Appendix F: Investigation of Systematic Errors in NMR Field Probes .....</b>	<b>89</b>
F.1 Methods.....	91
F.1.1 Methods for Investigation of Effects due to the Susceptibility of Epoxy .....	92
F.1.2 Methods for Investigation of Effects Due to Voids Within the Epoxy .....	95
F.3 Discussion .....	100
F.4 Conclusion .....	101
<b>Curriculum Vitae .....</b>	<b>102</b>

## List of Tables

Table 1 – Specifications of the rods used in experimental tests of magnetic force as conducted with methods outlines in Appendix A. All rods have radius, $r=0.635$ cm. Data sheets for the steels are included in Appendix C. Magnetic susceptibility of the steels was not included in the data sheets and thus was unknown. Rod lengths were machined to the values listed in the table. ....	29
Table 2 – Experimental results of deflection test conducted for each of the four rods specified in the table, as conducted to methods outlines in Appendix A. All rods have radius, $r=0.635$ cm. Data sheets for the steels are included in Appendix C. Rod lengths were machined to the values listed in the table. Deflection test conducted at a 3T (Siemens Prisma) MRI system. Deflection angle was average over three trials of measurement. Magnetic susceptibility of the steels was not included in the data sheets and thus was unknown. ....	37
Table 3 – Experimentally calculated magnetic susceptibility, simulated value of magnetic force and percent difference between simulated value of magnetic force and experimental value of force for each of the four rods specified in the table. Magnetic susceptibility was calculated using the results of the deflection test listed in Table 2, the linear approximation to the magnetic flux density of the 3T calculated in 2.2.3 and equation (48). This value of $\chi$ was used in the computational model of force to produce the simulated magnetic force values presented in the table. The percent difference is the result of comparing these simulated values of force to the experimentally determined values of force in Table 2. ....	41
Table 4 – $B_z$ field as a function of $z$ down the center on axis line of a 3T MRI (Siemens Prisma) as measured by a Hall-effect magnetic field probe. $Z$ position is measured as the distance from the isocenter where the isocenter is defined as $z=0$ . Data points were measured with sample spacing of 10 mm. All uncertainties are estimated. ....	69

Table 5 - Specifications of the current carrying coils used to define a Helmholtz pair in a *COMSOL* simulation. The radius, number of turns, and current were arbitrarily chosen. Coil position was constrained such that the distance between the coils was equal to  $R$ . ..... 71

## List of Figures

Figure 1- Magnetic susceptibility ( $\chi$ ) spectrum. Magnetic susceptibilities range from  $-10^5$  ppm to  $\chi > 10^{11}$  ppm. Materials are classified as diamagnetic, paramagnetic or ferromagnetic based on where the magnetic susceptibility of the material lies on this spectrum. Approximate spectrum locations for water, titanium, stainless steel 304, and pure iron are shown. Materials are ferromagnetic if their susceptibility is greater than  $10^4$  ppm. Medical implant-grade metals such as stainless steel 316, cobalt-chromium alloys and titanium alloys all have  $\chi < 10^4$  [27], [29], [30], [43]–[45]. ..... 11

Figure 2 – An electron,  $-e$ , revolving around the nucleus at a radius  $R$ , with angular velocity  $\nu$ , can be viewed as steady state current,  $I = \frac{-e\nu}{2\pi R}$  which produces a magnetic moment  $\mathbf{m} = -\frac{1}{2}e\nu R\hat{\mathbf{z}}$ ..... 12

Figure 3 – An example B-H curve, showing the magnetic flux density,  $\mathbf{B}$ , as a function of magnetic field strength,  $\mathbf{H}$ , for a hypothetical material. In this case the magnetic flux density is a non-linear function of applied magnetic field and ‘saturates’ at 2 T. This is the point where further increase of the applied field will not result in a change in the magnetic flux density. .... 15

Figure 4 – A loop of current  $I$ , and radius  $R$ , centered upon the  $z$ -axis in Cartesian coordinates will produce a magnetic flux density  $\mathbf{B} = \frac{\mu_0 I}{2R}\hat{\mathbf{z}}$  at the center of the loop, and  $\mathbf{B}(\mathbf{z}) = \frac{\mu_0 I R^2}{2(R^2+z^2)^{3/2}}\hat{\mathbf{z}}$  along the  $z$  axis. .... 18

Figure 5 – A pair of current carrying loops of current  $I$ , and radius  $R$ , placed a distance  $R$  apart will produce a nearly homogeneous magnetic field in the center of the loops. With the current loops centered upon the  $z$ -axis in Cartesian coordinates, they will produce a magnetic flux density  $\mathbf{B} = \left(\frac{4}{5}\right)^{\frac{3}{2}}\frac{\mu_0 I}{R}\hat{\mathbf{z}}$  at the center of the loops and  $\mathbf{B}(\mathbf{z}) = \frac{\mu_0 I R^2}{2(R^2+(z-l)^2)^{3/2}}\hat{\mathbf{z}} + \frac{\mu_0 I R^2}{2(R^2+(z+l)^2)^{3/2}}\hat{\mathbf{z}}$  along the  $z$ -axis, where  $l$  is the distance between the coil and the  $z = 0$ ,  $x$ - $y$  plane..... 19

Figure 6 –  $\mathbf{B}(\mathbf{z})$  as a function of  $z$  for a pair of current carrying loops. Two coils of current carrying wire placed a distance  $R$  apart, centered upon the  $z$ -axis in Cartesian coordinates, will produce the above magnetic flux density profile along the  $z$  axis. Contributions to the total  $\mathbf{B}(\mathbf{z})$  from each coil are shown. The total resulting  $\mathbf{B}(\mathbf{z})$  is nearly homogenous in the center of the coils.  $X$ -axis normalized to radius size and  $y$ -axis normalized to the maximum value of  $\mathbf{B}(\mathbf{z})$  to generalize to any coil pair. .... 20

Figure 7 – Geometry of a cylinder position within a *COMSOL* simulation. A cylinder of radius  $r=1.27$  cm and length  $L$  was centered along the  $z$ -axis. The base of the cylinder is positioned at isocenter. The integration over the volume of this cylinder is thus  $\pi r^2 \int_0^L dz$ . .... 25

Figure 8 – Geometry of a rod position within a *COMSOL* simulation. A rod of radius  $r = 0.635$  cm and length  $L$  was centered along the  $z$  axis with the midpoint of the rod at a position of  $z = -0.8$  m. The integration over the volume of this cylinder is thus  $\pi r^2 \int_{-0.8-\frac{L}{2}}^{-0.8+\frac{L}{2}} dz$ . .... 32

Figure 9 - Magnetic force as a function of magnetic susceptibility,  $\chi$ , for a cylinder of radius 1.27 cm, and length 2.54 cm in a magnetic environment  $B_x = -0.5x \mathbf{T}$ ,  $B_y = 0$ ,  $B_z = 0.5z \mathbf{T}$ . Cylinder is positioned about the  $z$ -axis. Simulated results and analytic solution are shown.

Analytic solution is given by  $F_z = \frac{\chi(1+\chi)\pi r^2 \int_0^L z dz}{4\mu_0}$ ,  $F_x = F_y = 0$  where  $L$  is 2.54 cm. .... 33

Figure 10 – (Top) Percent error when simulated results are compared to an analytic solution for the magnetic force of a cylinder of radius 1.27 cm, and length 2.54 cm in a magnetic environment  $B_x = -0.5x \mathbf{T}$ ,  $B_y = 0$ ,  $B_z = 0.5z \mathbf{T}$  as a function of magnetic susceptibility,  $\chi$ .

Cylinder is positioned about the  $z$ -axis. Analytic solution is given by  $F_z = \frac{\chi(1+\chi)\pi r^2 \int_0^L z dz}{4\mu_0}$ ,

$F_x = F_y = 0$  where  $L$  is 2.54 cm. (Bottom) Axis limit of above plot is restricted to  $\chi < 10^4$  ppm as implant-

grade metals have values of susceptibility  $< 104$  ppm. .... 34

Figure 11 - Magnetic force as a function of cylinder length,  $L$  for a cylinder of radius 1.27 cm, and magnetic susceptibility 100 ppm in a magnetic environment  $B_x = -0.5x \text{ T}, B_y = 0, B_z = 0.5z \text{ T}$ . Cylinder is positioned about the  $z$ -axis. Simulated results and analytic solution are shown. Analytic solution is given by  $F_z = \frac{\chi(1+\chi)\pi r^2 \int_0^L z dz}{4\mu_0}$ ,  $F_x = F_y = 0$  where  $\chi$  is 100 ppm.

..... 35

Figure 12 - Percent error when simulated results are compared to an analytic solution for the magnetic force of a cylinder of radius 1.27 cm and magnetic susceptibility 100 ppm in a magnetic environment  $B_x = -0.5x \text{ T}, B_y = 0, B_z = 0.5z \text{ T}$  as a function of cylinder length,  $L$ .

Cylinder is positioned about the  $z$ -axis. Analytic solution is given by  $F_z = \frac{\chi(1+\chi)\pi r^2 \int_0^L z dz}{4\mu_0}$ ,

$F_x=F_y=0$  where  $\chi$  is 100 ppm. .... 36

Figure 13 – (Top)  $B_z$  field as a function of  $z$  down the center on axis line of a 3T MRI (Siemens Prisma) as measured by a Hall-effect magnetic field probe.  $Z$  position is measured as the distance from the isocenter where the isocenter is defined as  $z = 0$ . Data points were measured with sample spacing of 10 mm. Measured data table included in Appendix D. (Bottom)  $X$  axis shortened to only include data sampled at 10 mm. The region along  $z$  over which 10 cm rods are placed shown with vertical black lines. The region along  $z$  over which 2.54 cm rods are placed shown with vertical cyan lines. Error bars are too small to be seen. .... 38

Figure 14 – Linear approximation, as calculated in 2.2.3,  $B_{z,linear}(z) = (4.2 \text{ T/m})z + 5.6 \text{ T}$ , of the experimentally measured  $B_z$  field data.  $B_z$  field as a function of  $z$  down the center on axis line of a 3T MRI (Siemens Prisma) as measured by a hall effect magnetic field probe. Axis limited to

highlight approximate region over which the rods are placed.  $Z$  position is measured as the distance from the isocenter where the isocenter is defined as  $z = 0$ . Data points were measured with sample spacing of 10 mm. Measured data table included in Appendix D. Error bars are too small to be seen..... 39

Figure 15 – Difference when comparing the linear approximation,  $B_{z,linear}(z) = (4.2 \text{ T/m})z + 5.6 \text{ T}$ , to the experimentally measured  $B_z$  field data over the approximate region over which the rods are placed. The region along  $z$  over which 10 cm rods are placed shown with vertical black lines. The region along  $z$  over which 2.54 cm rods are placed shown with vertical cyan lines.  $B_z$  field as a function of  $z$  down the center on axis line of a 3T MRI (Siemens Prisma) as measured by a Hall-effect magnetic field probe.  $Z$  position is measured as the distance from the isocenter where the isocenter is defined as  $z = 0$ . Data points were measured with sample spacing of 10 mm. Measured data table included in Appendix D. Error bars are too small to be seen..... 40

Figure 16 – Magnetic force as calculated by an experimental deflection test as conducted to methods outlines in Appendix A, and simulation for two steels, 316 and 304, at two lengths per steel, 2.54 cm and 10 cm. Specifications of the rods are found in Table 1 and magnetic susceptibilities are found in Table 3. Deflection test conducted at a 3T (Siemens Prisma) MRI system. Simulation performed within computational model developed in 2.2.1. Error bars are omitted as the experimental value of magnetic force is used to calculate the magnetic susceptibility value used in the simulation. Any error present in the experiment is automatically present in the simulation. Error bars would thus be redundant when looking to compare the data sets..... 42

Figure 17 – Percent difference when comparing simulated value of magnetic force and experimental value of force two steels, 316 and 304, at two lengths per steel, 2.54 cm and 10 cm. Experimental value of magnetic force as calculated by an experimental deflection test as conducted to methods outlines in Appendix A. Specifications of the rods are found in Table 1

and magnetic susceptibilities are found in Table 3. Deflection test conducted at a 3T (Siemens Prisma) MRI system. Simulation performed within computational model developed in 2.2.1.... 43

Figure 18 - Force deflection test conducted for a 10 cm rod of 316 stainless steel in a 60-cm bore 3 T MRI system (Siemens Prisma). In this case, the 10 cm rod is suspended by a string at a location of 0.8 m from the isocenter of the system, and at a height of 0.3 m from the top of the bore (i.e. along the central axis of the system). The string is fixed to a protractor which is rigidly mounted to the test fixture with the  $0^\circ$  mark of the protractor oriented vertically. Magnetic force on the object is calculated based on the angle of deflection measured [11]. ..... 58

Figure 19 – Magnetic flux density along the  $x = 0, y-z$  plane for a simulation of a Helmholtz coil of radius 0.5 m, current 100 A, and 10 wire turns within *COMSOL*. Simulation computed using the ‘Magnetic Fields, mf’ package of *COMSOL* within a spherical infinite element domain. Arrows indicate direction of field. .... 73

Figure 20 – Magnetic flux density as a function of  $z$  for a Helmholtz coil of radius 0.5 m, current 100 A, and 10 wire turns. Analytic solution and *COMSOL* simulation results shown. The simulation data falls off as the data extends into the infinite element domain which begins at  $1.8 z/R$ . As the data moves into the infinite element domain it will exponentially decrease to 0. The horizontal axis is normalized to the coil radius and the vertical axis is normalized to the maximum value of  $\mathbf{B}(z)$ . .... 74

Figure 21 – Percent difference when comparing the magnetic flux density as a function of  $z$  for a simulated Helmholtz coil to an analytic solution of the same Helmholtz coil of radius 0.5 m, current 100 A, and 10 wire turns. The horizontal axis limits are truncated to  $1.5 z/R$  in order to remove data points within the infinite element region. As the data moves into the infinite element domain it will exponentially decrease to 0. Percent difference in this region gives no information. The horizontal axis is normalized to the coil radius and the vertical axis is normalized to the maximum value of  $\mathbf{B}(z)$ . .... 75

Figure 22 – Magnet flux density profile produced by a *COMSOL* model of a standard actively shielded MR main magnet. The magnet consisted of seven inner coils and an additional two outer shielding coils. The current was adjusted such that the main field had a value of 0.5T within 0.3 mT. Simulation computed using the ‘Magnetic Fields, mf’ package of *COMSOL* within a spherical infinite element domain. (Left) Magnetic flux density shown along the  $y = 0$ ,  $x$ - $z$  plane. (Right) Zoomed in to better visualize the magnet flux density profile within the ‘bore’ and coils. .... 76

Figure 23 – Magnet flux density along the  $z$ -axis for a *COMSOL* model of a the example actively shielded MR main magnet. The magnet consisted of seven inner coils and an additional two outer shielding coils of finitely winded coil. The current was adjusted such that the main field had a value of 0.5 T within 0.3 mT..... 76

Figure 24 - Geometry of a plate of thickness 4mm, and dimensions 3 m by 2.5 m added to the model of a seven coil actively shield MR scanner at a position of  $y = -1.0$  m within *COMSOL*. .... 78

Figure 25- An example B-H curve, showing the magnetic flux density,  $\mathbf{B}$ , as a function of magnetic field strength,  $\mathbf{H}$ , for a hypothetical material. In this case the magnetic flux density is a non-linear function of applied magnetic field and ‘saturates’ at 2 T. This is the point where further increase of the applied field will not result in a change in the magnetic flux density.....79

Figure 26 – Magnet flux density profile at the location of a steel plate placed 1 m below the isocenter of a standard actively shielded MR main magnet as produced by a *COMSOL* model. The magnet consisted of seven inner coils and an additional two outer shielding coils. The current was adjusted such that the main field had a value of 0.5 T within 0.3 mT. .... 80

Figure 27 – Magnet flux density profile at the location of a steel plate of magnetic susceptibility  $10^8$  ppm placed 1 m below the isocenter of a standard actively shielded MR main magnet as

produced by a *COMSOL* model. The magnet consisted of seven inner coils and an additional two outer shielding coils. The current was adjusted such that the main field had a value of 0.5T within 0.3 mT. Color axis has been limited to 0.2 T to observe magnetic flux density as the location of the plate..... 81

Figure 28 – Change in magnetic flux density in the  $x = 0$ ,  $Y-Z$  plane due to the presence of a linear magnetic plate of susceptibility: (top, left)  $10^8$  ppm, (top, right)  $10^7$  ppm, (bottom, left)  $10^5$ , (bottom, right) 10 ppm; at a distance of  $y = -1$  m to a standard actively shielded MR main magnet of field strength 0.5 T. Change in magnetic flux density calculated by subtracting the magnetic flux density results of the simulation without a plate from the simulation with a plate. .... 82

Figure 29 - Change in magnetic flux density in the  $z = 0$ ,  $X-Y$  plane due to the presence of a linear magnetic plate of susceptibility: (top, left)  $10^8$  ppm, (top, right)  $10^7$  ppm, (bottom, left)  $10^5$ , (bottom, right) 10 ppm; at a distance of  $y = -1$  m to a standard actively shielded MR main magnet of field strength 0.5 T. Change in magnetic flux density calculated by subtracting the magnetic flux density results of the simulation without a plate from the simulation with a plate. .... 83

Figure 30 - Change in magnetic flux density in the  $y = 0$ ,  $X-Z$  plane due to the presence of a linear magnetic plate of susceptibility: (top, left)  $10^8$  ppm, (top, right)  $10^7$  ppm, (bottom, left)  $10^5$ , (bottom, right) 10 ppm; at a distance of  $y = -1$  m to a standard actively shielded MR main magnet of field strength 0.5 T. Change in magnetic flux density calculated by subtracting the magnetic flux density results of the simulation without a plate from the simulation with a plate. .... 84

Figure 31 - Change in magnetic flux density due the presence of a non-linear magnetic plate. (top, left)  $z = 0$ ,  $X-Y$  plane (top, right)  $x = 0$ ,  $Y-Z$  plane (bottom)  $y = 0$ ,  $X-Z$  plane; at a distance of  $y = -1$  m to a standard actively shielded MR main magnet of field strength 0.5 T. Change in

magnetic flux density calculated by subtracting the magnetic flux density results of the simulation without a plate from the simulation with a plate..... 85

Figure 32 - Nuclear magnetic resonance (NMR) field probe. Field probe contains copper solenoids that wrap around glass vials filled with copper sulphate doped water samples. The sample and solenoid are held in place in an epoxy filled ellipsoid. (Left) Field probe shown with the copper solenoid leads exiting the epoxy ellipsoid that contains the solenoid and sample vial. (Right) NMR field probe cut in cross section showing the epoxy-filled region..... 91

Figure 33 – *COMSOL* geometry of three NMR probe designs. Within an epoxy ellipsoid: (from left to right) probe i) was modeled with a glass vial containing a sample of copper sulphate doped water, surrounded by a 4 turn copper solenoid of wire thickness 0.225 mm; probe ii) was modeled with only a glass vial containing a sample of copper sulphate doped water; probe iii) was modeled containing only a 4 turn copper solenoid with wire thickness 0.225 mm..... 93

Figure 34 – Sensitivity profile of a solenoid modeled within *COMSOL* along the  $z$ -axis. Sensitivity profile produced by solving for the magnetic flux density using Biot-Savart law at every data point with an elements array in *MATLAB*. Normalizing to the maximum magnetic flux density gives the sensitivity profile. This sensitivity profile was used to produce a weight,  $w_i$ , for each value of  $\mathbf{B}$  in the data set,  $x_i$ . ..... 94

Figure 35 – Path of an air bubble of spherical radius 1 mm moving along a circle of radius of 5 mm fixed in the  $z = 0$ ,  $X$ - $Y$  plane at an angle,  $\theta$ , within an NMR probe. *COMSOL* simulation computed for angles of  $0^\circ$ ,  $45^\circ$ ,  $90^\circ$ ,  $135^\circ$ ,  $180^\circ$ ,  $225^\circ$ , and  $270^\circ$ ..... 95

Figure 36 - Field broadening as a function of magnetic susceptibility of epoxy for the three NMR probe models modelled. Within an epoxy ellipsoid: Probe i) was modeled with a glass vial containing a sample of copper sulphate doped water, surrounded by a 4 turn copper solenoid; Probe ii) was modeled with only a glass vial containing a sample of copper sulphate doped

water; Probe iii) was modeled containing only a 4 turn copper solenoid. The value of magnetic susceptibility that resulted in a minimum field broadening is represented by a vertical black, blue and red line for probes i), ii) and iii) respectively..... 97

Figure 37 - Field offset as a function of magnetic susceptibility of epoxy for NMR Probe i). Within an epoxy ellipsoid, Probe i) was modeled with a glass vial containing a sample of copper sulphate doped water, surrounded by a 4 turn copper solenoid..... 98

Figure 38 – Resulting field broadening due to a void at various locations within a NMR probe. The NMR probe was modeled with a glass vial containing a sample of copper sulphate doped water, surrounded by a 4 turn copper solenoid, all encapsulated in epoxy ellipsoid (i.e. “Probe i”). (Top) Resulting field broadening due to spherical void of radius 1 mm moving along a circle of radius of 5 mm fixed in the  $z = 0$ ,  $X$ - $Y$  plane at an angle of  $0^\circ$ ,  $45^\circ$ ,  $90^\circ$ ,  $135^\circ$ ,  $180^\circ$ ,  $225^\circ$ , and  $270^\circ$ . (Bottom) Resulting field broadening due to the spherical void of radius 1 mm at different  $z$  positions while remaining fixed at a position of  $x = 5$  mm,  $y = 0$  mm in the  $X$ - $Y$  plane..... 99

Figure 39- Computer design of an array of nuclear magnetic resonance (NMR) field probes that make up an effective ‘field camera’ which is used to acquire accurate spatial variation of time varying fields in MR systems at discrete points in space. Seven probes can be seen here (6 around the circumference of the circle and one at the centre). ..... 101

## List of Appendices

<b>Appendix A: ASTM F2052-15 Magnetic Force Deflection Test</b> .....	58
<b>Appendix B: Derivation of Magnetic Force Equation</b> .....	60
<b>Appendix C: Certificates of Tests for Stainless Steel Rods</b> .....	65
<b>Appendix D: Measured Magnetic Field Data for 3T MRI System</b> .....	69
<b>Appendix E: Investigation of the Effects of Foreign Magnetic Materials Positioned Outside an MRI System on the Main Field Homogeneity of that System</b> .....	70
E.1 Magnet Design.....	71
E.1.1 Methods for Modeling of Helmholtz Coil .....	71
E.1.2 Methods for Modeling Actively Shielded MRI Magnet .....	72
E.1.3 Results for Modeling of Helmholtz Coil.....	72
E.1.4 Results for Modeling Actively Shielded MRI Magnet .....	75
E.2 Investigation of Main Field Homogeneity in Presence of Foreign Materials .....	77
E.2.1 Methods.....	77
E.2.2 Results .....	79
E.3 Discussion.....	855
E.4 Conclusion .....	88
<b>Appendix F: Investigation of Systematic Errors in NMR Field Probes</b> .....	89
F.1 Methods.....	911
F.1.1 Methods for Investigation of Effects due to the Susceptibility of Epoxy .....	922
F.1.2 Methods for Investigation of Effects Due to Voids Within the Epoxy .....	95
F.3 Discussion .....	100
F.4 Conclusion .....	101

## List of Abbreviations and Symbols

$a$	Vector area
ASTM	ASTM International
$B$	Magnetic flux density
$B_m$	Magnetic flux density due to a magnet moment $m$
$B_M$	Magnetic flux density due to magnetization $M$
$E$	Electric field
$e$	Elementary charge
FDA	Food and Drug Administration
FEM	Finite element method
FID	Free induction decay
$g$	Acceleration due to gravity
$H$	Magnetic field strength
$h$	Height
$\hbar$	Plank's constant
$I$	Current
IEC	International Electrotechnical Commission
$J$	Electric Current density
$L$	Length
$m$	Magnetic Moment
$m_e$	Electron mass
$M$	Magnetization
MRI, MR	Magnetic resonance imaging, Magnetic resonance
$n$	Number of turns
$N$	Torque
NMR	Nuclear magnetic resonance
PDE	Partial differential equation
ppm	Parts per million
$r, R$	Radius
$r'$	Distance to $dI$

RF	Radiofrequency
$S(t)$	Signal as a function of time (t)
$s_w^2$	Weighted variance
T1	Longitudinal relaxation time
$V$	Volume
$v$	Angular velocity
$w_i$	Weight
$x_i$	Value of $\mathbf{B}$ in a data set
$\bar{x}_w$	Weighted mean
$\rho$	Electric charge density
$\epsilon_0$	Permittivity of free space
$\mu$	Magnetic permeability
$\mu_0$	Permeability of free space
$\mu_r$	Relative magnetic permeability
$\chi$	Volume magnetic susceptibility
$\sigma$	Field broadening

## Chapter 1: Introduction

This chapter introduces the problem posed by the presence of implanted medical devices in patients who would need a Magnetic Resonance Imaging (MRI) procedure at some point in their lives. The basic interactions that implanted devices can have with a MRI system are reviewed. Although there are multiple interactions between devices and MRI systems, this thesis is focused on the interactions between a device and the static magnetic field of the MRI magnet, and more specifically, the magnetically-induced forces experienced by devices in the vicinity of an MRI system. Some fundamentals of electromagnetism and magnetic material properties in the presence of static electromagnetic fields will be reviewed as they largely govern the interactions of interest. A brief overview of very simple models of MRI magnet systems is included, and a short description of the computer simulation tools used in thesis provided. This chapter concludes with a statement of the research objectives of this thesis and explanation of the thesis structure and format.

### 1.1 Motivation

Magnetic Resonance Imaging (MRI) is a widely used imaging modality with millions of MR exams conducted globally every year. Canadians received over 1.7 million MR exams in 2012 alone [1]. The effects of cumulative exposure to strong, static, magnetic fields present in MRI have been studied extensively and have been shown not to have hazardous effects in the absence of foreign materials [2].

It is, however, increasingly common for patients to have permanently implanted medical devices, and there are millions of individuals receiving permanently or semi-permanently implanted medical devices each year [3]. This represents a particular challenge if and when those patients ever require an MRI. Just as one classic example of this, there were over 370,000 implants of cardiac systems (i.e. pacemakers and implantable cardioverter defibrillators, ICDs) in the United States in 2003, and over 135,000 implants of cardiac systems in Canada in 2006 [3], [4]. With 50 to 75% of these individuals expected to be referred to an MRI over the lifetime of the device, patients with medical devices who require an MR exam must rely on the judgement of local MR technical staff and the labeling provided by device manufacturers [3], [5], [6]. Because only a

fraction of medical devices have been officially tested to determine the conditions under which they can be safely used within an MRI, the presence of any medical device creates a potential barrier to patients in need of an MRI [7]. This effectively results in a lower standard of care for subjects with implanted medical devices. In fact, in the United States in 2004 alone, it is estimated that 200,000 patients were denied an MRI due to the presence of implanted cardiac systems [3].

The basic reason that implanted medical devices represent a barrier to receiving MRI is fundamentally very simple: many devices when within the MR environment can present a danger to the subject, and/or interfere with the normal operation of the MR scanner [8], [9]. Devices can experience forces, torques, heating, vibration, and (for devices with active function) operational failure [9], [10]. The presence of devices can interfere with the MR scanner by causing image artefacts or noise in the images [11], [12]. The increased need for implantable medical devices, coupled with the increased use of MRI, creates a major need to understand and systematically investigate the safety of devices in the MRI environment.

The current procedures and guidelines for testing medical devices generally require that conservative testing be carried-out using the “worst-case” device or device configuration for each interaction (force, torque, heating, et cetera) of importance, and the results of those tests be used to inform regulatory labeling for that device [13]. One of the most difficult elements of carrying out the above procedure is the determination of what represents a “worst-case” device or device configuration. If the device is very simple, it may be trivial to identify which device to test. For example, if the device is available in only two materials, one of which is plastic and the other a highly-magnetic material, it is a simple matter of testing the “magnetic version” for the related interactions [14]. However, in most cases “devices” are in fact a family of multiple configurations, materials, and components, and there may be literally thousands (or more) of possible scenarios to test [15]. It is not practical to physically test all the scenarios, or even a large fraction of them. In these circumstances, one approach is to use an efficient, systematic, validated computer simulation to model a large fraction (if not all) of the configurations for a device for the interaction of interest, and through that process identify a small number or possibly a single configuration as the “worst-case”, and have only those configurations proceed to physical testing. It is the primary goal of this thesis to develop such a computer simulation

capability or “pipeline” for modeling the magnetic force experienced by any medical device, and thereby enable more comprehensive, and at the same time more practical, evaluation of devices for this interaction. This simulation capacity must have the ability to include an arbitrary MR magnet system, arbitrary device/material/configurations, and arbitrary positioning of the device within the MR magnet.

## 1.2 Medical Devices in the MR Environment

This thesis discusses the safety of medical devices in the MR environment. This section will provide some background on medical devices, their interactions in the MR environment, and their current testing standards and procedures.

### 1.2.1 Medical Devices

There are many possible definitions of a “medical device”, so it is important to be clear what is meant in the context of the thesis. In this thesis we are interested in the consideration of any device or system within the MRI environment that is not part of the “normal” MR system. The major groups of technology that fall under this broad definition would include:

- permanently or semi-permanently implanted medical devices (e.g. orthopedic implants, trauma fixation devices, cardiac pacemakers, drug pumps, neurostimulators, dental implants, vascular stents, cochlear implants);
- physiological monitoring devices (EEG, ECG, blood-pressure monitoring, laparoscopes);
- non-MR-based imaging or therapy modalities (PET, SPECT, x-ray, ultrasound, radiotherapy);
- MR-guided interventional systems (surgical robotics, biopsy guidance systems, HIFU);
- stimulus presentation and monitoring systems (visual goggles, optical and infrared cameras)[16].

At first glance, this appears impossibly broad. But the unifying factor in the evaluation and testing of this huge range of technology is the MRI exposure environment itself. In terms of magnetic force in particular, it is the consideration of the underlying material composition and

geometry of the devices in combination with the main magnetic field of the scanner that determines the interaction [17].

## 1.2.2 Dangers in MRI

When compared to other imaging modalities, the dangers of MRI are quite low. Since the introduction of MRI as a clinical modality, more than 100,000,000 diagnostic procedures have been completed with few major incidents, and many of those incidents were the apparent result of failure to follow safety guidelines or of the use of inappropriate or outdated information related to the safety aspects of medical devices [18], [15]. These major incidents include seven deaths [2], [19]–[21]. One death occurring when an oxygen tank became a projectile due to the magnetic force the tank experienced, fatally striking a boy in the head [19]; one patient experienced an acute intracerebral hemorrhage in the MR unit, with a fatal outcome due to the presence of a ferromagnetic aneurysm clip [20], [21]; and five additional deaths occurring, possibly due to inadvertently scanning patients with cardiac pacemakers [2]. In addition to these fatal accidents, several patients have experienced heating burns due to medical device heating, and in one case, the presence of a foreign body has caused unilateral blindness after an MR exam [22]–[24]. Beyond these major incidents however, 52% of MRI facilities responding to a survey in 1999 reported the occurrence of a MRI-related accident [19]. Although the effects of cumulative exposure to strong, static, magnetic fields present in MRI have been studied extensively and have shown no hazardous effects in the absence of foreign materials, medical devices, which fall into this category of foreign materials, pose an associated safety risk [2]. This risk is mitigated with medical device testing and the classification of medical devices.

## 1.2.3 Medical Device Interactions

As noted above, medical devices within the MR environment can present a danger to the subject, and/or interfere with the normal operation of the MR scanner due to several interactions between the device and the MR system [8], [9]. The interactions between a device and the MR system are complicated, and extensive testing and analysis is required in order to determine the conditions for which the device can be safely used [25]. When a passive medical device is within the MR system environment it can: experience heating from the radiofrequency (RF) electromagnetic fields [10], [26]–[30]; experience force and torque due to the strong static magnetic fields of the

main magnet and quickly varying magnet fields of the temporally and spatially varying gradients [10], [26], [29]–[33], [11]; and can cause distortions in images due to field inhomogeneities around the device [10], [26], [29], [30], [11].

Device heating is caused primarily by the RF field, a rapidly varying (10's to 100's of MHz) electromagnetic field with a magnetic field component applied perpendicularly to the static magnetic field for imaging purposes. The RF field deposits power in the human body even under normal circumstances (no device present), quantified by the specific absorption rate (SAR), measured in W/kg [16]. When a conducting medical device is present, the interactions are much stronger and the RF field can induce significant current flow in the device which can cause device heating [10], [26]–[30]. Medical devices can also cause increased electric fields around the device, leading to higher levels of SAR; causing heating in patient tissue in the vicinity of the device [30]. Heating is also caused by the gradient magnetic fields, which are spatially and temporally varying (kHz frequency range) magnetic fields used in imaging, applied along (alone or in combination)  $x$ -,  $y$ - and  $z$ -axes. These time varying gradient fields can also induce currents within medical devices, which also causes device heating [10], [29], [34]. RF heating is most prominent in long, extended devices which are of a resonant length for the RF frequency used. Gradient heating is more significant in devices with significant cross-sectional area, and there is no significant resonant effect [10].

Magnetic force and torque are interactions caused by the static field of the MR systems, although gradient fields can also cause torque and vibration via forces on induced eddy currents [10], [26], [29]–[33], [11], [35]. Torque will tend to align the long axis of a medical device along the direction of the static magnetic field and force will tend to pull magnetic materials present in the MR environment towards the scanner [10], [36]. Since this thesis focuses on static magnetic field interactions, specifically magnetic force, magnetic force is described in detail in section 1.3.4.

Medical devices can also cause image distortions due to field inhomogeneities around the device [10], [26], [29], [30], [11]. Medical devices composed of materials with non-zero magnetic susceptibility (see 1.3.2) can distort the local magnetic field surrounding the device [11], [17]. These field inhomogeneities then cause image distortions due to various processes of MR imaging that are beyond the scope of this thesis [37], [38]. The extent and nature of the image distortions are highly dependent on the specific imaging sequence employed.

The interactions itemized in the above paragraphs are in practice very complicated. Interactions between a device and an MR system depend on magnetic environment which is unique and dependent on the scanner, field strength, field uniformity; the pulse sequence, sequence type (gradient echo versus spin echo, et cetera), sequence parameters (bandwidth, flip angle, et cetera) and the device [10]. When considering a device, the composition, geometry, and orientation all play a large role in the resulting interactions. Medical device composition affects the interactions as different materials will have different magnetic, electrical, mechanical, and thermal properties that cause unique heating, magnetic force, torque and image distortion [12]. Device geometry is important as certain geometries can cause increases in heating and torques. Additionally, orientation within the magnetic environment is important as exposure to RF and gradient fields as well as the magnitude of the static field are all spatially dependent and thus depend on orientation. This thesis will focus on examining the static magnetic field interactions, specifically magnetic force, experienced by medical devices in the MRI environment. Some consideration is made of purely field-uniformity effects caused by magnetic materials, and these are presented in Appendices E and F because they are not complete and they are tangential to the primary theme and objectives of the thesis.

## 1.2.4 Classification of Medical Devices

The safety of a medical device in the MR environment must be determined, and afterwards marked as MR Safe, MR Conditional, or MR Unsafe. These classifications are defined as:

- MR Safe - an item that poses no known hazards resulting from exposure to any MR environment. MR Safe items are composed of materials that are electrically nonconductive, nonmetallic, and nonmagnetic.
- MR Conditional - an item with demonstrated safety in the MR environment within defined conditions. At a minimum, address the conditions of the static magnetic field, the switched gradient magnetic field and the radiofrequency fields. Additional conditions, including specific configurations of the item, may be required.
- MR Unsafe - an item which poses unacceptable risks to the patient, medical staff or other persons within the MR environment [13].

In the context of the above terminology, this thesis is primarily related to MR Conditional devices. Physical testing of worst-case devices (which would be identified using the simulation procedures described in the following chapters) for magnetic force would allow for determination of the conditions (if any) under which a given device or group of devices could be safely used within a MRI system or scanner.

## 1.2.5 Current Medical Device Testing

Presently, the Food and Drug Administration (FDA) and the International Electrotechnical Commission (IEC) recommends medical device testing be performed in accordance to test standards developed and published by ASTM International (ASTM) [25]. ASTM was formally an acronym for “American Society for Testing and Materials”, but is now simply “ASTM”. These documents can be found on the ASTM website [39]. Force and torque measurements are to be conducted according to ASTM F2052-15 (“Measurement of Magnetically Induced Displacement Force on Medical Devices in the Magnetic Resonance Environment”) and ASTM F2213-06 (“Measurement of Magnetically Induced Torque on Medical Devices in the Magnetic Resonance Environment”), respectively [40], [41]. All testing of image artifacts caused by the presence of medical devices is conducted according to F2119-07 (“Evaluation of MR Image Artifacts from Passive Implants”) [42]. Heating of medical devices is tested in accordance to ASTM F2128-11a (“Measurement of Radio Frequency Induced Heating On or Near Passive Implants During Magnetic Resonance Imaging”) [43]. Since this thesis seeks to evaluate the static magnetic field interactions, specifically magnetic force, the most important of the above test standards is ASTM F2052-15. For this reason, the device testing procedure for ASTM F2052-15 has been summarized and included as Appendix A.

## 1.3 Physics of Electromagnetism

This sub-chapter will provide the necessary fundamentals of electromagnetics required for an understanding of magnetic fields, magnetic materials, and magnetic forces. Concepts and equations discussed in this sub-chapter can be found in more detail in David J. Griffiths’ *Introduction to Electrodynamics*’ third edition [44].

### 1.3.1 Fundamental Electromagnetic Concepts

When discussing magnetic fields, it is important to distinguish between  $\mathbf{B}$  and  $\mathbf{H}$ .  $\mathbf{B}$ , the magnetic induction - or more commonly referred to as the magnetic flux density - is given in units of Tesla.  $\mathbf{H}$ , the magnetic field strength, is the strength of the magnetic field given in  $A/m$ . The difference between  $\mathbf{B}$  and  $\mathbf{H}$  is subtle, but important when discussing electromagnetics.  $\mathbf{B}$  is the total magnetic field contribution from the magnetic field, plus induced magnetization. A constitutive relation, the relation between two physical quantities that is specific to a material, is used to relate the  $\mathbf{H}$  and  $\mathbf{B}$  fields. The constitutive relation between  $\mathbf{H}$  and  $\mathbf{B}$  is given by equation (1) where  $\mu_0$  is the permeability of free space and  $\mathbf{M}$  is the magnetization, which is defined in equation (10).

$$\mathbf{B} = \mu_0(\mathbf{H} + \mathbf{M}) \quad (1)$$

#### *Maxwell's Equations*

Maxwell's equations are the foundation of classical electrodynamics, and thus are included, in differential form, for completeness.

$$\nabla \cdot \mathbf{E} = \frac{\rho}{\epsilon_0} \quad (2)$$

$$\nabla \cdot \mathbf{B} = 0 \quad (3)$$

$$\nabla \times \mathbf{E} = -\frac{\partial \mathbf{B}}{\partial t} \quad (4)$$

$$\nabla \times \mathbf{B} = \mu_0 \left( \mathbf{J} + \epsilon_0 \frac{\partial \mathbf{E}}{\partial t} \right) \quad (5)$$

$\mathbf{E}$  is the electric field,  $\rho$  is the electric charge density,  $\epsilon_0$  is the permittivity of free space, and  $\mathbf{J}$  is the electric current density.

#### *Biot-Savart law and Ampère's Law*

A steady line current will produce a static magnetic field. The magnetic flux density produced by a steady current,  $I$ , is given by the Biot-Savart law:

$$\mathbf{B}(\mathbf{r}) = \frac{\mu_0 I}{4\pi} \int \frac{d\mathbf{l} \times \mathbf{r}'}{|\mathbf{r}'|^3} \quad (6)$$

where  $d\mathbf{l}$  is an infinitesimal length of current,  $\mathbf{r}'$  is the displacement vector from  $d\mathbf{l}$  to the point at which the field is calculated,  $\mathbf{r}$ , and the integration is along the closed current path in the direction of flow. As an extension of the Biot-Savart law, for problems with sufficient symmetry, the magnetic flux density can also be solved for using Ampère's law.

$$\nabla \times \mathbf{B} = \mu_0 \mathbf{J} \quad (7)$$

$$\oint \mathbf{B} \cdot d\mathbf{l} = \mu_0 I_{enc} \quad (8)$$

In equation (8),  $I_{enc}$  is the total current enclosed by the integration path. This integration path is any loop that encloses the current,  $I_{enc}$ , exactly once.

### *Magnetic Moment and Magnetization*

A current not only produces a magnetic field, it induces a magnetic dipole moment,  $\mathbf{m}$ .

$$\mathbf{m} = I \int d\mathbf{a} = I\mathbf{a} \quad (9)$$

In equation (9),  $\mathbf{a}$  is the vector area. For a flat loop,  $\mathbf{a}$  is the ordinary area enclosed, with the direction assigned by the right hand rule where the fingers point in the direction of the current.

The integration is over the enclosed area with the normal in the direction of  $\mathbf{a}$ . [44]

The sum of all the magnetic moments,  $\sum \mathbf{m}$ , in a given homogeneous volume,  $V$ , allows the definition of magnetization as the volume density of magnetic moments, per equation (10) below.

$$\mathbf{M} = \frac{\sum \mathbf{m}}{V} \quad (10)$$

### 1.3.2 Magnetic Susceptibility and Permeability

Magnetic susceptibility,  $\chi$ , is the dimensionless proportionality constant that indicates the degree to which a material will become magnetized in response to an applied magnetic field.

$$\mathbf{M} = \chi\mathbf{H} \quad (11)$$

The magnetic susceptibility defined above is more specifically the volume magnetic susceptibility. Magnetic susceptibility can also be specified in terms of mass magnetic susceptibility, measured in  $m^3/kg$ , and molar magnetic susceptibility, measured in  $m^3/mol$ . Within this thesis, unless specifically noted otherwise, magnetic susceptibility will refer to volume magnetic susceptibility.

Magnetic susceptibility can also be discussed in terms of magnetic permeability,  $\mu$ ,

$$\mu = \mu_0(1 + \chi) \quad (12)$$

or relative magnetic permeability,  $\mu_r$ .

$$\mu_r = \frac{\mu}{\mu_0} \quad (13)$$

Magnetic permeability is discussed as the measure of the ability of a material to support the formation of a magnetic field within itself. The use of magnetic susceptibility is favoured when discussing magnetization,  $\mathbf{M}$ , and magnetic field strength,  $\mathbf{H}$ , as seen in equation (11). The use of magnetic permeability is preferred when relating magnetic flux density to magnetic field strength, as shown in equation (15).

$$\mathbf{B} = \mu\mathbf{H} \quad (15)$$

Magnetic susceptibility is also useful when discussing the classification of magnetic materials.

### 1.3.3 Magnetic Materials

All materials can be classified as diamagnetic, paramagnetic or ferromagnetic. For example, water is diamagnetic, titanium and non-magnetic stainless steels are paramagnetic, and pure iron is ferromagnetic [38], [44], [45]. This classification is based on a material's magnetic susceptibility, see Figure 1. For example, medical implant-grade metals such as stainless steel 316, cobalt-chromium alloys and titanium alloys all approximately have  $\chi < 10^4$  ppm [17], [38], [12], [45], [46], which classifies them as paramagnetic.

There are several ways to measure magnetic susceptibility including measuring the magnetic force on a material [47]–[49]; measuring the change in nuclear magnetic resonance signal of a reference sample in the presence of the material [47], [50], [51]; and measuring changes in magnetic field due to the presence of a material using superconducting quantum interference devices (SQUIDs) [47], [52]. Details of the multiple techniques for determining magnetic susceptibility are outside the scope of the work but can be found in references [12], [47]–[52].

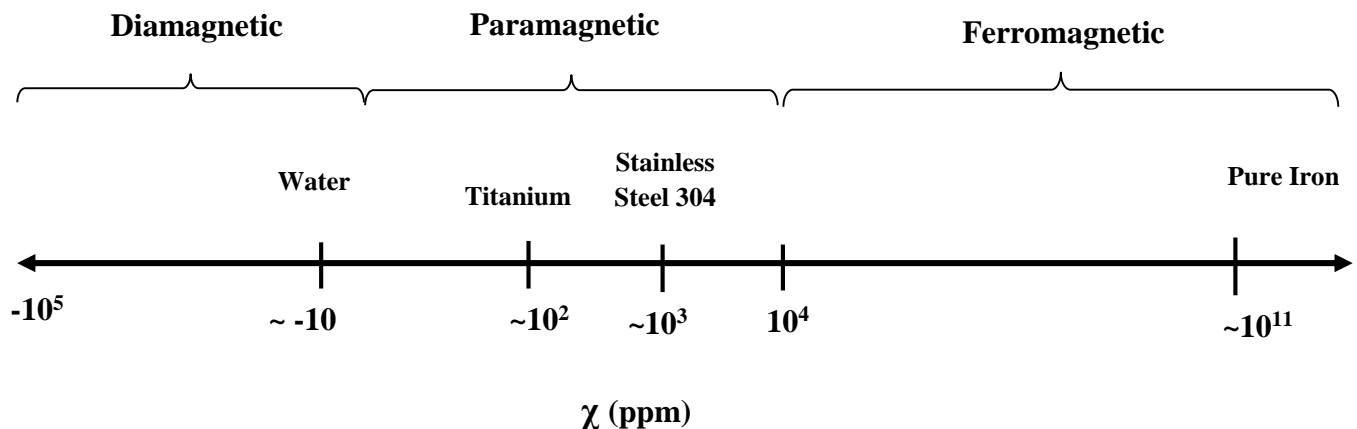


**Figure 1-** Magnetic susceptibility ( $\chi$ ) spectrum. Magnetic susceptibilities range from  $-10^5$  ppm to  $\chi > 10^{11}$  ppm. Materials are classified as diamagnetic, paramagnetic or ferromagnetic based on where the magnetic susceptibility of the material lies on this spectrum. Approximate spectrum locations for water, titanium, stainless steel 304, and pure iron are shown. Materials are ferromagnetic if their susceptibility is greater than  $10^4$  ppm. Medical implant-grade metals such as stainless steel 316, cobalt-chromium alloys and titanium alloys all have  $\chi < 10^4$  [17], [38], [12], [44]–[46].

Materials that are diamagnetic form no permanent magnet dipoles in the absence of an externally applied magnetic field. Any induced magnetic dipole moments are anti-parallel to the initial applied magnetic flux density,  $\mathbf{B}_0$ , where  $\mathbf{B}_0$  is applied along the  $z$  direction of Cartesian coordinates for the purposes of this thesis. Since  $\mathbf{B}_m$ , the magnetic flux density produced by the magnetic dipole moments, is anti-parallel to  $\mathbf{B}_0$ , overall magnetic flux density,  $\mathbf{B}$ , within the material is reduced. A simple classical model for diamagnetism can be obtained by considering electrons as “revolving” around the nucleus in a way that can be viewed as steady state current

$$I = \frac{-ev}{2\pi R} \quad (16)$$

where  $-e$  is the charge of an electron,  $v$  is the angular velocity, and  $R$  is the radius of electron orbit; see Figure 2.

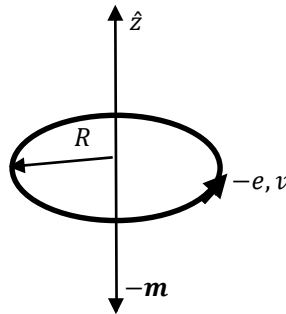


**Figure 2** – An electron,  $-e$ , revolving around the nucleus at a radius  $R$ , with angular velocity  $v$ , can be viewed as steady state current,  $I = \frac{-ev}{2\pi R}$  which produces a magnetic moment  $\mathbf{m} = -\frac{1}{2}evR\hat{\mathbf{z}}$ .

The dipole moment is then given by equation (17).

$$\mathbf{m} = -\frac{1}{2}evR\hat{\mathbf{z}} \quad (17)$$

When placed in a magnetic field,  $\mathbf{B}_0$ , the dipole moment experiences a torque, and the speed at which the electron revolves changes - thus its dipole moment changes. This change is opposite to the direction of  $\mathbf{B}_0$ . This change is shown in equation (18), where  $m_e$  is the mass of the electron.

$$\Delta \mathbf{m} = -\frac{e^2 R^2}{4m_e} \mathbf{B}_0 \quad (18)$$

Diamagnetism is mostly observed in materials with an even number of electrons, since this effect is much weaker than the mechanism for paramagnetism.

Materials that are paramagnetic form weak permanent magnet dipoles such that  $\mathbf{m} = 0$ ,  $\mathbf{B}_m = 0$ . However, when placed in an external magnetic field,  $\mathbf{m}$  align such that  $\mathbf{B}_m > 0$ , and enhances  $\mathbf{B}_0$  such that magnetization is linear to  $\mathbf{B}_0$ , and  $\mathbf{B} = \mathbf{B}_0 + \mathbf{B}_m$ .

Paramagnetism is the result an odd number of electrons. From a simplistic classical perspective, the unpaired electron is subject to magnetic torque. The spin of the unpaired electron creates a magnetic dipole, given by equation (19), where  $\hbar$  is Planck's constant.

$$\mathbf{m}_s = \frac{e\hbar}{2m_e} \hat{\mathbf{z}} \quad (19)$$

If placed in an external magnetic field this magnetic dipole moment will experience a torque,  $\mathbf{N}$ .

$$\mathbf{N} = \mathbf{m} \times \mathbf{B} \quad (20)$$

The torque is such that the dipole is aligned parallel with the field. Paramagnetism is only observed in atoms with an odd number of electrons as the Pauli Exclusion Principle dictates that the electrons within an atom pair together with opposing spins - neutralizing the torque on the combination. It is also important to note that the alignment is not complete due to random thermal collisions which tend to disrupt the alignment.

Like paramagnetism, materials that are ferromagnetic form permanent magnet dipoles. However, there is a much stronger alignment of magnetic dipoles such that the field inside ferromagnetic

materials can be on the order of  $10^4$  times stronger than  $B_0$  and the magnetization remains when the applied field is removed.

Ferromagnetism is also the result of the spin of unpaired electrons. However, unlike paramagnetism, each dipole tends to point in the same direction as its neighbor and results in a near 100% alignment. This occurs in domains, relatively small patches in the material containing billions of dipoles, and although dipoles line up within domains, domains themselves are randomly oriented. The longer a ferromagnetic is left in an applied field, the larger the domains parallel to the applied field grow as these domains expand and 'take over' less favorable domains which are unaligned. If the field is strong enough, one domain takes over entirely. Because of this behavior, ferromagnetic materials follow a hysteresis, that is, the relationship between  $B_0$  and  $M$  depends on the material's magnetic history. This is due to the fact that the magnetic dipoles will remain aligned even after  $B_0$  is reduced to 0.

A  $B$ - $H$  curve, see Figure 3, is a plot used to show the relationship between magnetic flux density and magnetic field strength for a given material. A linear magnetic material will have a linear relationship between  $B$  and  $H$ , whereas a non-linear magnetic material will not. It is important to note that ferromagnetic materials do not have a linear relationship between  $B$  and  $H$ , and thus the magnetic susceptibility of a ferromagnetic material is a function of the applied magnetic field. Additionally, all materials will have a 'saturation' point where further increase of the applied field will not result in a change in the magnetic flux density.

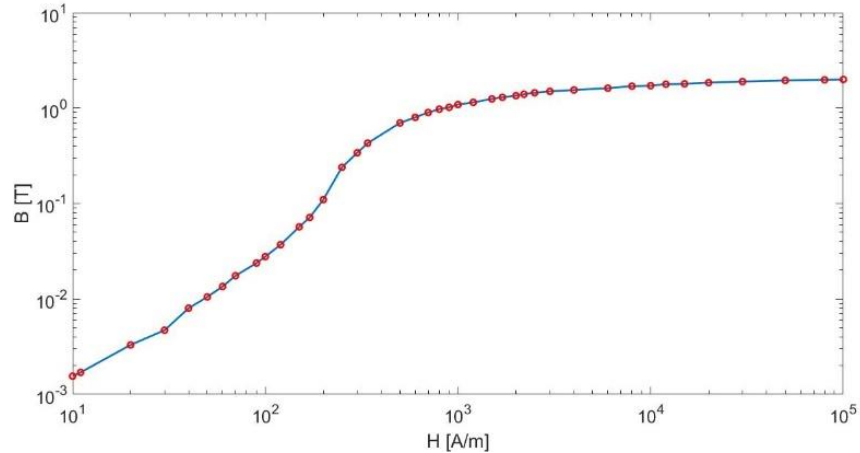


**Figure 3** – An example B-H curve, showing the magnetic flux density,  $\mathbf{B}$ , as a function of magnetic field strength,  $\mathbf{H}$ , for a hypothetical material. In this case the magnetic flux density is a non-linear function of applied magnetic field and ‘saturates’ at 2 T. This is the point where further increase of the applied field will not result in a change in the magnetic flux density.

### 1.3.4 Magnetic Force

When a magnetic material is exposed to a spatial gradient of a magnetic field it will experience a force. In the context of this thesis, this is the force experienced by a medical device when exposed to the spatial gradient of the main magnetic field of a superconducting MRI magnet. For paramagnetic materials, this force is proportional to both the magnitude of the local magnetic field and the local spatial gradient of that field, equation (21) [53], [54]. In MRI systems, force is typically greatest within the highly inhomogeneous field region at the entrance of the bore of the scanner [36].

$$\mathbf{F} = (\mathbf{m} \cdot \nabla) \quad (21)$$

In general the force on a magnetic dipole moment is described in Chapter 6 of [44], p.258, equation (6.3), as

$$\mathbf{F} = \nabla(\mathbf{m} \cdot \mathbf{B}) \quad (22)$$

which has been cited to be the same as equation (21) when  $\mathbf{J} = \frac{\partial \mathbf{E}}{\partial t} = 0$  [55]. This equivalence does not apply when the magnet moment is spatially dependent, as it is in the case of magnetized materials. This is included in Appendix B with a full derivation of equation (21). In the case where the magnet moment is spatially dependent, as it will be for the entirety of this thesis, equation (21) should be used.

## 1.4 Magnetic Resonance Imaging

This sub-chapter will provide a very brief overview of MRI. Since this thesis does not directly pertain to imaging, but rather focuses on the magnetic environment, detailed discussions of MRI including imaging acquisition, spin relaxation, pulse sequences, etc., will be omitted and can be found in detail in E. Mark Haacke, et al. ‘*Magnetic Resonance Imaging: Physical Principles and Sequence Design*’ [56].

### 1.4.1 Magnetic Resonance Imaging

Magnetic Resonance Imaging is a non-invasive, high-resolution imaging modality used for its lack of ionizing radiation, excellent soft tissue contrast, and multi-planar imaging capabilities [57]. MRI is capable of capturing both anatomical and functional information from intact biological systems. Images in MRI are possible due to signal acquired from nuclear magnetization when in the presence of a strong, static, spatially-uniform, external magnetic field [56]. The signal acquired,  $S(t)$ , is proportional to the initial magnetization  $M_0$  produced by the sum of these magnetic moments, and proportional to the rate at which that net magnetization precesses after being exposed to a radiofrequency pulse of magnetic field [56]. Because the rate of precession is itself proportional to the main magnetic field, and the net magnetization is also proportional to the main magnetic field strength, the signal magnitude is proportional to the main field strength squared; equation (23) [56].

$$S(t) \propto \mathbf{B}^2 \quad (23)$$

The noise associated with the MR signal also increases with increasing magnetic field, and for clinical MRI systems the noise is approximately proportional to the field; therefore, the signal-to-noise-ratio (SNR) is approximately proportional to the field strength [57]. In order to achieve more SNR, MR systems are naturally driven to implement the use of stronger static magnetic fields. Clinical MR systems vary in magnetic field strength from low field 0.2 T to high field 3 T systems. Research MR systems can achieve fields of 7.0 T and higher. Higher field strength magnets have the primary advantage of increased SNR, but this does generally come at the cost of increased power deposition in tissues, higher absolute (not relative) field inhomogeneity, higher radiofrequency (RF) field inhomogeneity, and higher equipment costs [55]. In the context of this thesis, the larger field strengths generally result in higher magnetic forces on magnetic materials, which is of particular concern for implanted medical devices [32], [53], [55].

Field inhomogeneity is of concern because image formation in MRI relies on the assumption that the main magnetic field is spatially uniform and temporally stable, and that the only source of additional field during signal acquisition is due to the gradient field system [37]. The details of this assumption, as well as all other details that concern image formation in MRI (e.g. spin relaxation, signal detection, k-space, pulse sequences, etc.) are outside the scope of this thesis and can be found in [56].

## 1.5 MRI systems

MRI systems are complicated multi-component entities. A MR scanner contains several magnetic field systems: the main magnet, radiofrequency (RF) coils, gradient coils, and shim coils [57]. This thesis discusses the interactions of medical devices composed of magnetic materials within the MR environment, focusing exclusively on interactions that relate to the static magnetic field of the main superconducting magnet. A brief overview of the main magnet is given in Section 1.5.1. In this thesis magnet design itself is not under consideration; therefore, the treatment of magnets is correspondingly brief.

### 1.5.1 Main Magnet

The main magnet of an MR scanner is responsible for providing the main magnetic field of a given scanner [57]. The operation of the main magnet is simple in principle. A flow of electric current will produce a magnetic field, and a loop of current will produce (along the axis of the loop) a net magnetic field perpendicular to that loop [44]. For a loop of current  $I$ , and radius  $R$ , centered upon the  $z$ -axis in Cartesian coordinates (see Figure 4) the magnetic flux density at the center of that loop is given by equation (24).

$$\mathbf{B} = \frac{\mu_0 I}{2R} \hat{\mathbf{z}} \quad (24)$$

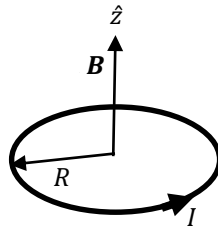


**Figure 4** – A loop of current  $I$ , and radius  $R$ , centered upon the  $z$ -axis in Cartesian coordinates will produce a magnetic flux density  $\mathbf{B} = \frac{\mu_0 I}{2R} \hat{\mathbf{z}}$  at the center of the loop, and  $\mathbf{B}(z) = \frac{\mu_0 I R^2}{2(R^2 + z^2)^{3/2}} \hat{\mathbf{z}}$  along the  $z$  axis.

The magnetic flux density as a function of  $z$ , through the center of the loop along the  $z$ -axis, is then given by equation (25).

$$\mathbf{B}(z) = \frac{\mu_0 I R^2}{2(R^2 + z^2)^{3/2}} \hat{\mathbf{z}} \quad (25)$$

Using this concept, a pair of current carrying loops of radius  $R$  can be placed a distance of  $R$  apart in order to produce a nearly homogeneous magnetic field in the center of the loops, see Figures 5 and 6.

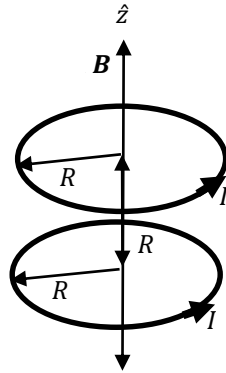


**Figure 5** – A pair of current carrying loops of current  $I$ , and radius  $R$ , placed a distance  $R$  apart will produce a nearly homogeneous magnetic field in the center of the loops. With the current loops centered upon the  $z$ -axis in Cartesian coordinates, they will produce a magnetic flux

density  $\mathbf{B} = \left(\frac{4}{5}\right)^{\frac{3}{2}} \frac{\mu_0 I}{R} \hat{\mathbf{z}}$  at the center of the loops and  $\mathbf{B}(\mathbf{z}) = \frac{\mu_0 I R^2}{2(R^2 + (z-l)^2)^{3/2}} \hat{\mathbf{z}} +$

$\frac{\mu_0 I R^2}{2(R^2 + (z+l)^2)^{3/2}} \hat{\mathbf{z}}$  along the  $z$ -axis, where  $l$  is the distance between the coil and the  $z = 0$ ,  $x$ - $y$  plane.

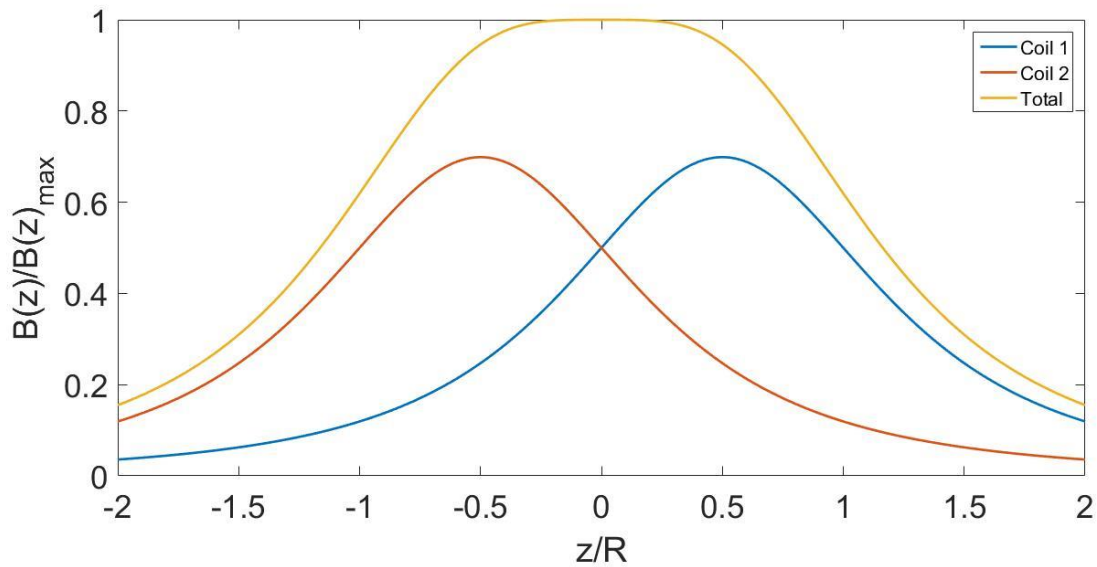


**Figure 6** –  $\mathbf{B}(z)$  as a function of  $z$  for a pair of current carrying loops. Two coils of current carrying wire placed a distance  $R$  apart, centered upon the  $z$ -axis in Cartesian coordinates, will produce the above magnetic flux density profile along the  $z$  axis. Contributions to the total  $\mathbf{B}(z)$  from each coil are shown. The total resulting  $\mathbf{B}(z)$  is nearly homogenous in the center of the coils. X-axis normalized to radius size and y-axis normalized to the maximum value of  $\mathbf{B}(z)$  to generalize to any coil pair.

In the case that multiple turns of non-spatially extending wire are used, the magnetic flux density at the center location between the loops along the  $z$ -axis is given by equation (26), where  $n$  is the number of turns of wire.

$$\mathbf{B} = \left(\frac{4}{5}\right)^{\frac{3}{2}} \frac{\mu_0 n I}{R} \hat{\mathbf{z}} \quad (26)$$

The magnetic flux density along the  $z$ -axis, down the center of the coil, is now given by

$$\mathbf{B}(z) = \frac{\mu_0 I R^2 n}{2(R^2 + (z - l)^2)^{3/2}} \hat{\mathbf{z}} + \frac{\mu_0 I R^2 n}{2(R^2 + (z + l)^2)^{3/2}} \hat{\mathbf{z}} \quad (27)$$

where  $l$  is the distance between the coil and the  $x$ - $y$  plane. For a coil pair centered around the  $z = 0$ ,  $xy$  plane,  $l = R/2$ . This is known as a Helmholtz pair, or Helmholtz coil.

The Helmholtz pair is designed to optimize the field homogeneity along the  $z$ -axis at the very center of the system ( $z=0$ ). In principal, an MR scanner main magnet is simply an extension of this concept, but with the region over which the field homogeneity is to be optimized defined over a larger region. Several coils of current carrying wire (typically 6) are placed along the bore at optimized locations and radii in order to produce a more homogenous magnetic field over a larger region [57]. Actively-shielded magnets will contain additional loops (typically 2) of oppositely wound coils in order to reduce or cancel the magnetic field outside of the system [57].

## 1.6 Computational Methods

This thesis seeks to develop and validate a comprehensive capacity to simulate the static magnetic field interactions, specifically magnetic force, experienced by medical devices in the MRI environment. Computational methods, such as *COMSOL* and other finite element method simulation packages are frequently described as a tool for investigating and determining medical device heating due to radiofrequency and gradient field interactions [34], [58]–[61]; references to such methods are sparse, if not unavailable, for magnetic force. This thesis seeks to develop a novel capacity to simulate the static magnetic field interactions, specifically magnetic force, and thus the finite element method and *COMSOL Multiphysics*, both used in this thesis to compute the aforementioned simulations, are introduced below.

The finite element method (FEM) is a method used to solve partial differential equations (PDE) that otherwise cannot be solved by analytical methods. FEM uses approximations of the PDEs which are based upon discretization. These approximations are made using numerical model equations, which then can be solved using numerical methods. The solution is thus an approximation of the real solution to the PDEs. The finite element method is used to compute such approximations [62].

*COMSOL Multiphysics (COMSOL, Sweden)* [63] is a software package, based on finite element methods, for modeling and simulating physics-based problems. Although the use of *MATLAB*

(*MathWorks, United states*) [64] and *Python (Python Software Foundation, Netherlands)* [65] is implemented within this thesis, all simulations are performed within *COMSOL Multiphysics*. The *AC/DC Module* is employed for simulating all the included electromagnetic interactions.

## 1.7 Research Objectives and Thesis Organization

The goal of this thesis is to address one current limitation to practical yet comprehensive testing of medical devices for use within the MRI system environment: the problem of worst-case device identification for magnetically induced force. As described earlier in this chapter, in most cases “devices” are in fact a family of multiple configurations, materials, and components, and there are far too many possible scenarios to physically test. Current regulatory standards require physical testing to be conducted in a conservative manner using a “worst-case” device or device configuration.

The primary objective of this thesis is to develop and validate a computer simulation capability for predicting the magnetic force experienced by any medical device in any MRI-relevant environment. This simulation capacity must have the ability to include an arbitrary MR magnet system, arbitrary device/material/configurations, and arbitrary positioning and orientation of the device within the MR magnet. If this objective is met, the simulation “pipeline” would enable a systematic procedure for identification of the worst-case device or device configuration for magnetic force from an otherwise impossibly large set of options. The simulation capacity is not intended to replace physical testing, but rather allow for physical testing to be focused on the most important devices within a device group or family.

The simulation capacity developed and described in this thesis is focused on the evaluation of magnetically induced force. Similar simulation capacity would need to be implemented for the other device interactions outlined earlier in this chapter. This capacity already exists for the evaluation and ranking of devices for RF heating. For torque and image-distortion, additional simulation work is necessary. However, much of the underlying simulation required for both torque and image-distortion would be common to the simulations described in this thesis, since both are fundamentally a static magnetic field interaction with a magnetic material. In particular,

preliminary work on the use of the simulations for predicting magnetic field inhomogeneity, which is the first step in predicting image distortion, was conducted. This work is tangential yet separate from the main objective described above. The results of these investigations are presented in Appendices E and F. They are included because, although incomplete, they provide additional means of validating the magnetic field simulations which underlie the magnetic force modeling as presented in Chapters 2 through 4.

The thesis is organized as follows. Chapter 2 presents all methods used, including simulation, derivation of analytic models for simulation validation, and experimental validation of the simulation. Appendix A is directly related to Chapter 2 as it overviews the specific experimental methods used as specified in ASTM F2052-15. Appendix B provides the details of the analytic derivation of the force model as required in Chapter 2. Chapter 3 summarizes all results obtained and Chapter 4 provides a discussion as well as summary of future work. Appendix C provides copies of the material certificates for the devices used in the experimental validation. Appendix D provides the raw data for the magnetic field mapping conducted on the 3.0 T MR scanner used in the experimental validation. As noted above, Appendices E and F describe two self-contained projects related to but tangential to the main content of this thesis.

## Chapter 2: Methodology

To utilize a computational method for the analysis of magnetic force on devices, such a model needs to be validated. As such, the following methods are described: development of a computational model of magnetic force; analytic validation of the computational model of magnetic force for a simple medical device in an idealized magnetic field; analytic and experimental validation of the computational model of magnetic force for a simple medical device in a 3T MR environment.

### 2.1 Computational Model of Magnetic Force

The computational model of magnetic force was developed using *COMSOL* and *MATLAB*. All design, modeling and simulations were performed in *COMSOL Multiphysics* using the ‘Magnetic Fields, No Current (mfnc)’ package and performed in a cubic simulation domain. Within the cubic simulation domain, a magnetic environment was implemented with the ‘Magnetic flux Density’ function of the ‘Magnetic Fields, No Current (mfnc)’ package. Once a magnetic environment is implemented in the simulation, devices can be added to the simulation as required. Device geometry, material composition, and spatial orientation can all be defined as required. All domains were meshed with free tetrahedrals.

Magnetic flux density, magnetization, mesh element volume, and spatial gradient of the  $\mathbf{B}$  field,  $\nabla \mathbf{B}$ , data -- all as a function of position -- is exported from the simulations. Magnetic force is given by equation (21).

$$\mathbf{F} = (\mathbf{m} \cdot \nabla) \mathbf{B} \quad (21)$$

As the magnetic moment is unknown, element volume scale factor and mesh element type are exported to determine the mesh element volume,  $dV$ , of each computational node.

$$\frac{\text{Element volume scale factor}}{\text{mesh element type}} = dV \quad (32)$$

The product of this volume and the magnetization,  $\mathbf{M}$ , is thus the magnetic moment,  $\mathbf{m}$ , of each node.

$$\mathbf{m} = \mathbf{M}dV \quad (33)$$

Within *MATLAB* a series of scripts import, define, and analyze the data to determine the total magnetic force. The developed computational model of magnetic force is therefore a “pipeline” where the force on a device can be directly calculated for a given magnetic environment.

## 2.2 Analytic Validation of a Computational Model of Magnetic Force

In order to validate the computational model, a test case was developed such that an analytic model could be produced to compare the simulation results. A background magnetic flux density in units Tesla,  $B_x = -0.5x T$ ,  $B_y = 0$ ,  $B_z = 0.5z T$ , was implemented at all boundaries of the computational model. This field was chosen due to its divergence of 0, which satisfies Maxwell’s equations, specifically, equation (3). Within this magnetic environment a cylinder of radius 1.27 cm, length  $L$ , and magnetic susceptibility  $\chi$ , was centered along the  $z$ -axis with the base of the cylinder at isocenter. Figure 7 depicts this geometry. This positioning allowed sufficient symmetry such that  $F_x=F_y=0$ , simplifying the analytic solution.

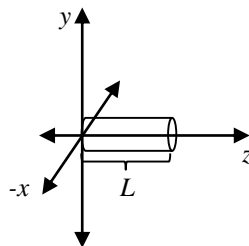


**Figure 7** – Geometry of a cylinder position within a *COMSOL* simulation. A cylinder of radius  $r=1.27$  cm and length  $L$  was centered along the  $z$ -axis. The base of the cylinder is positioned at isocenter. The integration over the volume of this cylinder is thus  $\pi r^2 \int_0^L dz$ .

Results of magnetic force were produced for two simulation sets. First, the length of the cylinder was kept constant at 2.54 cm and simulations were run varying the magnetic susceptibility of the

cylinder from 1 to  $10^6$  ppm. Next, the magnetic susceptibility was kept constant at 100 ppm and simulations were run varying the length of the cylinder from 1.27 to 25.4 cm.

In order to validate the results of the simulations, an analytic model of magnetic force was produced and this model was solved for all cases between simulation sets. The results of the analytic solution are compared to the simulation results in section Chapter 3, Figures 10-13.

The magnetic force on a material was given by equation (21), reproduced below.

$$\mathbf{F} = (\mathbf{m} \cdot \nabla) \mathbf{B} \quad (21)$$

In the case of an analytic model, a magnetic flux density can easily be defined, however the magnetic moment is unknown. The magnetic moment is given by re-arranging equation (10), such that the magnetic moment of an infinitesimal volume within a magnetic material,  $dV$ , is given by the product of that volume and the total magnetization,  $\mathbf{M}$ , of the material.

$$\mathbf{m} = \mathbf{M} dV \quad (33)$$

The total magnetization of the material is also unknown, however using equations (11), (12) and (15) from 1.3.2, magnetization can be described by the magnetic flux density.

$$\mathbf{M} = \chi \frac{\mathbf{B}}{\mu_0(1 + \chi)} \quad (34)$$

Combining equations (34), (33) and (21), magnetic force is given by equation (35), where  $\nabla \mathbf{B}$  is the spatial gradient of the magnetic flux density.

$$\mathbf{F} = \left( \chi \frac{\mathbf{B}}{\mu_0(1 + \chi)} dV \cdot \nabla \right) \mathbf{B} \quad (35)$$

For example, for a cylinder of radius  $r$  and length  $L$  centered along the  $z$ -axis, the base of the cylinder at isocenter in a magnetic flux density,  $B_x = -0.5x T$ ,  $B_y = 0$ ,  $B_z = 0.5z T$ , the magnetic force is given by equation (36).

$$F_z = \chi \frac{\pi r^2 \int_0^L 0.5z dz}{2\mu_0(1 + \chi)}, \quad F_x = F_y = 0 \quad (36)$$

This equation however, only accounts for first order magnetization. As discussed in 1.3.2, and as evident from equation (34), a material placed in a field  $\mathbf{B}$  acquires an induced magnetization  $\mathbf{M}$ . This magnetization will itself also produce a  $\mathbf{B}$  field. Removing the magnetic field strength,  $\mathbf{H}$ , from equation (1), it is possible to only observe the effective  $\mathbf{B}$  field due to the magnetization;  $\mathbf{B}_M$ .

$$\mathbf{B}_M = \mu_0 \mathbf{M} \quad (37)$$

This cycle of initial magnetic flux density,  $\mathbf{B}_0$ , causing magnetization,  $\mathbf{M}_1$ , which in turn causes an additional component of magnetic flux density,  $\mathbf{B}_{M_1}$ , continues ad infinitum;

$$\mathbf{M}_1 = \chi \frac{\mathbf{B}_0}{\mu_0(1 + \chi)} \quad (38)$$

$$\mathbf{B}_{M_1} = \mu_0 \mathbf{M}_1 \quad (39)$$

$$\mathbf{M}_2 = \chi \frac{\mathbf{B}_{M_1}}{\mu_0(1 + \chi)} \quad (40)$$

$$\mathbf{B}_{M_2} = \mu_0 \mathbf{M}_2 \quad (41)$$

and so on.

This results in a series,

$$\mathbf{F} = \left( \left( \sum_{i=1}^N \frac{\chi^i}{\mu_0(1+\chi)^i} \right) \mathbf{B}_0 \cdot \nabla \right) \left( \sum_{j=0}^N \frac{\chi^j}{\mu_0(1+\chi)^j} \right) \mathbf{B}_0 \quad (42)$$

which when  $\lim_{N \rightarrow \infty} \mathbf{F}$  is solved, gives the magnetic force, equation (43).

$$\mathbf{F} = \left( \frac{\chi(1+\chi)\mathbf{B}_0}{\mu_0} \cdot \nabla \right) \mathbf{B}_0 \quad (43)$$

Given a known initial magnetic flux density,  $\mathbf{B}_0$ , the magnetic susceptibility  $\chi$ , and the position and geometry of a material in Cartesian coordinates, the magnetic force can be calculated analytically by integrating over the volume of the material. For a cylinder of radius  $r$ , length  $L$ , positioned along the  $z$ -axis field, Figure 8, in a magnetic flux density,  $B_x = -0.5x T, B_y = 0, B_z = 0.5z T$ , the magnetic force is given by equation (44).

$$F_z = \frac{\chi(1+\chi)\pi r^2 \int_0^L z dz}{4\mu_0}, \quad F_x = F_y = 0 \quad (44)$$

In order to validate the computational model of magnetic force equation (44) was solved for a radius of 1.27 cm and for all values of  $\chi$ , and  $L$  used in simulation. Varying  $\chi$  from 1 to  $10^6$  ppm while  $L$  was kept constant at 2.54 cm and then  $\chi$  was kept constant at 100 ppm and  $L$  was varied from 1.27 to 25.4 cm.

## 2.3 Experimental Validation of a Computational Model of Magnetic Force

To further validate the computational model of magnetic force an experimental investigation of force was performed. In accordance to FDA and IEC guidelines, testing of force on medical devices is performed in agreement with ASTM F2052-15 “Standard Test Method for Measurement of Magnetically Induced Displacement Force on Medical Devices in the Magnetic Resonance Environment” [25][40]. The test for magnetic force, a deflection test, is performed

where a medical device is suspended within the region of the bore of the scanner and the angle the device deflects within the magnetic environment is measured. From this measured deflection angle, force is calculated. Full description of test methods, which were performed in accordance of ASTM F2052-15, are included in Appendix A.

Deflection tests were conducted for four steel rods of radius 0.00635 m, length,  $L$ , and mass,  $m$ , as listed in Table 1, at a 3T MRI system (Siemens Prisma). Data sheets for the steels are included in Appendix C. Exact magnetic susceptibility of the rods was not included in the data sheets and thus was unknown. Literature cites magnetic susceptibility values on the order of  $10^3$  ppm for 316 steel and for 304 steel [17], [38]. Rod lengths were machined to the values listed in Table 1. Magnetic properties of the steel are assumed to be unchanged as the steel is assumed to be non-ferromagnetic. [66]

Material	Length, $L$ [m] $\pm 0.01\text{mm}$	Mass, $m$ [kg] $\pm 0.1\text{g}$
316 Steel	0.0254	0.0255
	0.1000	0.1002
304 Steel	0.0254	0.0256
	0.1000	0.1001

**Table 1** – Specifications of the rods used in experimental tests of magnetic force as conducted with methods outlines in Appendix A. All rods have radius,  $r=0.635$  cm. Data sheets for the steels are included in Appendix C. Magnetic susceptibility of the steels was not included in the data sheets and thus was unknown. Rod lengths were machined to the values listed in the table.

The magnitude of the magnetic force on the device is given by,

$$F = mg \tan \alpha \quad (45)$$

where  $m$ , is the mass of the device,  $\alpha$  is the deflection angle and  $g$  is the acceleration due to gravity [40]. Using equation (45) and the results of the deflection test, magnetic force was calculated for all four rods. The results are shown in Chapter 3, Table 2.

To compare the computational model to the experimental results, the computational model had to be set up. To set up the computational model, the magnetic susceptibility of the materials needed to be known. The rods were shipped with calibration certificates, but they did not contain magnetic susceptibility values. In order to determine magnetic susceptibility, the measured deflection angle of each respective device was used. From ASTM F2052-15,  $\chi$  can be calculated using equation (46) [40].

$$\chi = \frac{\rho\mu_0 g \tan \alpha}{|\vec{B}_0| |\nabla|\vec{B}_0||} \quad (46)$$

Alternatively, by combining equations (43) and (45),

$$\chi(1 + \chi) = \frac{mg \tan \alpha}{\left(\frac{\mathbf{B}_0}{\mu_0} dV \cdot \nabla\right) \mathbf{B}_0} \quad (47)$$

and solving for  $\chi$ , equation (48) can be used.

$$\chi = \frac{1}{2} \left| \left( \pm \sqrt{\frac{mg \tan \alpha}{\left(\frac{\mathbf{B}_0}{\mu_0} dV \cdot \nabla\right) \mathbf{B}_0} + 1} - 1 \right) \right| \quad (48)$$

In order to solve for  $\chi$  from equation (48), and additionally to set up the simulation, the magnetic environment also needs to be known. As such,  $B_z$  field data was acquired from a 3T MRI system (Siemens Prisma) using a Hall-effect magnetic field probe at a sample spacing of 10 mm along the  $z$ -axis of the bore, Appendix D. Measurement was conducted along the  $z$ -axis of the bore using the laser landmark of the MR system to verify position within a +/-0.5 mm uncertainty. As described in ASTM F2052-15, along the scanner axis the magnetic field is known to only possess a  $z$ -component of magnetic flux density. This is the reason that the force tests are conducted along this axis of the scanner.

To model the magnetic environment a linear approximation,  $B_{z,linear}(z)$ , of the field over the region in which the devices were placed was formed.

$$B_{z,linear}(z) = (\nabla B_{z,experimental})z + B_{z,experimental}(0) \quad (49)$$

The magnetic flux density as a function of  $z$  position was imported into *MATLAB*. The spatial gradient at every data point acquired was calculated and the slope of the line, equation (49), was taken as the average of the spatial gradients over the region in which the device was placed. The  $y$ -intercept of the linear approximation was determined by taking the average of three solutions of the  $y$ -intercept; using the equation of a line and the measured  $B_z$  value at the two edges of the device, and the center of the device. This provided the linear approximation shown in equation (50).

$$B_{z,linear}(z) = (4.2 \text{ T/m})z + 5.6 \text{ T} \quad (50)$$

For the computational model, this linear approximation was used to model the magnetic environment. The linear approximation was used, rather than importing the measured field data directly, since the field data only contained information of  $B_z$ . This would violate equation (3) since the divergence is not zero, equation (51).

$$\nabla \cdot B_z \neq 0 \quad (51)$$

As such, a negative  $x$  component of magnetic flux density with the same profile as  $B_{z,linear}$  was also added to the magnetic environment. The total magnetic environment was  $B_x = -B_{z,linear}(x)$ ,  $B_y = 0$ ,  $B_z = B_{z,linear}(z)$ , more specifically  $B_x = -(4.2 \text{ T/m})x + 5.6 \text{ T}$ ,  $B_y = 0$ ,  $B_z = (4.2 \text{ T/m})x + 5.6 \text{ T}$ , which satisfies equation (3). The symmetry of the simulation cancels out the  $x$  component of the field within the device such that  $B_x$  does not affect the simulation other than providing sufficient magnetic environment to satisfy the divergence requirement of Maxwell's equations.

Again using the linear approximation, magnetic susceptibility of each rod was determined. From equation (48), the linear approximation of the field can be used to integrate the magnetic flux

density over each specific device, and plugging in the measured deflection angle, mass of each specific device,  $\chi$  can be determined for each rod.

Within the simulation, a cylinder of radius 0.00635 m, length  $L$ , and magnetic susceptibility  $\chi$  was added at a location of -0.8 m from the isocenter. This simulation was computed for all four rods from Table 1. The results of the simulation as well as a comparison to the experimental results can be found in Chapter 3; Figure 17 and Table 3.

Additionally, as the device was again a cylinder, using the same derivation as equation (44), an analytic solution could be derived for this experimental case; (52). The geometry of equation (52) is visualized in Figure 8.

$$F_z = \frac{\chi(1 + \chi)\pi r^2 \int_{-0.8 - (\frac{L}{2})}^{-0.8 + (\frac{L}{2})} (4.2 \text{ T/m})z + 5.6 \text{ T} dz(4.2 \text{ T/m})}{\mu_0}, F_x = F_y = 0 \quad (52)$$

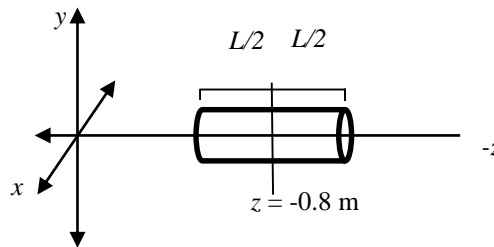


**Figure 8** – Geometry of a rod position within a *COMSOL* simulation. A rod of radius  $r = 0.635$  cm and length  $L$  was centered along the  $z$  axis with the midpoint of the rod at a position of  $z = -0.8$  m. The integration over the volume of this cylinder is thus  $\pi r^2 \int_{-0.8 - (\frac{L}{2})}^{-0.8 + (\frac{L}{2})} dz$ .

## Chapter 3: Results

In order to validate a computational model of magnetic force, an analytic model was derived. With a simple device and idealized magnetic environment, both models were computed for identical cases. The results from varying the magnetic susceptibility of a cylinder with a constant length are shown in Figure 9. Results from varying the length of the cylinder at a constant magnetic susceptibility are shown in Figure 11. Using the analytic model as truth, the percent error between the simulated result and the analytic solution was calculated. Percent error when varying the magnetic susceptibility of a cylinder with a constant length is shown in Figure 10. Percent error when the length of the cylinder is varied at a constant magnetic susceptibility is shown in Figure 12.

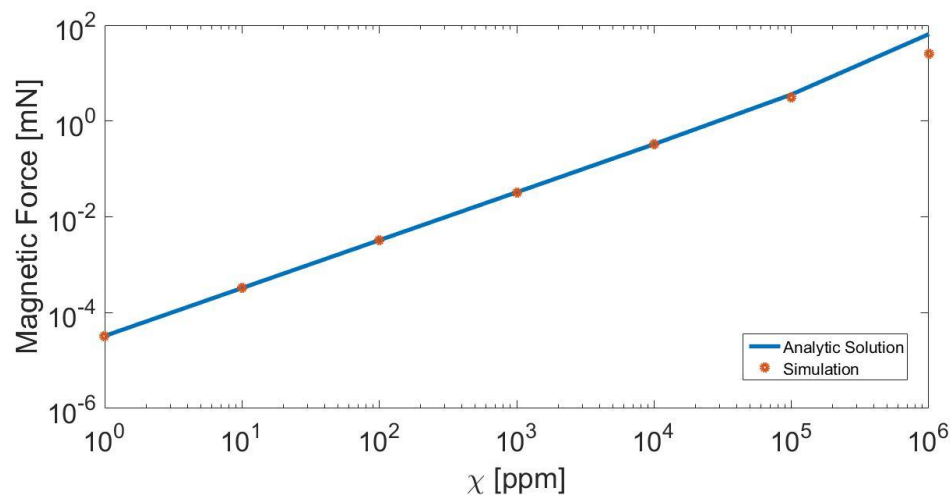


**Figure 9** - Magnetic force as a function of magnetic susceptibility,  $\chi$ , for a cylinder of radius 1.27 cm, and length 2.54 cm in a magnetic environment  $B_x = -0.5x T, B_y = 0, B_z = 0.5z T$ . Cylinder is positioned about the  $z$ -axis. Simulated results and analytic solution are shown. Analytic solution is given by  $F_z = \frac{\chi(1+\chi)\pi r^2 \int_0^L z dz}{4\mu_0}$ ,  $F_x = F_y = 0$  where  $L$  is 2.54 cm.

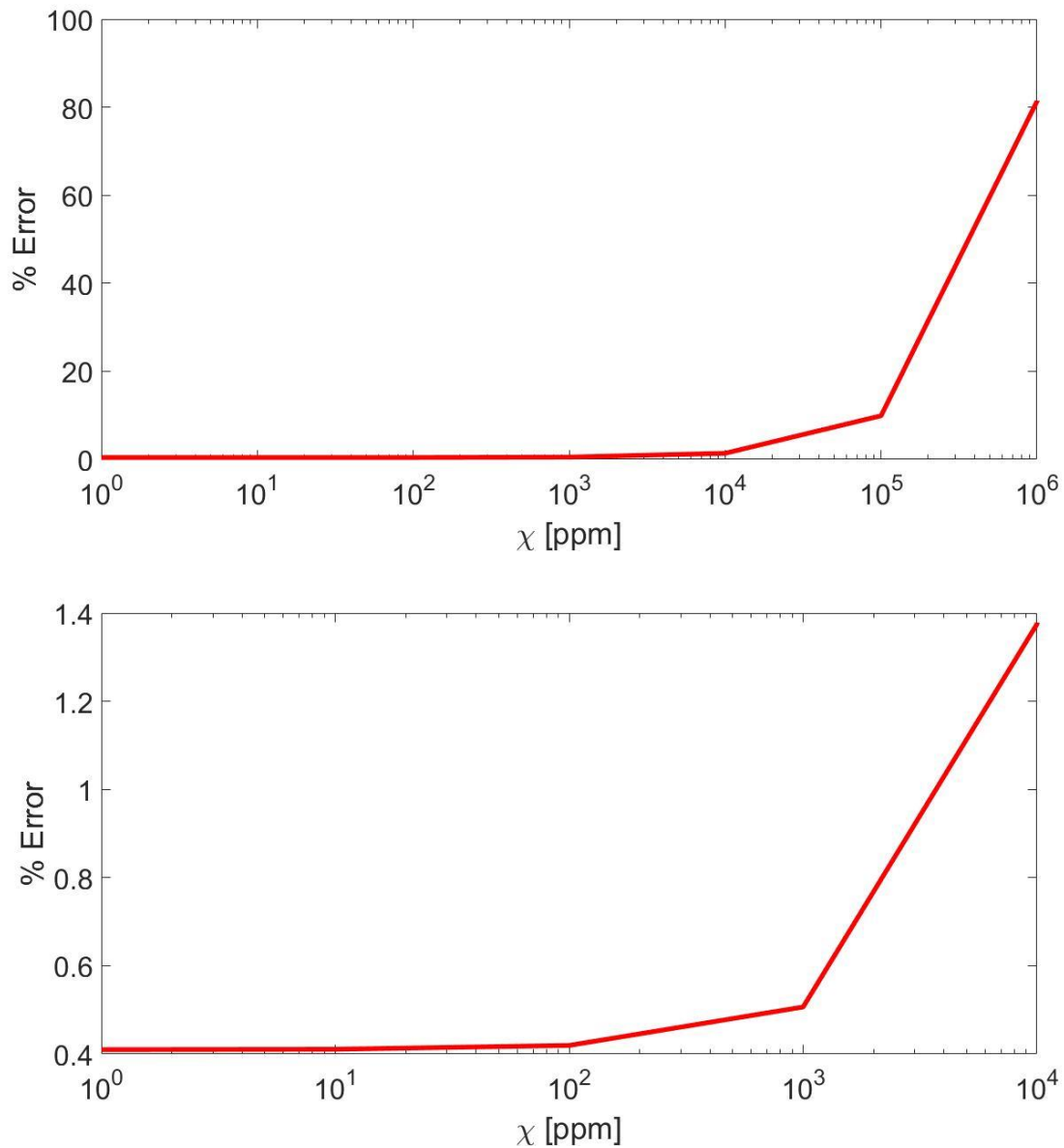


**Figure 10** – (Top) Percent error when simulated results are compared to an analytic solution for the magnetic force of a cylinder of radius 1.27 cm, and length 2.54 cm in a magnetic environment  $B_x = -0.5x T, B_y = 0, B_z = 0.5z T$  as a function of magnetic susceptibility,  $\chi$ .

Cylinder is positioned about the  $z$ -axis. Analytic solution is given by  $F_z = \frac{\chi(1+\chi)\pi r^2 \int_0^L z dz}{4\mu_0}$ ,

$F_x = F_y = 0$  where  $L$  is 2.54 cm. (Bottom) Axis limit of above plot is restricted to  $\chi < 10^4$  ppm as implant-grade metals have values of susceptibility  $< 10^4$  ppm.

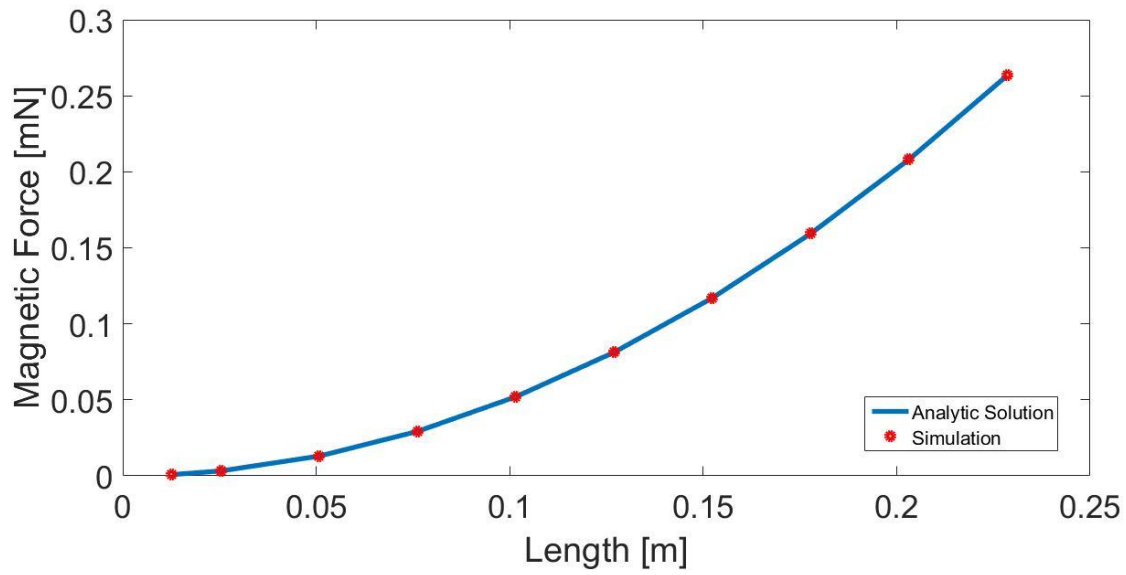


**Figure 11** - Magnetic force as a function of cylinder length,  $L$  for a cylinder of radius 1.27 cm, and magnetic susceptibility 100 ppm in a magnetic environment  $B_x = -0.5x T, B_y = 0, B_z = 0.5z T$ . Cylinder is positioned about the  $z$ -axis. Simulated results and analytic solution are shown. Analytic solution is given by  $F_z = \frac{\chi(1+\chi)\pi r^2 \int_0^L z dz}{4\mu_0}$ ,  $F_x = F_y = 0$  where  $\chi$  is 100 ppm.

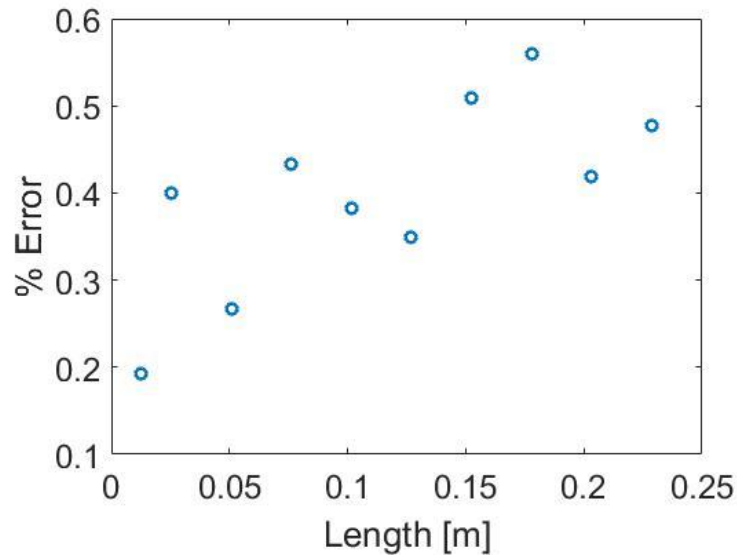


**Figure 12** - Percent error when simulated results are compared to an analytic solution for the magnetic force of a cylinder of radius 1.27 cm and magnetic susceptibility 100 ppm in a magnetic environment  $B_x = -0.5x T$ ,  $B_y = 0$ ,  $B_z = 0.5z T$  as a function of cylinder length,

$L$ . Cylinder is positioned about the  $z$ -axis. Analytic solution is given by  $F_z = \frac{\chi(1+\chi)\pi r^2 \int_0^L z dz}{4\mu_0}$ ,  $F_x = F_y = 0$  where  $\chi$  is 100 ppm.

In order to experimentally validate a computational model of magnetic force, a magnetic force deflection test was performed for several rods. Table 2 shows the results of these tests and gives the average deflection angle measured over three trials of each test. The magnetic force as calculated by equation (45) is also provided.

Material	Length, L [m] $\pm 0.01\text{mm}$	Mass, m [kg] $\pm 0.1\text{g}$	Average Deflection, $\alpha$ [deg] $\pm 0.3^\circ$	Force [N] $F = mgtan\alpha$
316 Steel	0.0254	0.0255	15.3	$0.069 \pm 0.007$
	0.1000	0.1002	14.3	$0.25 \pm 0.03$
304 Steel	0.0254	0.0256	23.0	$0.11 \pm 0.01$
	0.1000	0.1001	21.1	$0.38 \pm 0.04$

**Table 2** – Experimental results of deflection test conducted for each of the four rods specified in the table, as conducted to methods outlines in Appendix A. All rods have radius,  $r=0.635$  cm. Data sheets for the steels are included in Appendix C. Rod lengths were machined to the values listed in the table. Deflection test conducted at a 3T (Siemens Prisma) MRI system. Deflection angle was average over three trials of measurement. Magnetic susceptibility of the steels was not included in the data sheets and thus was unknown.

In order to determine the magnetic susceptibility of each device, and to define a magnetic environment within the computational model the  $z$  component of the magnetic flux density of the 3T (Siemens Prisma) system was measured. Figure 13 plots this data. From this data a linear approximation to the measured field was derived. This linear approximation is shown in Figure 14 and the difference between the linear approximation and the measured field data is presented in Figure 15.

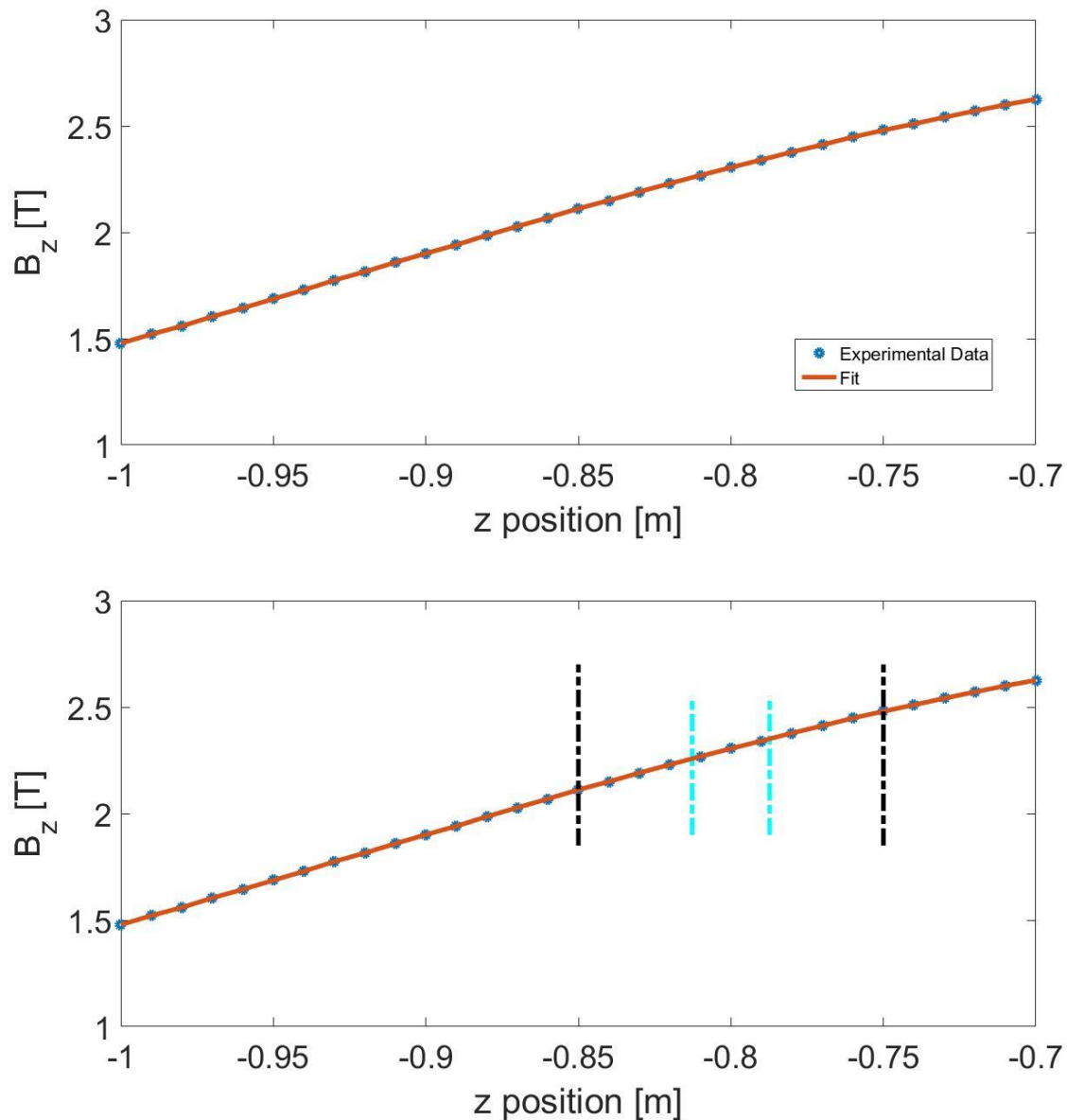


**Figure 13** – (Top)  $B_z$  field as a function of  $z$  down the center on axis line of a 3T MRI (Siemens Prisma) as measured by a Hall-effect magnetic field probe.  $Z$  position is measured as the distance from the isocenter where the isocenter is defined as  $z = 0$ . Data points were measured with sample spacing of 10 mm. Measured data table included in Appendix D. (Bottom) The region along  $z$  over which 10-cm rods are placed shown with vertical black lines. The region along  $z$  over which 2.54-cm rods are placed shown with vertical cyan lines. Error bars are too small to be seen.

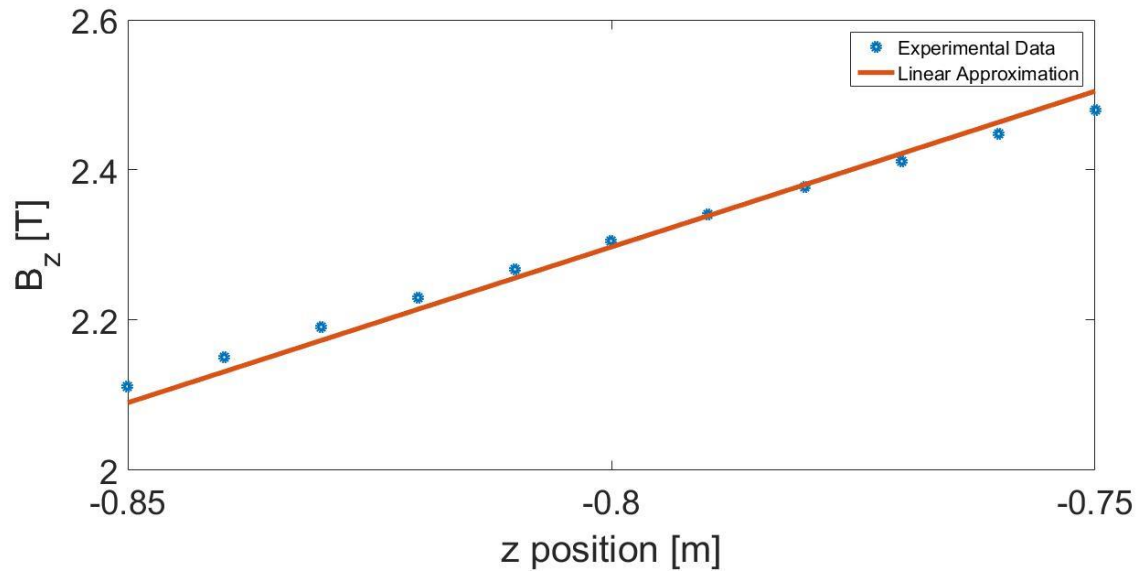


**Figure 14** – Linear approximation, as calculated in 2.2.3,  $B_{z,linear}(z) = (4.2 \text{ T/m})z + 5.6 \text{ T}$ , of the experimentally measured  $B_z$  field data.  $B_z$  field as a function of  $z$  down the center on axis line of a 3T MRI (Siemens Prisma) as measured by a Hall-effect magnetic field probe. Axis limited to highlight approximate region over which the rods are placed.  $Z$  position is measured as the distance from the isocenter where the isocenter is defined as  $z = 0$ . Data points were measured with sample spacing of 10 mm. Measured data table included in Appendix D. Error bars are too small to be seen.

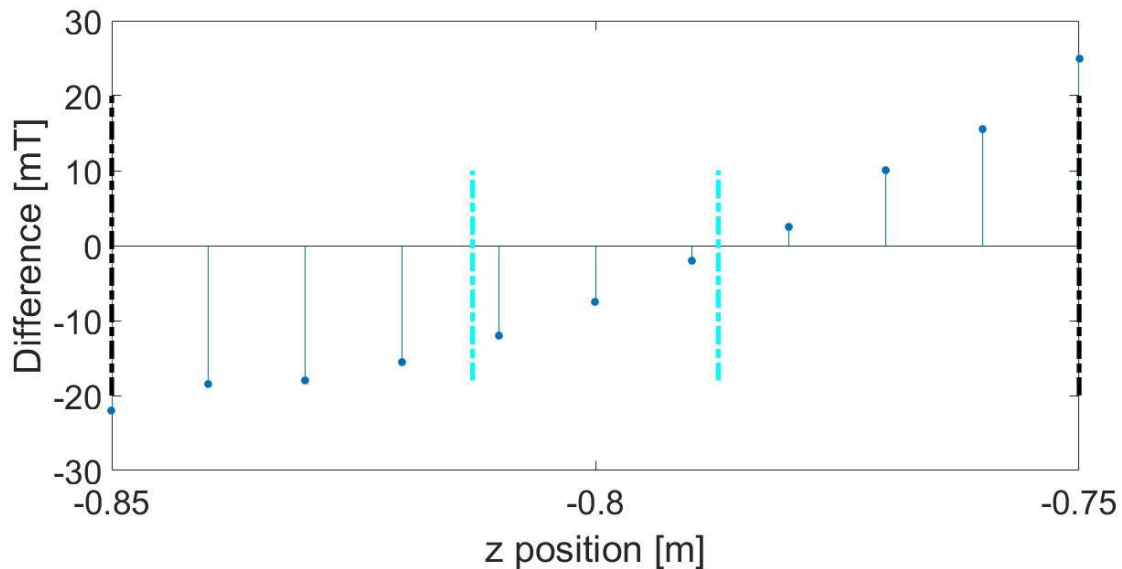


**Figure 15** – Difference when comparing the linear approximation,  $B_{z,linear}(z) = (4.2 \text{ T/m})z + 5.6 \text{ T}$ , to the experimentally measured  $B_z$  field data over the approximate region over which the rods are placed. The region along  $z$  over which 10 cm rods are placed shown with vertical black lines. The region along  $z$  over which 2.54 cm rods are placed shown with vertical cyan lines.  $B_z$  field as a function of  $z$  down the center on axis line of a 3T MRI (Siemens Prisma) as measured by a Hall-effect magnetic field probe.  $Z$  position is measured as the distance from the isocenter where the isocenter is defined as  $z = 0$ . Data points were measured with sample spacing of 10 mm. Measured data table included in Appendix D. Error bars are too small to be seen.

Using the linear approximation, deflection and equation (48), magnetic susceptibility for each device was determined. These values of  $\chi$  are listed in Table 3. Using these specific values for each length and material, the computational model was used to determine a simulated value of magnetic force, which also present in Table 3.

Both experimental, and computational values of magnetic force are presented in Figure 16. Comparing the simulation results of magnetic force to the experimentally calculated values of magnetic force, the percent difference between these data sets is shown in Figure 17, and Table 3.

Material	Length, L [m] $\pm 0.01\text{mm}$	$\chi$ [ppm] $\times 10^3$	Simulated Force [N]	Force [N] $F = mgtan\alpha$	% Difference
316 Steel	0.0254	$2.8 \pm 0.3$	0.06842	$0.069 \pm 0.007$	0.20
	0.1000	$2.6 \pm 0.3$	0.2508	$0.25 \pm 0.03$	0.064
304 Steel	0.0254	$4.4 \pm 0.5$	0.1062	$0.11 \pm 0.01$	0.35
	0.1000	$4.0 \pm 0.5$	0.3790	$0.38 \pm 0.04$	0.31

**Table 3** – Experimentally calculated magnetic susceptibility, simulated value of magnetic force and percent difference between simulated value of magnetic force and experimental value of force for each of the four rods specified in the table. Magnetic susceptibility was calculated using the results of the deflection test listed in Table 2, the linear approximation to the magnetic flux density of the 3T calculated in 2.2.3 and equation (48). This value of  $\chi$  was used in the computational model of force to produce the simulated magnetic force values presented in the table. The percent difference is the result of comparing these simulated values of force to the experimentally determined values of force in Table 2.

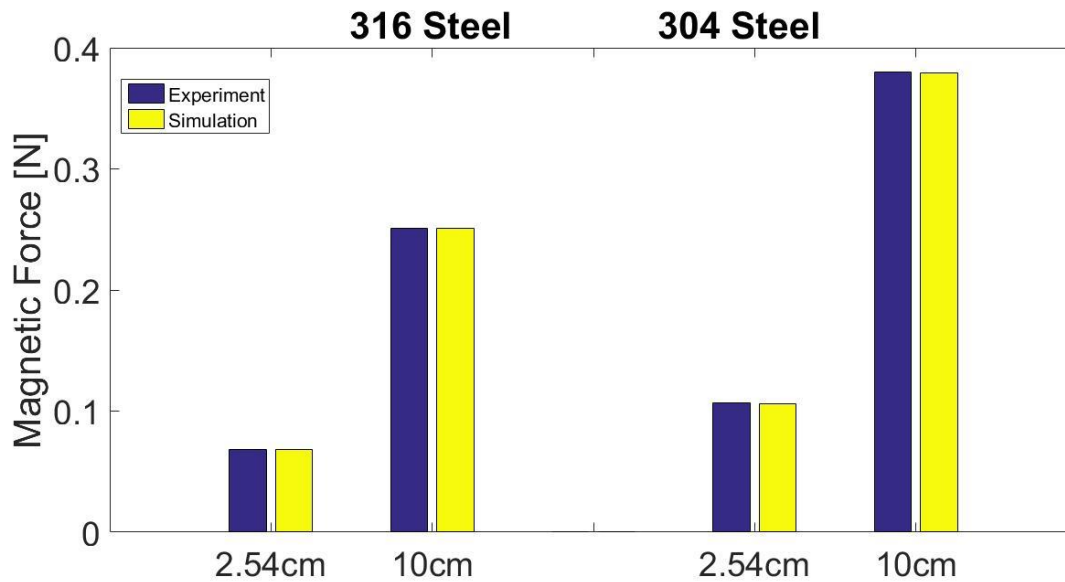


**Figure 16** – Magnetic force as calculated by an experimental deflection test as conducted to methods outlines in Appendix A, and simulation for two steels, 316 and 304, at two lengths per steel, 2.54 cm and 10 cm. Specifications of the rods are found in Table 1 and magnetic susceptibilities are found in Table 3. Deflection test conducted at a 3T (Siemens Prisma) MRI system. Simulation performed within computational model developed in 2.2.1. Error bars are omitted as the experimental value of magnetic force is used to calculate the magnetic susceptibility value used in the simulation. Any error present in the experiment is automatically present in the simulation. Error bars would thus be redundant when looking to compare the data sets.

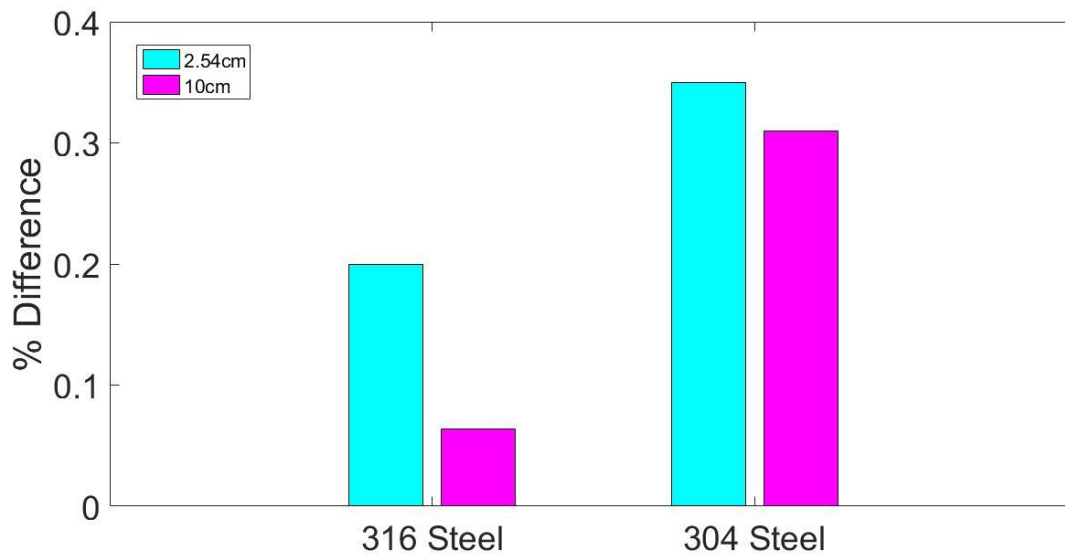


**Figure 17** – Percent difference when comparing simulated value of magnetic force and experimental value of force two steels, 316 and 304, at two lengths per steel, 2.54 cm and 10 cm. Experimental value of magnetic force as calculated by an experimental deflection test as conducted to methods outlines in Appendix A. Specifications of the rods are found in Table 1 and magnetic susceptibilities are found in Table 3. Deflection test conducted at a 3T (Siemens Prisma) MRI system. Simulation performed within computational model developed in 2.2.1.

## Chapter 4: Discussion and Conclusion

This chapter reflects on the main results from Chapters 3. Future work involving additional validation of the computational model of magnetic force with extensions to measurements of torque are suggested. Two projects involving the extension of the methods described in this thesis are presented as appendixes. Conclusions are drawn on the basis of the findings in this thesis. In particular, the computational method of evaluating magnetic force is advocated for medical devices of materials of magnetic susceptibility less than  $10^4$  ppm.

### 4.1 Analytic Validation

The initial validation, an analytic validation, involved the calculation of the magnetic force on a simple medical device in an idealized magnetic field. Using both analytic and computational methods, a cylinder of radius 1.27 cm, length  $L$  and magnetic susceptibility  $\chi$  was centered along the  $z$ -axis with the center of cylinder at isocenter in a magnetic environment  $B_x = -0.5x T, B_y = 0, B_z = 0.5z T$ . Figure 9 shows a linear increase in both simulated and analytic values of magnetic force for values of magnetic susceptibility below  $10^5$  ppm. For larger susceptibilities, the simulation begins to underestimate force compared to the analytic solution. Using the analytic model as truth, the percent error between the simulated result and the analytic solution was calculated. Figure 10 shows the percent difference between the two data sets. Error is less than 1% for  $\chi < 10^4$  ppm, and less than 10% for  $\chi < 10^5$  ppm. Above  $\chi = 10^5$  ppm, percent error has a very large increase. The increase in percent error is likely due to materials entering the regime of ferromagnetism. As magnetic susceptibility increases beyond  $10^4$  ppm they become ferromagnetic. As such it is likely the simulation does not account for the increasing effect of ferromagnetic magnetization. That is, the simulation under represents the non-linearity of the magnetic material. Additionally, it is likely that the simulation is underestimating the effect the magnetization has on the surrounding field as  $\chi$  increases. As previously described, magnetization and magnetic flux density have a cyclic nature. The simulation likely begins to underestimate this nature at  $\chi > 10^4 - 10^5$  ppm. Implant-grade metals (i.e. stainless steel 316, cobalt-chromium alloys, titanium alloys) however, all have  $\chi$  less than or on the order of  $10^4$  ppm, where error would be less than 1%.

Again, using both analytic and computational methods, a cylinder of radius 1.27 cm varied length,  $L$ , and magnetic susceptibility 100 ppm, centered along the  $z$  axis with the center of cylinder at isocenter in a magnetic environment  $B_x = -0.5x T, B_y = 0, B_z = 0.5z T$ . Figure 11 shows both the analytic and simulated force due to a cylinder of varying length. Magnetic force in both simulated and analytic values of magnetic force increases as length increases. This is due to two factors. The rod is extending into regions of larger spatial gradient and thus is experiencing a larger force, and the device is increasing in mass. The larger the device the more magnetization it can develop and the larger the force it will experience. Simulation and analytic solutions appear to agree. The percent error between the two data sets, shown in Figure 12, increases slightly with length but is less than 0.6% for all lengths. Percent error is dominated by magnetic susceptibility rather than device size.

The results give confidence that the computational model of magnetic force is sufficient to predict magnetic forces on materials with magnetic susceptibility less than  $10^5$  ppm, and is ideal for use on materials with magnetic susceptibility less than  $10^4$  ppm such as implant-grade metals.

## 4.2 Experimental Validation

To further validate the computational model of magnetic force, an experimental investigation of force was performed. A force deflection test was conducted for two alloys of steel, both at a radius of 0.635cm, and length of 2.54 cm and 10 cm. Table 2 shows the average angle of deflection measured over three trials of deflection and the associated force calculated for that rod based on the average angle of deflection. As previously seen in the analytic validation, force increases as length of material increases as expected. Additionally, force is always higher for the 304 steel rod than the associated 316 steel rod. This is also to be expected since 304 steel has a higher magnetic susceptibility, and as seen with the analytic validation, higher susceptibilities lead to greater forces.

To produce simulations of force the magnetic susceptibilities of the materials had to be deduced. Additionally, to define a magnetic environment within the computational model the magnetic environment of the 3T system had to be known. This required measuring the 3T (Siemens Prisma) system. The  $z$  component of the magnetic flux density was measured with a Hall-effect

field probe precise to 0.1 mT within 0.5 mm positioning certainty. Considering the field is spatially dependent, the positioning uncertainty would also produce uncertainty in the magnetic flux density. Using the approximate field gradient within the region of device testing, equation (50), this would lead to a total possible error in field measurement of approximately 25 mT due to positional uncertainty, roughly 1%. From this data, Figure 13, the magnetic flux density looks to be linear over the region in which the devices are placed. As such a linear approximation of the measured field data was derived, Figure 14. The difference between the linear approximation and the measured field data is presented in Figure 15 where the regions of  $z$  where the 2.54 cm and 10 cm lengths of rods would lie are denoted by corresponding vertical black and cyan lines. Within these regions the difference in linear approximation is approximately 10 mT, roughly 0.5% error, at the mid-point position of  $z = -0.8$  m; and 25 mT, roughly 1% error, at the point of largest difference. Combining this with the measurement uncertainty of the field itself, it is estimated that the linear approximation has at most 2 % error for any given point. This difference was considered acceptable and the linear approximation was applied.

Using the linear approximation, deflection angle, and equation (48), the associated magnetic susceptibility was solved for each rod, shown in Table 3. The magnetic susceptibility of 316 steel is approximately 2700 ppm and magnetic susceptibility is approximately 4200 ppm for 304 steel, both within the region of susceptibilities for stainless steels [17], [38]. Of note is that the two calculated susceptibilities for the 316 steel have a 7.2% difference between each other and for the 304 steel the susceptibilities have a 9.8% difference. It is expected that for each respective steel the two lengths have identical magnetic susceptibility as the different lengths of rods were machined from the same sample. This discrepancy in magnetic susceptibility between lengths of rods is due to experimental errors and uncertainties in the deflection test, and measurement uncertainties of the magnetic field measurements and resulting linear approximation to the field. When propagating the experimental uncertainties, the experimental measurement of force has an uncertainty within approximately 10-12% of the value of force. As previously discussed, the error of the linear approximation to the field could be as high as 2%. Since the magnetic susceptibility is calculated using the experimentally measured value of magnetic force and the linear approximation, using equation (48), these uncertainties carry into the value of  $\chi$ . When considering this, and propagating these uncertainties, the values of  $\chi$  for each material, 304 and 316 stainless steel, agree within experimental uncertainty.

The goal however, is to compare the computational method of calculating magnetic force and the experimental method of calculating magnetic force. Since the computational method implements the linear approximation, the calculated values of  $\chi$  can be taken as truth. Using the calculated values of  $\chi$ , any error within the value of  $\chi$  from the experimental measurement of force is then an input into the simulation. Thus when comparing the simulation to the experimental value of force, all sources of error in the value of  $\chi$  from experiment are cancelled. Additionally, since the computational model implements the magnetic environment using the linear approximation, any error in  $\chi$  from the use of this approximation are also already accounted for.

Using the specific calculated values of  $\chi$  for each length and material, the computational model of magnetic force was used to determine a simulated value of magnetic force, which is presented in Table 3. The magnetic force produced by simulation was less than the measured force in all cases, as illustrated in Figure 16 where both experimental and computational values of magnetic force are presented. Error bars are omitted as the experimental value of magnetic force is used to calculate the magnetic susceptibility value in the simulation. Any error present in the experiment is automatically present in the simulation. Error bars would thus be redundant when comparing the data sets. This result agrees with the findings of the analytic validation, which predicted that for susceptibilities over 1000 ppm the simulation would start to under estimate force. This under prediction is very small however, as the percent difference between these data sets is less than 1%, shown in Figure 17, where the simulation results of magnetic force and the experimentally calculated values of magnetic force are compared, and Table 3. Again, this matches the results of the analytic validation as it predicted error less than 1% for  $\chi < 10^4$  ppm. Figure 17 also shows a trend of increased percent difference in 304 steel over 316 steel which agrees with the trend of increased percent difference of the simulation as magnetic susceptibility increases. Additionally, percent difference seems to decrease for the longer device. This could be due to increased computational nodes, which gives a more accurate representation of magnetization.

### 4.3 Conclusion

The objective of this thesis was to develop and validate a computational capacity to predict the magnetic force experienced by any medical device in any MRI-relevant environment. Using analytic techniques, it was shown that for materials with magnetic susceptibility  $<10^5$  ppm, a computational model of magnetic force was correct within 10% error, which decreased to less than 1% for  $\chi < 10^4$  ppm. The size of the device had little effect on error. Experimentally, two steels of magnetic susceptibility  $<10^4$  ppm had error less than 1%. The computational model of magnetic force is ideal for use on materials with magnetic susceptibility less than  $10^4$  ppm such as implant-grade metals.

Current regulatory standards require physical testing to be conducted in a conservative manner using a “worst-case” device or device configuration. One of the most difficult elements of carrying out this procedure is the determination of what represents a “worst-case” device or device configuration. Simulation offers the potential for a systematic procedure for identification of the worst-case device or device configuration for magnetic force from an otherwise impossibly large set of options. The work presented in this thesis gives support to the claim that force can be predicted within 1% of the current experimental methods of measuring magnetic force, for devices within magnetic susceptibility less than  $10^4$  ppm. However, patient safety is at the utmost concern, and testing method needs to be rigorously validated in order to not compromise patient safety. This thesis does give confidence in the use of simulation in the context of static magnetic field interactions of medical devices in the MRI environment and with further research, the computational model developed could be implemented to predict the magnetic force of medical devices in order to determine what represents a “worst-case” device or device configuration.

## 4.4 Future Work

As an extension to the work presented in this thesis several future works are suggested. Future work involving additional validation of the computational model of magnetic force with more complex devices, extensions of the model to include measurements of torque, and testing of magnetic materials with known magnetic susceptibilities is suggested. Additionally, two projects extending the methods of this thesis to evaluate field inhomogeneities are presented.

Further validation of the computational model of magnetic force with more complex devices would greatly improve confidence in the model. As larger, more complex geometries can generally be thought of the combination of multiple simple parts, the work in this thesis should extend very well to larger more complex devices. However, very small features and edges of more complex device geometries have the potential to produce larger differences between the computational model and experimental results as the computational could fail to accurately represent these geometries.

To better understand the error within experimental and simulated measures of magnetic force, deflection tests with materials of known susceptibilities should be conducted. The experimental values of force were used as the gold standard to compare the computational model for validation. However, there is a relatively large uncertainty in the experimentally measured values of magnetic force which leads to an uncertainty in the value of magnetic susceptibility used in the computational model. The validity of the computational model could be better determined if simulations with materials of known magnetic susceptibility were to be conducted and experimentally validated.

The computational model could also be extended to include interactions of torque. The added capacity to simulate torque would greatly improve the practicality of this model in a device testing application. This added capacity would also need to be experimentally validated.

The methods described in this thesis can also be extended to evaluate field inhomogeneities. For evaluation of magnetic force, magnetic environments can be implemented and magnetic materials can be simulated in these environments. In order to calculate magnetic force, detailed information of the effect of these materials on the magnetic field is exported. Using similar

computational methods developed in this thesis, with different analysis scripts, the work in thesis can be expanded to evaluate field inhomogeneities. Appendixes E and F describe two projects that were undertaken together with an industry partner, *Synaptive Medical (Toronto, Canada)*. In Appendixes E main field homogeneity of a MR main magnet is investigated in the presence of foreign materials. In Appendixes F systematic errors of nuclear magnetic resonance field probes are investigated as a guide to their construction.

## References

- [1] Canadian Institute for Health Information (CIHI), “Medical Imaging in Canada,” 2012.
- [2] J. F. Schenck, “Safety of Strong, Static Magnetic Fields,” *J. Magn. Reson. Imaging*, vol. 12, no. 1, pp. 2–19, Jul. 2000.
- [3] R. K. and M. S. Staton, “Current clinical issues for mri scanning of pacemaker and defibrillator patients.,” *J. Am. Med. Assoc.*, 2011.
- [4] C. S. Simpson and A. M. Gillis, “The pacemaker and implantable cardioverter defibrillator recall issue - a Canadian perspective.,” *Can. J. Cardiol.*, vol. 22, no. 6, pp. 467–71, 2006.
- [5] F. G. Shellock and A. Spinazzi, “MRI Safety Update 2008: Part 2, Screening Patients for MRI,” *Am. J. Roentgenol.*, vol. 191, no. 4, pp. 1140–1149, Oct. 2008.
- [6] A. M. Sawyer-Glover and F. G. Shellock, “Pre-MRI procedure screening: Recommendations and safety considerations for biomedical implants and devices,” *Journal of Magnetic Resonance Imaging*, vol. 12, no. 1. pp. 92–106, 2000.
- [7] F. G. Shellock, “MR imaging of metallic implants and materials: A compilation of the literature,” *American Journal of Roentgenology*, vol. 151, no. 4. pp. 811–814, 1988.
- [8] F. G. Shellock, T. O. Woods, and J. V. Crues, “MR Labeling Information for Implants and Devices: Explanation of Terminology,” *Radiology*, vol. 253, no. 1, pp. 26–30, Oct. 2009.
- [9] T. Birkholz, M. Schmid, C. Nimsky, J. Schüttler, and B. Schmitz, “ECG artifacts during intraoperative high-field MRI scanning.,” *J. Neurosurg. Anesthesiol.*, vol. 16, no. 4, pp. 271–6, Oct. 2004.
- [10] J. A. Nyenhuis, S. M. Park, R. Kamondetdacha, A. Amjad, F. G. Shellock, and A. R. Rezai, “MRI and implanted medical devices: Basic interactions with an emphasis on heating,” *IEEE Trans. Device Mater. Reliab.*, vol. 5, no. 3, pp. 467–479, 2005.
- [11] P. F. New *et al.*, “Potential hazards and artifacts of ferromagnetic and nonferromagnetic surgical and dental materials and devices in nuclear magnetic resonance imaging.,”

- Radiology*, vol. 147, no. 1, pp. 139–148, 1983.
- [12] J. Starčuková, Z. Starčuk, H. Hubálková, and I. Linetskiy, “Magnetic susceptibility and electrical conductivity of metallic dental materials and their impact on MR imaging artifacts,” *Dent. Mater.*, vol. 24, no. 6, pp. 715–723, Jun. 2008.
- [13] ASTM F2503 – 13, “Standard Practice for Marking Medical Devices and Other Items for Safety in the Magnetic Resonance Environment,” *ASTM Int.*, pp. 1–7, 2008.
- [14] ASTM F2182 – 11a, “Standard test method for measurement of radio frequency induced heating near passive implants during magnetic resonance imaging,” *ASTM Int.*, no. December, pp. 1–14, 2002.
- [15] F. G. Shellock and J. V. Crues, “MR Procedures: Biologic Effects, Safety, and Patient Care,” *Radiology*, vol. 232, no. 3, pp. 635–652, Sep. 2004.
- [16] ISO 13485, “Medical devices — Quality management systems — Requirements for regulatory purposes,” 2016.
- [17] K. El Bannan, W. B. Handler, C. Wyenberg, B. A. Chronik, and S. P. Salisbury, “Prediction of force and image artifacts under MRI for metals used in medical devices,” *IEEE/ASME Trans. Mechatronics*, vol. 18, no. 3, pp. 954–962, 2013.
- [18] D. Formica *et al.*, “Biological effects of exposure to magnetic resonance imaging: an overview,” *Biomed. Eng. Online*, vol. 3, no. 1, p. 11, 2004.
- [19] C. Landrigan, “Preventable Deaths and Injuries during Magnetic Resonance Imaging,” *N. Engl. J. Med.*, vol. 345, no. 13, pp. 1000–1001, Sep. 2001.
- [20] R. P. Klucznik, D. A. Carrier, R. Pyka, and R. W. Haid, “Placement of a ferromagnetic intracerebral aneurysm clip in a magnetic field with a fatal outcome,” *Radiology*, vol. 187, no. 3, pp. 855–856, Jun. 1993.
- [21] J. T. McFadden, “Magnetic resonance imaging and aneurysm clips,” *J. Neurosurg.*, vol. 117, no. 1, pp. 1–11, Jul. 2012.
- [22] R. D. Boutin, J. E. Briggs, and M. R. Williamson, “Injuries associated with MR imaging:

- survey of safety records and methods used to screen patients for metallic foreign bodies before imaging,” *AJR. Am. J. Roentgenol.*, vol. 162, no. 1, pp. 189–94, Jan. 1994.
- [23] G. Chaljub, L. A. Kramer, R. F. Johnson, R. F. Johnson, H. Singh, and W. N. Crow, “Projectile Cylinder Accidents Resulting from the Presence of Ferromagnetic Nitrous Oxide or Oxygen Tanks in the MR Suite,” *Am. J. Roentgenol.*, vol. 177, no. 1, pp. 27–30, Jul. 2001.
- [24] W. M. Kelly, P. G. Paglen, J. A. Pearson, A. G. San Diego, and M. A. Soloman, “Ferromagnetism of intraocular foreign body causes unilateral blindness after MR study.,” *AJNR. Am. J. Neuroradiol.*, vol. 7, no. 2, pp. 243–5.
- [25] “Establishing Safety and Compatibility of Passive Implants in the Magnetic Resonance (MR) Environment Guidance for Industry and Food and Drug Administration Staff,” 2014.
- [26] B. A. Schueler *et al.*, “MRI compatibility and visibility assessment of implantable medical devices,” *J. Magn. Reson. Imaging*, vol. 9, no. 4, pp. 596–603, Apr. 1999.
- [27] Nyenhuis, A. V. Kildishev, J. D. Bourland, K. S. Foster, and G. Graber, “Heating near implanted medical devices by the mri rf-magnetic field,” *IEEE Trans. Magn.*, vol. 35, no. 5 PART 2, pp. 4133–4135, 1999.
- [28] Y. M. Hwang *et al.*, “Cardiac Implantable Electronic Device Safety during Magnetic Resonance Imaging.,” *Korean Circ. J.*, vol. 46, no. 6, pp. 804–810, Nov. 2016.
- [29] J. S. Shinbane, P. M. Colletti, and F. G. Shellock, “Magnetic resonance imaging in patients with cardiac pacemakers: era of ‘MR Conditional’ designs.,” *J. Cardiovasc. Magn. Reson.*, vol. 13, no. 1, p. 63, Oct. 2011.
- [30] F. G. Shellock and V. J. Shellock, “Vascular access ports and catheters: Ex vivo testing of ferromagnetism, heating, and artifacts associated with MR imaging,” *Magn. Reson. Imaging*, vol. 14, no. 4, pp. 443–447, 1996.
- [31] R. Luechinger, F. Duru, M. B. Scheidegger, P. Boesiger, and R. Candinas, “Force and torque effects of a 1.5-Tesla MRI scanner on cardiac pacemakers and ICDs.,” *Pacing*

- Clin. Electrophysiol.*, vol. 24, no. 2, pp. 199–205, 2001.
- [32] F. G. Shellock and J. V. Crues, “High-field-strength MR imaging and metallic biomedical implants: An ex vivo evaluation of deflection forces,” *Am. J. Roentgenol.*, vol. 151, no. 2, pp. 389–392, 1988.
- [33] A. G. Gegauff, K. A. Laurell, A. Thavendrarajah, and S. F. Rosenstiel, “A potential MRI hazard: forces on dental magnet keepers,” *J. Oral Rehabil.*, vol. 17, no. 5, pp. 403–410, 1990.
- [34] T. R. Oskar Talcoth and T. Rylander, “Electromagnetic Modeling of Pacemaker Lead Heating During MRI,” 2011.
- [35] D. Martire, K. Wawrzyn, W. Handler, and B. Chronik, “Measuring Gradient-Induced Vibration of a Conductive Device using Laser Doppler Vibrometry at 3T,” in *24th Annual Meeting and Exhibition of ISMRM*, 2016, p. 3655.
- [36] J. Planert, H. Modler, and R. Vosshenrich, “Measurements of magnetism-related forces and torque moments affecting medical instruments, implants, and foreign objects during magnetic resonance imaging at all degrees of freedom,” *Med Phys*, vol. 23, no. 6, pp. 851–856, 1996.
- [37] A. M. Viano, S. A. Gronemeyer, M. Haliloglu, and F. A. Hoffer, “Improved MR imaging for patients with metallic implants,” *Magn. Reson. Imaging*, vol. 18, no. 3, pp. 287–295, 2000.
- [38] J. F. Schenck, “The role of magnetic susceptibility in magnetic resonance imaging: MRI magnetic compatibility of the first and second kinds,” *Med. Phys.*, vol. 23, no. 6, p. 815, 1996.
- [39] ASTM, “ASTM International - Standards Worldwide.” [Online]. Available: <https://www.astm.org/Standards/medical-device-and-implant-standards.html>.
- [40] ASTM F2052 – 15, “Standard Test Method for Measurement of Magnetically Induced Displacement Force on Medical Devices in the Magnetic Resonance,” *ASTM Int.*, vol. 3, pp. 1–6, 2002.

- [41] ASTM F2213 – 06, “Standard Test Method for Measurement of Magnetically Induced Torque on Medical Devices in the Magnetic Resonance Environment,” *ASTM Int.*, vol. 6, no. Reapproved 2011, pp. 1–8, 2012.
- [42] ASTM F2119 – 07, “Standard Test Method for Evaluation of MR Image Artifacts from Passive Implants,” *ASTM Int.*, vol. 7, no. Reapproved 2013, pp. 1–4, 2013.
- [43] ASTM F2128-11a, “Measurement of Radio Frequency Induced Heating On or Near Passive Implants During Magnetic Resonance Imaging,” *ASTM Int.*, 2011.
- [44] D. J. Griffiths, *Introduction to Electrodynamics*, Third Edit. Pearson Education, 1999.
- [45] H. Imai *et al.*, “Three-dimensional quantification of susceptibility artifacts from various metals in magnetic resonance images,” *Acta Biomater.*, vol. 9, no. 9, pp. 8433–8439, Sep. 2013.
- [46] S.-P. Hong, Y.-M. Ko, and C.-S. Kim, “Magnetic Susceptibility of Zr-Cu Binary Alloys,” *Mater. Trans.*, vol. 55, no. 10, pp. 1634–1636, 2014.
- [47] M. Zborowski, G. R. Ostera, L. R. Moore, S. Milliron, J. J. Chalmers, and A. N. Schechter, “Red blood cell magnetophoresis,” *Biophys. J.*, vol. 84, no. 4, pp. 2638–45, Apr. 2003.
- [48] J. A. Hopkins and F. W. Wehrli, “Magnetic susceptibility measurement of insoluble solids by NMR: Magnetic susceptibility of bone,” *Magn. Reson. Med.*, vol. 37, no. 4, pp. 494–500, Apr. 1997.
- [49] B. L. Morris and A. Wold, “Faraday Balance for Measuring Magnetic Susceptibility,” *Rev. Sci. Instrum.*, vol. 39, no. 12, p. 1937, 1968.
- [50] C. Piguet, “Paramagnetic Susceptibility by NMR: The ‘Solvent Correction’ Removed for Large Paramagnetic Molecules,” *J. Chem. Educ.*, vol. 74, no. 7, p. 815, Jul. 1997.
- [51] H. B. Gray, D. N. Hendrickson, and Y. S. Sohn, “Magnetic susceptibility study of various ferricenium and iron(III) dicarbollide compounds,” *Inorg. Chem.*, vol. 10, no. 8, pp. 1559–

- 1563, Aug. 1971.
- [52] W. M. Spees, D. A. Yablonskiy, M. C. Oswood, and J. J. H. Ackerman, “Water proton MR properties of human blood at 1.5 Tesla: Magnetic susceptibility, T<sub>1</sub>, T<sub>2</sub>, T<sub>2</sub>\*2, and non-Lorentzian signal behavior,” *Magn. Reson. Med.*, vol. 45, no. 4, pp. 533–542, Apr. 2001.
- [53] J. B. Greene and F. G. Karioris, “Force on a Magnetic Dipole,” *Am. J. Phys.*, vol. 39, no. 2, p. 172, 1971.
- [54] H. E. Knoepfel, *MAGNETIC FIELDS A Comprehensive Theoretical Treatise for Practical Use*. New York: WILEY, 2000.
- [55] T. H. Boyer, “The Force on a Magnetic Dipole,” *Am. J. Phys.*, vol. 56, no. 8, pp. 688–692, 1988.
- [56] E. M. Haacke, R. W. Brown, M. R. Thompson, and R. Venkatesan, *Magnetic Resonance Imaging: Physical Principles and Sequence Design*, vol. 1st. 1999.
- [57] D. W. McRobbie, E. A. Moore, M. J. Graves, and M. R. Prince, *MRI From Picture To Proton*, 2nd ed. New York: Cambridge, 2006.
- [58] M. M. Elwassif *et al.*, “Temperature control at DBS electrodes using a heat sink: experimentally validated FEM model of DBS lead architecture,” *J. Neural Eng.*, vol. 9, no. 4, p. 46009, Aug. 2012.
- [59] S. O. McCabe and J. B. Scott, “Cause and Amelioration of MRI-Induced Heating Through Medical Implant Lead Wires,” *21st Electron. New Zeal. Conf.*, 2014.
- [60] J. Ruoff, C. Würslin, H. Graf, and F. Schick, “Resolution adapted finite element modeling of radio frequency interactions on conductive resonant structures in MRI,” *Magn. Reson. Med.*, vol. 67, no. 5, pp. 1444–1452, May 2012.
- [61] S. A. Mohsin, J. A. Nyenhuis, and R. Masood, “Interaction Of Medical Implants With The MRI Electromagnetic Fields,” *Prog. Electromagn. Res. C*, vol. 13, pp. 195–202, 2010.
- [62] G. Strang and G. Fix, *An Analysis of the Finite Element Method*, Second Edi. Wellesley-Cambridge, 2008.

- [63] COMSOL INC., “Multiphysics Simulation Software - Platform for Physics-Based Modeling,” [www.comsol.com/comsol-multiphysics](http://www.comsol.com/comsol-multiphysics), 2014.
- [64] The Mathworks Inc., “MATLAB - MathWorks,” [www.mathworks.com/products/matlab](http://www.mathworks.com/products/matlab), 2016. [Online]. Available: <http://www.mathworks.com/products/matlab/>.
- [65] Python Software Foundation, “Python Language Reference, version 2.7,” *Python Software Foundation*. 2013.
- [66] K. Trapp, L. Käfer, and D. Bähre, “Effects of Machining Ferromagnetic Materials on Magnetic Property Changes,” *Procedia Manuf.*, vol. 1, pp. 721–727, 2015.
- [67] D. E. Neuenschwander, *Tensor Calculus for Physics*. John Hopkins University Press, 2014.
- [68] X. Fei, V. W. Hughes, and R. Prigl, “Precision measurement of the magnetic field in terms of the free-proton NMR frequency,” *Nucl. Instruments Methods Phys. Res. Sect. A Accel. Spectrometers, Detect. Assoc. Equip.*, vol. 394, no. 3, pp. 349–356, 1997.
- [69] K. Borer and G. Frémont, “The nuclear magnetic resonance magnetometer type 9298,” *Nucl. Instruments Methods*, vol. 154, no. 1, pp. 61–82, 1978.
- [70] N. De Zanche, C. Barmet, J. A. Nordmeyer-Massner, and K. P. Pruessmann, “NMR probes for measuring magnetic fields and field dynamics in MR systems,” *Magn. Reson. Med.*, vol. 60, no. 1, pp. 176–186, Jul. 2008.
- [71] G. Boero, J. Frounchi, B. Furrer, P.-A. Besse, R. S. Popovic, and J Frounchi, “Fully integrated probe for proton nuclear magnetic resonance magnetometry,” vol. 72, 2001.
- [72] M. E. Stoll and T. J. Majors, “Reduction of magnetic susceptibility broadening in NMR by susceptibility matching,” *J. Magn. Reson.*, vol. 46, no. 2, pp. 283–288, 1982.

## Appendix A: ASTM F2052-15 Magnetic Force Deflection Test

As per ASTM F2052-15, testing of magnetic force is conducted using the magnetic fields produced by an MR system. The device-under-test (DUT) is suspended by a string of negligible weight at a location near the entrance of the bore. The DUT must be positioned such that after any deflection, the DUT is on the axis of the bore at a location of known field and field gradient. Because the test location is along the axis of the scanner, the magnetic field is known to have a single component (parallel to the axis). The angular deflection of the device at this location is used to obtain a measurement of the magnetic force in relation to the force of gravity on that object. If the mass of the object is known, the magnetic force can be calculated from the deflection angle. Because the test is conducted at a location of well-characterized magnetic field, the expected magnetic force for other magnetic field environments (specifically, other combinations of magnetic field and magnetic field gradient) can be extrapolated from the results.

Because the magnetic force is generally larger for higher magnetic fields, a 3 T system is used. For the 3 T system, the angular deflection of the string is measured at a distance of 0.8 m from the isocenter of the system, and at a height of 0.3 m from the top of the bore.



**Figure 18** - Force deflection test conducted for a 10 cm rod of 316 stainless steel in a 60-cm bore 3 T MRI system (Siemens Prisma). In this case, the 10 cm rod is suspended by a string at a location of 0.8 m from the isocenter of the system, and at a height of 0.3 m from the top of the bore (i.e. along the central axis of the system). The string is fixed to a protractor which is rigidly mounted to the test fixture with the 0° mark of the protractor oriented vertically. Magnetic force on the object is calculated based on the angle of deflection measured [40].

The test fixture consists of a sturdy nonmagnetic structure which holds the test device in position and contains a protractor accurate to  $1^\circ$  rigidly mounted to the structure. The  $0^\circ$  mark of the protractor is oriented vertically. The medical device is suspended from a thin string, whose weight is less than 1% of the weight of the device, that is attached to the  $0^\circ$  mark of the protractor. The test location is at the entrance of the MR system bore and on the axis of the bore.

The test device is suspended from the string and is positioned such that the device's center of mass is located at a distant of 0.8 m from the isocenter of the system and at a height of 0.3 m from the top of the bore, Figure 18. The deflection angle,  $\alpha$ , is recorded alongside the magnitude of the  $\mathbf{B}$  field and spatial gradient of the  $\mathbf{B}$  field. The test process is repeated a minimum of three times per device.

## Appendix B: Derivation of Magnetic Force Equation

This appendix will demonstrate that when the magnetic moment is spatially dependent, equations (B.1) and (B.2) are not equal. A derivation of the magnetic force equation introduced in 1.3.4 and used throughout this thesis, equation (B.2), is presented.

The force on a magnetic dipole moment is described in [44] as

$$\mathbf{F} = \nabla(\mathbf{m} \cdot \mathbf{B}) \quad (\text{B.1})$$

which has been cited to be the same as equation (B.2)

$$\mathbf{F} = (\mathbf{m} \cdot \nabla)\mathbf{B} \quad (\text{B.2})$$

when  $\mathbf{J} = \frac{\partial \mathbf{E}}{\partial t} = 0$  [55].

This is in fact not the case, and can be demonstrated by using the identity:

$$\nabla(\mathbf{A} \cdot \mathbf{C}) = (\mathbf{A} \cdot \nabla)\mathbf{C} + (\mathbf{C} \cdot \nabla)\mathbf{A} + \mathbf{A} \times (\nabla \times \mathbf{C}) + \mathbf{C} \times (\nabla \times \mathbf{A}) \quad (\text{B.3})$$

such that equation (B.2) can be expressed as equation (B.3).

$$\nabla(\mathbf{m} \cdot \mathbf{B}) = (\mathbf{m} \cdot \nabla)\mathbf{B} + (\mathbf{B} \cdot \nabla)\mathbf{m} + \mathbf{m} \times (\nabla \times \mathbf{B}) + \mathbf{B} \times (\nabla \times \mathbf{m}) \quad (\text{B.4})$$

From equation (B.5),

$$\nabla \times \mathbf{B} = \mu_0 \left( \mathbf{J} + \epsilon_0 \frac{\partial \mathbf{E}}{\partial t} \right) \quad (\text{B.5})$$

in the case where  $\mathbf{J} = \frac{\partial \mathbf{E}}{\partial t} = 0$ ,  $\nabla \times \mathbf{B} = 0$ . This eliminates the third term of equation (B.4).

Additionally, since the magnetic moment can be written in terms of  $\mathbf{B}$ , equation (B.12), the fourth term also becomes 0. Equation (B.4) then simplifies to equation (B.6).

$$\nabla(\mathbf{m} \cdot \mathbf{B}) = (\mathbf{m} \cdot \nabla)\mathbf{B} + (\mathbf{B} \cdot \nabla)\mathbf{m} \quad (\text{B.6})$$

Using equations (B.7), (B.8), (B.9) and (B.10),

$$\mathbf{B} = \mu_0(\mathbf{H} + \mathbf{M}) \quad (\text{B.7})$$

$$\mathbf{m} = \mathbf{M}dV \quad (\text{B.8})$$

$$\mathbf{M} = \chi\mathbf{H} \quad (\text{B.9})$$

$$\mathbf{B} = \mu\mathbf{H} \quad (\text{B.10})$$

$\mathbf{B}$  can be written as

$$\mathbf{B} = \mu_0\mathbf{m} \frac{1 + \chi}{\chi dV} \quad (\text{B.11})$$

or

$$\mathbf{B} = k\mathbf{m} \quad (\text{B.12})$$

where  $k$  is a constant.

$$k = \mu_0 \frac{1 + \chi}{\chi dV} \quad (\text{B.13})$$

Substituting  $\mathbf{B}$  for  $k\mathbf{m}$  in equation (B.6),

$$\nabla(\mathbf{m} \cdot \mathbf{B}) = (\mathbf{m} \cdot \nabla)k\mathbf{m} + (k\mathbf{m} \cdot \nabla)\mathbf{m} \quad (\text{B.14})$$

collecting terms,

$$\nabla(\mathbf{m} \cdot \mathbf{B}) = 2(k\mathbf{m} \cdot \nabla)\mathbf{m} \quad (\text{B.15})$$

and substituting  $k$ , equation (B.2) does not in fact equal equation (B.1) in the case where the magnetic moment is spatially dependent.

$$\nabla(\mathbf{m} \cdot \mathbf{B}) = 2(\mathbf{m} \cdot \nabla)\mathbf{B} \quad (\text{B.16})$$

In the case where the magnetic moment is spatially independent, then the second term of equation (B.4) would also be 0 since  $\nabla\mathbf{m} = 0$ , and  $\nabla(\mathbf{m} \cdot \mathbf{B})$  would in fact equal  $(\mathbf{m} \cdot \nabla)\mathbf{B}$ . The factor of two discrepancy in equation (B.16) comes from the dependence the magnet moment has on the magnetic flux density. A full derivation of equation (B.2) will make this clear.

From the Lorentz force,

$$\mathbf{F} = I \oint d\mathbf{l} \times (\mathbf{r} \cdot \nabla)\mathbf{B} \quad (\text{B.17})$$

where the integration path is any closed loop that encloses the current  $I$  exactly once. Using Levi-Civita notation to represent the dot and cross product, this can be expressed as equation (B.18) [67].

$$F_i = I \sum_{j,k,l} \epsilon_{ijk} \oint r_l dl_j \nabla_l B_k \quad (\text{B.18})$$

If we assume  $\nabla B_k$  is constant then,

$$\oint \nabla_l B_k r_l dl_j = \mathbf{a} \times \nabla B_k \quad (\text{B.19})$$

where  $\mathbf{a}$  is the vector area previously defined in 1.3. Again using Levi-Civita notation,

$$\sum_l \oint r_l \nabla B_k dl_j = \sum_{m,n} \epsilon_{jmn} a_m (\nabla B_k)_n \quad (\text{B.20})$$

and plugging this back into equation (B.18)

$$F_i = I \sum_{j,k,m,n} \epsilon_{ijk} \epsilon_{jmn} a_m (\nabla B_k)_n \quad (\text{B.21})$$

force can be expressed as equation (B.22).

$$F_i = I \sum_k a_k (\nabla B_k)_i - I \sum_k a_i (\nabla B_k)_k \quad (\text{B.22})$$

Where the magnetic moment is given by equation (B.23),

$$\mathbf{m} = I \mathbf{a} \quad (\text{B.23})$$

and the second term of equation (B.22) becomes 0 since  $\nabla \cdot \mathbf{B} = 0$ , then

$$F_i = \sum_k m_k \nabla (B_k)_i \quad (\text{B.24})$$

which gives equation (B.2).

$$\mathbf{F} = (\mathbf{m} \cdot \nabla) \mathbf{B} \quad (\text{B.2})$$

Where  $\mathbf{m}$  is spatially independent,  $m_k$  can be brought into the gradient operation of equation (B.24),

$$F_i = \sum_k \nabla(m_k B_k)_i \quad (\text{B.25})$$

which is equivalent to equation (B.1), and actually how equation (B.1) is derived [44]. However, for magnetic materials, where  $\mathbf{m}$  is spatially dependent, bringing in  $m_k$  would be invalid. In this case,  $\mathbf{m}$  has the same spatial dependence as  $\mathbf{B}$  and therefore would result in an extra factor of two if it were brought into the gradient operation of equation (B.24), as seen in equation (B.16).

For magnetic materials, where  $\mathbf{m}$  is dependent on the magnetic flux density, and therefore spatially dependent, equation (B.2) should be used. As this thesis focuses on examining the static magnetic field interactions experienced by medical devices, which are magnetic materials, it uses equation (B.2).

## Appendix C: Certificates of Tests for Stainless Steel Rods

outokumpu  
high performance stainless steel



## Certificate of Test

Page: 1

HEAT E141755 ORDER 655495/ 03 BOL 0230961 \* CERTIFICATION \* 02/10/15

SHIP TO:  
ROLLED ALLOYS BAR CENTER  
711 PHOENIX LAKE AVENUE

STREAMWOOD 601070000

TRACER # 044675US

----- YOUR ORDER & DATE -----  
0118640-STR 10/29/14 CUST# 0773001 CUST TAG#0009259

----- ITEM DESCRIPTION -----  
GRADE 316L/316 Ship Condition CONDA  
Size 316L RND CDA CONDA .5000 x 144.080 RL  
Country of Melt: UNITED KINGDOM Country of Mfg.: UNITED STATES  
NAFTA Country of Origin is Country of Melt

No weld repair  
Free of mercury contamination, Free of radiation contamination  
No WEEE relevant substances; Meets EU electrical ROHS

Total Bundles 1 Total Weight 2150 Approx. Hot Red. Ratio 133:1

WO 2053930 Bundles: 1D

----- SPECIFICATIONS -----  
MFG TO FINISHED BAR IN THE USA FROM BILLETS IMPORTED UNITED KINGDOM  
AMS 5648L, 5653H SAE AMS-00-S-763C  
ASME SA182 2007-2013 Ed ASME SA193 2013 Edition  
ASME SA479 2007-2013 Ed. ASME SA320 B8M CL1, 2013 Ed.  
ASTM A182 13a ASTM A262 13 Practice A/E  
ASTM A276-15 ASTM A374 13a  
ASTM A479/A479M 14 ASTM A484 14a  
ASTM A320 11 B8M Class 1 ASTM A193 14 B8M  
NACE-MR0175-09, ISO 15156:09 DFARS 252.225.7009 10/4/11  
Federal Spec QQ-S-763F US S31600, AISI 316  
UNS S31603, AISI 316L Prodec Quality  
EN 10204 Type 3.1 Document RA-S3 RAM 316L  
EN 10272 GR 1, 4404 chemistry Butech BU-36 Rev 2  
DFARS 225.7002-3(B)(1) WAGE MR0103-10  
Sol Ann 1900F min/WQ Bars are Eddy Current tested

----- MECHANICAL & OTHER TESTS -----  
Hardness as shipped 213 HB  
Hardness as shipped ( 94 HRB )  
Grain size 5.0 Tensile strength, KSI (MPa) 99.0 ( 683 )  
Micro OK 0.2% Yield Strngth, KSI (MPa) 78.5 ( 541 )  
Intergranular corrosion OK  
Elongation % in 4D 44.0  
Reduction of area % 76.0

-- Continued --



## Certificate of Test

Page: 2

HEAT E141755 ORDER 655495/ 03 BOL 0230961 \* CERTIFICATION \* 02/10/15

SHIP TO:  
ROLLED ALLOYS BAR CENTER  
711 PHOENIX LAKE AVENUE

STREAMWOOD 601070000

CHEMICAL COMPOSITION			
Carbon (C)	.018	Manganese (Mn)	1.650
Phosphorus (P)	.029	Sulphur (S)	.024
Silicon (Si)	.600	Chromium (Cr)	16.670
Nickel (Ni)	10.150	Cobalt (Co)	.431
Copper (Cu)	.460	Moly (Mo)	2.060
Nitrogen (N)	.051	Columbium (Cb)	.030
Titanium (Ti)	.003	Aluminum (Al)	.005
Tin (Sn)	.007	Tantalum (Ta)	.002
Vanadium (V)	.060	Tungsten (W)	.150
Columbium/ Tantalum (Cb+Ta)	.032		
Iron (Fe)	Balance		
Melt Practice	EAF		
Refining Practice	AOD		
De-long Ferrite	3.8		

Knowingly & willfully falsifying or concealing a material act on this form, or making false, fictitious or fraudulent statements or representations herein could constitute a felony punishable under federal statutes. We hereby certify that the test results shown in this report are correct and accurate as contained in the records of the company and are in compliance with the specifications, codes, and standards listed above.

M. E. Mercurio Quality Manager

ROLLED ALLOYS QUALITY ASSURANCE
APPROVED [REDACTED]
DATE 12 Feb 2015

HEAT # E141755



TRACER # 0444875US



# Certificate of Test

Page: 1

HEAT E150968 ORDER 661945/ 02 BOL 0234163 \* CERTIFICATION \* 12/10/15

SHIP TO:  
ROLLED ALLOYS BAR CENTER  
711 PHOENIX LAKE AVENUE

STREAMWOOD 601070000

----- YOUR ORDER & DATE -----  
0129308-STR 9/11/15 CUST# 0773001 CUST TAG#0009069----- ITEM DESCRIPTION -----  
GRADE 304L Ship Condition CONDA  
Size 304L RND CDA CONDA .5000 x 144.000 RL  
Country of Melt: UNITED KINGDOM Country of Mfg.: UNITED KINGDOM  
NAFTA Country of Origin is Country of Melt  
No weld repair  
Free of mercury contamination, Free of radiation contamination  
No WEEE relevant substances; Meets EU electrical ROHS

Total Bundles 2 Total Weight 4206 Approx. Hot Red. Ratio 133:1

WO 2063353 Bundles: 1G, 1H

-----  
AMS 5639H, 5647J  
ASME SA182 2007-2015 Ed  
ASME SA484 2015 Ed.  
ASME SA193 B8 2015 Edition  
ASTM A262 15 Practice A/E  
ASTM A314 15  
ASTM A484 15  
ASTM A193 15 B8  
NACE MR0175-09, ISO 15156:09  
Federal Spec QQ-S-763F  
UNS S30403, AISI 304L  
Prodec Quality  
EN 10204 Type 3.1 Document  
NACE MR0103-10  
QTC is a prolongation of bar  
Bars are Eddy Current tested

## ----- SPECIFICATIONS -----

SAE AMS-00-S-763D  
ASME SA479 2007-2015 Ed.  
ASME SA320 B8 Cl1, 2015 Ed.  
ASTM A182 15  
ASTM A276-15  
ASTM A479/A479M 15  
ASTM A320 11 B8 Class 1  
Solution Annealed Condition  
DFARS 252.225.7009 10/4/11  
UNS S30400, AISI 304  
Free of Cont. carbide network  
RA-53 RAM 304L  
ASTM F899 12  
ASTM F899 12  
Sol Ann 1900F min/WQ----- MECHANICAL & OTHER TESTS -----  
Hardness as shipped (217 HB )  
Hardness as shipped 95 HRB  
Grain size 4.0  
Micro OK  
Intergranular corrosion OK  
Tensile strength, KSI (MPa) 107.0 ( 738 )  
0.2% Yield Strength, KSI (MPa) 85.4 ( 589 )  
1% Yield Strength, KSI (MPa) 99.6 ( 687 )  
Elongation % in 4D 48.0  
Elongation % in 5D 46.7  
Reduction of area % 69.0

-- Continued --

HEAT # E150968



TRACER # 0468355US



## Certificate of Test

Page: 2

HEAT E150968 ORDER 661945/ 02 BOL 0234163 \* CERTIFICATION \* 12/10/15

SHIP TO:  
ROLLED ALLOYS BAR CENTER  
711 PHOENIX LAKE AVENUE

STREAMWOOD 601070000

----- CHEMICAL COMPOSITION -----			
Carbon (C)	.026	Manganese (Mn)	1.780
Phosphorus (P)	.033	Sulphur (S)	.026
Silicon (Si)	.280	Chromium (Cr)	18.130
Nickel (Ni)	8.090	Cobalt (Co)	.164
Copper (Cu)	.660	Moly (Mo)	.400
Nitrogen (N)	.078	Columbium (Cb)	.020
Titanium (Ti)	.002	Aluminum (Al)	.005
Tin (Sn)	.012	Boron (B)	.001
Tantalum (Ta)	.001	Vanadium (V)	.070
Tungsten (W)	.030		.000
Columbium/ Tantalum (Cb+Ta)	.021		
Iron (Fe)	Balance		
Melt Practice	EAF		
Refining Practice	AOD		
De-long Ferrite			

Knowingly & willfully falsifying or concealing a material act on this form, or making false, fictitious or fraudulent statements or representations herein could constitute a felony punishable under federal statutes. We hereby certify that the test results shown in this report are correct and accurate as contained in the records of the company and are in compliance with the specifications, codes, and standards listed above.

M. F. Marcano, Quality Manager

HEAT # E150968



TRACER # 0468355US

Receiving Inspection  
By:   
Date: 12-10-11

## Appendix D: Measured Magnetic Field Data for 3T MRI System

Distance from isocentre, $z$ [m] $\pm 0.5$ mm	$B_z$ [T] $\pm 0.1$ mT	Distance from isocentre, $z$ [m] $\pm 0.5$ mm	$B_z$ [T] $\pm 0.1$ mT
1000.00	1.478	810.00	2.268
990.00	1.521	800.00	2.305
980.00	1.559	790.00	2.341
970.00	1.604	780.00	2.378
960.00	1.644	770.00	2.412
950.00	1.687	760.00	2.448
940.00	1.729	750.00	2.480
930.00	1.775	740.00	2.510
920.00	1.815	730.00	2.541
910.00	1.859	720.00	2.571
900.00	1.901	710.00	2.600
890.00	1.941	700.00	2.626
880.00	1.986		
860.00	2.069		
850.00	2.112		
840.00	2.150		
830.00	2.191		
820.00	2.230		

**Table 4** –  $B_z$  field as a function of  $z$  down the center on axis line of a 3T MRI (Siemens Prisma) as measured by a Hall-effect magnetic field probe.  $Z$  position is measured as the distance from the isocenter where the isocenter is defined as  $z=0$ . Data points were measured with sample spacing of 10 mm. All uncertainties are estimated.

## **Appendix E: Investigation of the Effects of Foreign Magnetic Materials Positioned Outside an MRI System on the Main Field Homogeneity of that System**

This Appendix describes a project related to, but separate from the primary thesis work described in Chapters 2 through 4. The objective of this project was to simulate the effects that relatively large amounts of magnetic material, placed outside a realistic model of an MRI magnet, would have on the homogeneity of that magnet. This project was conducted as part of an industry-sponsored internship. The objective of the industry partner was to develop a systematic method for analyzing the potential effects that magnetic materials in MRI installations would have on their system performance.

The reason this Appendix is included in this thesis is that this project leveraged many of the same simulation tools as those developed to model magnetic forces on medical devices. To the extent that these tools become validated for the application described in this appendix, this project would serve to support the validity of the tools for use in the medical device application described in Chapters 2 through 4. Furthermore, this project required the additional step of producing a simulation of a full 3D model of a realistic MRI system, and as such represented an additional challenge to the methods developed in the primary thesis.

MRI relies on the assumption that the main field is stable and homogeneous, and deviations from homogeneity will result in image artifacts to varying degrees depending on the specific MR imaging methods employed [37]. When planning and evaluating facilities in which an MR system will be placed, one must often consider the effects of surrounding magnetic materials on the homogeneity of the main field. As one example, in the construction and planning of a MR installation, the addition of a steel plate in the floor may be considered with the objective of reducing the stray fields beyond the plate. This is a form of passive magnetic shielding employed in various ways in some MRI system installations.

In this work the objective was to investigate the effect a non-linear magnetic steel plate placed below a MR scanner would have on the homogeneity of the magnetic field within the imaging

region of that realistic scanner model. A secondary objective was to provide a systematic means of evaluating site-planning choices on MR system performance prior to installation.

## E.1 Magnet Design

A simple Helmholtz coil was selected in order to in some way validate the use of *COMSOL Multiphysics* in this application. In principle an MR scanner main magnet can be simplified as a Helmholtz coil. The reason for considering this is that there is a known analytic solution for the magnetic field produced down the axis of a Helmholtz coil. By simulating the field produced by a Helmholtz coil to the corresponding analytic solution, the use of *COMSOL* can be partially validated. With this partial validation of *COMSOL* complete, a more realistic actively shielded magnet may be modeled with much more confidence.

All design, modeling, and simulations were performed in *COMSOL Multiphysics* using the ‘Magnetic Fields, mf’ package. For each simulation, all coil geometries were placed in a spherical infinite element domain of air. Simulation data was exported from all the simulations and the data was imported into *MATLAB* in order to enable visualization and further analysis.

### E.1.1 Methods for Modeling of Helmholtz Coil

The coils of the Helmholtz pair were designed using circular regions formed in the geometry, using ‘work plane - plane geometry – circle’. The ‘edge current’ function within the ‘Magnetic Fields, mf’ package of *COMSOL* was used to assign 10 turns of 100 A of current to the coils. The details of the coils are found in Table 5.

Coil	Position in (x,y) plane, z [m]	Radius, $R$ [m]	Turns, $n$	Current, $I$ [A]
1	-0.25	0.5	10	100
2	0.25	0.5	10	100

**Table 5** - Specifications of the current carrying coils used to define a Helmholtz pair in a *COMSOL* simulation. The radius, number of turns, and current were arbitrarily chosen. Coil position was constrained such that the distance between the coils was equal to  $R$ .

Meshing of the coils was performed with free tetrahedrals, while the outer domains of the spherical infinite element domain employed a swept mesh.

As shown in the introduction, 1.5.1, the field at the isocenter of a Helmholtz coil is given by:

$$\mathbf{B} = \left(\frac{4}{5}\right)^{\frac{3}{2}} \frac{\mu_0 n I}{R} \hat{\mathbf{z}} \quad (26)$$

and the field down the center of the coil, is now given by

$$\mathbf{B}(z) = \frac{\mu_0 I R^2 n}{2(R^2 + (z - l)^2)^{3/2}} \hat{\mathbf{z}} + \frac{\mu_0 I R^2 n}{2(R^2 + (z + l)^2)^{3/2}} \hat{\mathbf{z}} \quad (27)$$

where  $l$  is the distance between the coil and the  $xy$ -plane; for a Helmholtz coil centered around the  $z = 0$ ,  $xy$ -plane,  $l = R/2$ .

Equations (26) and (27) were solved using the same coil position, radius, current and number of windings as listed in Table 5.

## E.1.2 Methods for Modeling Actively Shielded MRI Magnet

A representative actively shielded magnet was modeled in *COMSOL*. The magnet consisted of seven inner coils and an additional two outer shielding coils. The example magnet design parameters were provided by Synaptive Medical Inc.

The coil geometries were each designed using a combination of the ‘work plane’ and ‘revolve’ functions in *COMSOL*. The coils were then defined using the ‘Coil’ function within the ‘Magnetic Fields, mf’ package of *COMSOL* with ‘Homogenized Multi-Turn Coils’ to include the effect of finite spatial windings. The current in all windings was adjusted to 137.75 A, such that the main field had a value of 0.5 T within 0.3 mT. All geometries were meshed using a free tetrahedral mesh.

## E.1.3 Results for Modeling of Helmholtz Coil

The magnetic flux density produced by the *COMSOL* model of a Helmholtz coil is shown in Figure 19, in the  $x = 0$ ,  $y$ - $z$  plane. The field is close to uniform in what would be the imaging

region of the modeled scanner, is at its greatest intensity near the windings, and falls off quickly outside the windings.

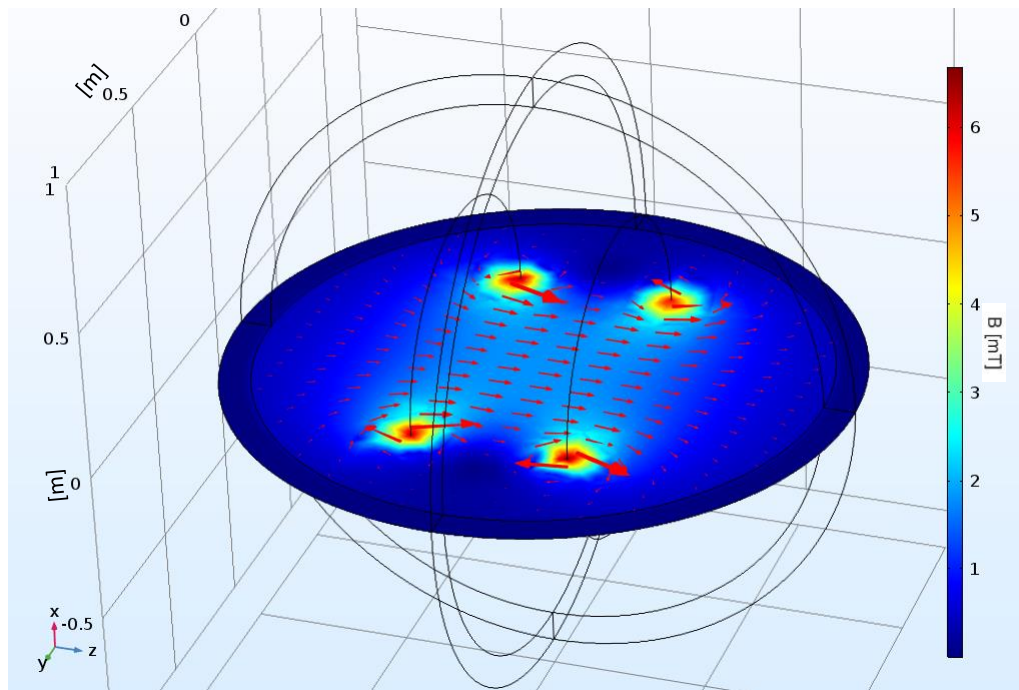


**Figure 19** – Magnetic flux density along the  $x = 0$ ,  $y$ - $z$  plane for a simulation of a Helmholtz coil of radius 0.5 m, current 100 A, and 10 wire turns within *COMSOL*. Simulation computed using the ‘Magnetic Fields, mf’ package of *COMSOL* within a spherical infinite element domain. Arrows indicate direction of field.

Figure 20 is a plot comparing the simulation data of a Helmholtz coil to the analytic solution of that same coil for the line through the coil axis. Figure 21 is a plot of the percent difference between the analytic solution and the simulation data.

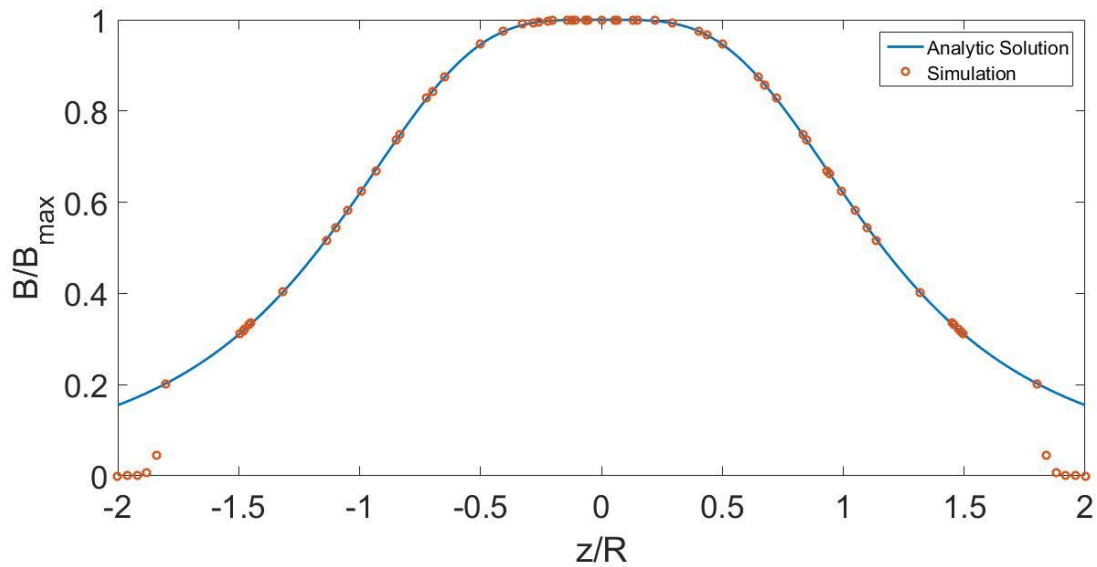


**Figure 20** – Magnetic flux density as a function of  $z$  for a Helmholtz coil of radius 0.5 m, current 100 A, and 10 wire turns. Analytic solution and *COMSOL* simulation results shown. The simulation data falls off as the data extends into the infinite element domain which begins at  $1.8 z/R$ . As the data moves into the infinite element domain it will exponentially decrease to 0. The horizontal axis is normalized to the coil radius and the vertical axis is normalized to the maximum value of  $\mathbf{B}(z)$ .

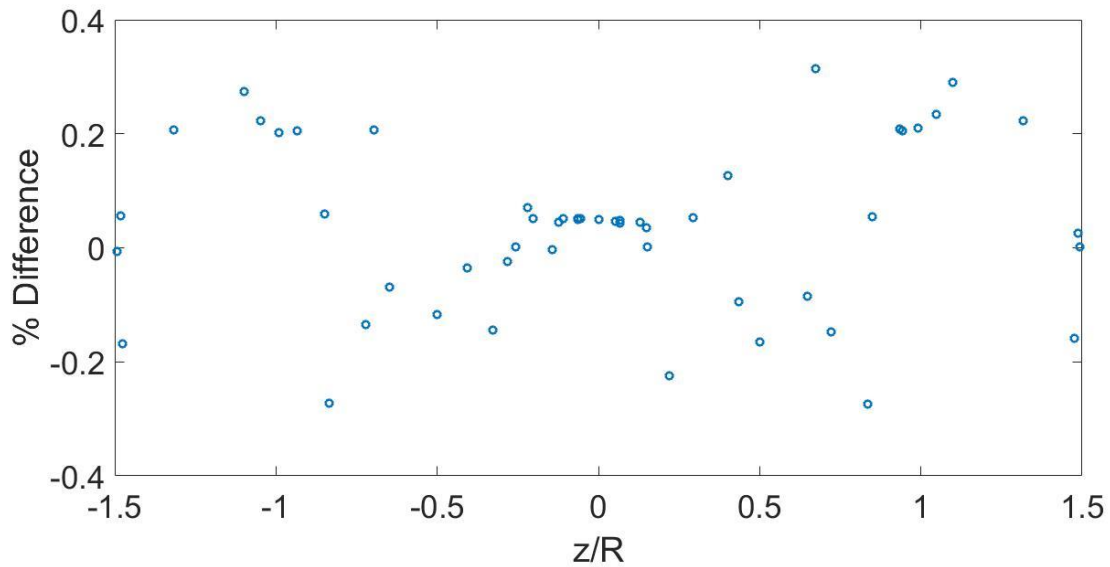


**Figure 21** – Percent difference when comparing the magnetic flux density as a function of  $z$  for a simulated Helmholtz coil to an analytic solution of the same Helmholtz coil of radius 0.5 m, current 100 A, and 10 wire turns. The horizontal axis limits are truncated to 1.5  $z/R$  in order to remove data points within the infinite element region. As the data moves into the infinite element domain it will exponentially decrease to 0. Percent difference in this region gives no information. The horizontal axis is normalized to the coil radius and the vertical axis is normalized to the maximum value of  $\mathbf{B}(z)$ .

#### E.1.4 Results for Modeling Actively Shielded MRI Magnet

The resultant magnetic flux density profile from the modeled MR magnet is shown in Figure 22. Figure 23 is a plot of the magnetic flux density as a function of  $z$  position down the center line of the scanner.

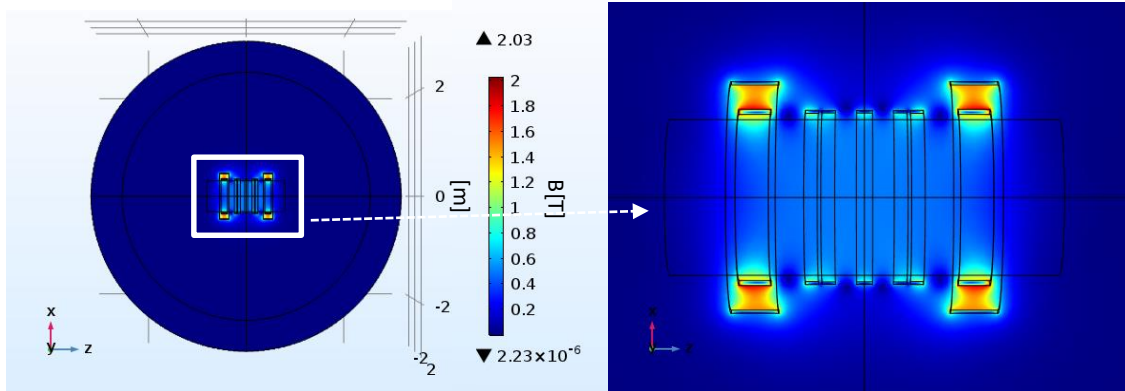


**Figure 22** – Magnet flux density profile produced by a *COMSOL* model of a standard actively shielded MR main magnet. The magnet consisted of seven inner coils and an additional two outer shielding coils. The current was adjusted such that the main field had a value of 0.5T within 0.3 mT. Simulation computed using the ‘Magnetic Fields, mf’ package of *COMSOL* within a spherical infinite element domain. (Left) Magnetic flux density shown along the  $y = 0$ ,  $x$ - $z$  plane. (Right) Zoomed in to better visualize the magnet flux density profile within the ‘bore’ and coils.

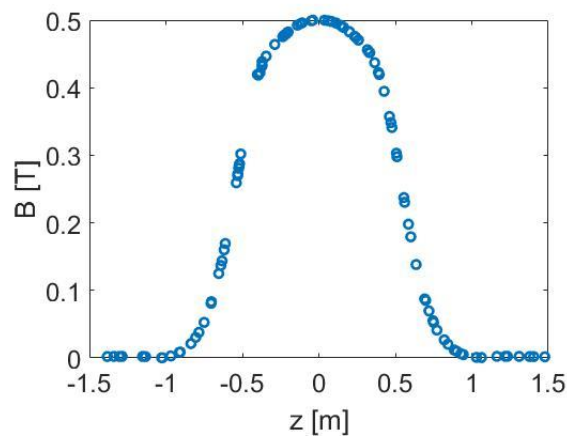


**Figure 23** – Magnet flux density along the  $z$ -axis for a *COMSOL* model of the example actively shielded MR main magnet. The magnet consisted of seven inner coils and an additional two outer shielding coils of finitely winded coil. The current was adjusted such that the main field had a value of 0.5 T within 0.3 mT.

## E.2 Investigation of Main Field Homogeneity in Presence of Foreign Materials

In this section the magnetic modeling methods presented above are used to model the additional effects of externally located magnetic materials could have on the field produced within the imaging region of the simple magnet model. Specifically, the effect of a large plate is considered. The materials of the plate were varied, and the effect the plate had on the uniformity of the main magnetic field profile were investigated. To begin with the plate was assumed to be a linear magnetic material (a material whose susceptibility is constant and independent of magnetic field strength). Following that a more complex non-linear magnetic material was modeled.

### E.2.1 Methods

All design, modeling and simulations were performed in *COMSOL Multiphysics* using the ‘Magnetic Fields, mf’ package. Magnet design and model from E.1.2 was employed. A plate of thickness 4 mm, and dimensions 3.0 m by 2.5 m was added to the model at a position of  $y = -1.0$  m as shown in Figure 24. Simulation data was exported from the simulations and all data analysis was performed in *MATLAB*. In order to investigate the effect of the addition of the plate, the background field (i.e. the field in the case that no plate is present) was subtracted from all data sets. Data from each simulation was interpolated onto a 1-mm isotropic grid using *MATLAB*. From this grid the background field was subtracted from the data.

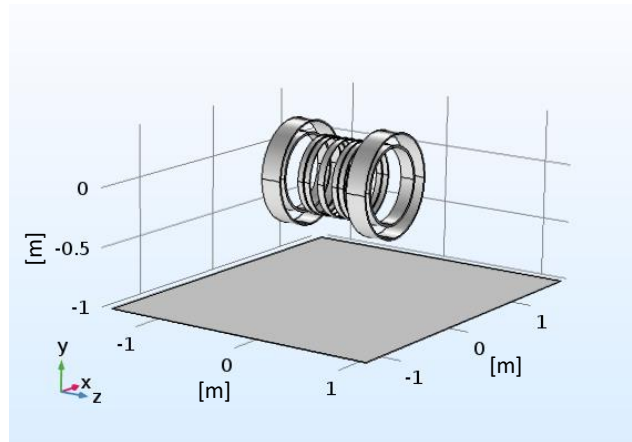


**Figure 24** - Geometry of a plate of thickness 4mm, and dimensions 3 m by 2.5 m added to the model of a seven coil actively shield MR scanner at a position of  $y = -1.0$  m within *COMSOL*.

A simulation-data analysis pipeline was generated to aid with the volume of simulations and data analysis in the investigation of linear magnetic materials. The pipeline contains elements of *COMSOL*, *MATLAB*, *Python* and *COMSOL LiveLink* with *MATLAB*. The pipeline is designed such that a user can run multiple iterations of a simulation all from a single script. This pipeline allows for simulations to be run in succession while iterating parameters within *COMSOL*.

In order to investigate the presence of a linear magnetic material the plate domain was set to a blank material in *COMSOL* and using this pipeline the magnetic susceptibility of this material was iterated over values of  $10^8$  ppm,  $10^7$  ppm,  $10^5$  ppm and 10 ppm. These values were chosen to represent materials that are extremely ferromagnetic, slightly ferromagnetic, and paramagnetic.

In order to investigate the presence of a non-linear magnetic material, the material of the plate was defined as iron and the constitutive relationship was interpolated from an assumed **BH** curve as shown in Figure 25. In *COMSOL*, a second ‘Ampere’s Law’ from the ‘Magnetic Fields, mf’ package is required in order to define the constitutive relation of the material to come from the **BH** curve.

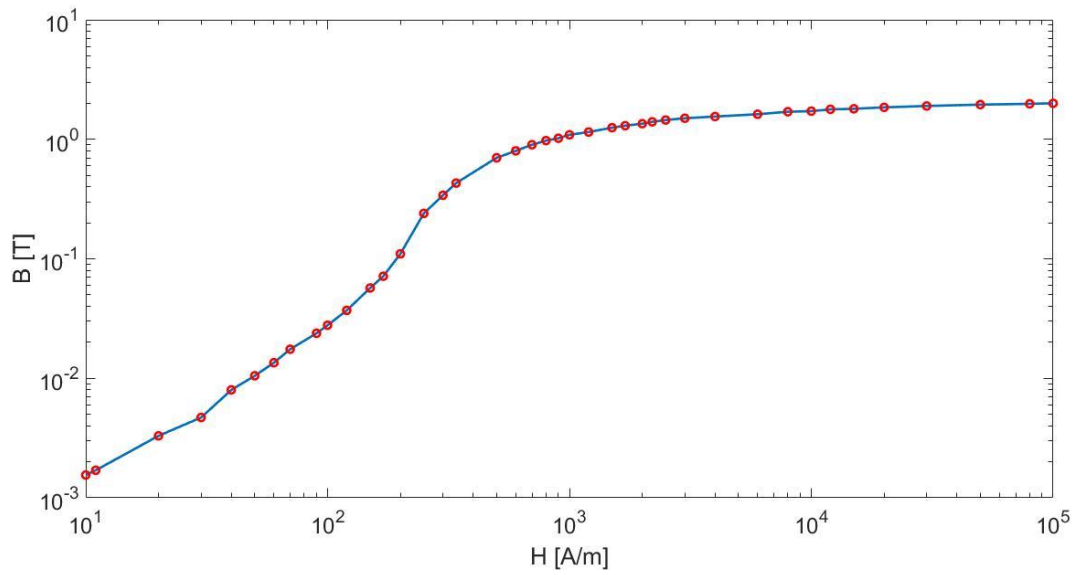


**Figure 25** - An example B-H curve, showing the magnetic flux density,  $B$ , as a function of magnetic field strength,  $H$ , for a hypothetical material. In this case the magnetic flux density is a non-linear function of applied magnetic field and ‘saturates’ at 2 T. This is the point where further increase of the applied field will not result in a change in the magnetic flux density.

## E.2.2 Results

Figure 26 shows the field experienced by the plate due to the magnet. Figure 27 shows an example of how that field changes due to the presence of magnetic material. In this figure the plate has a susceptibility of  $10^8$  ppm and the color axis has a maximum of 0.2 Tesla to observe magnetic flux density as the location of the plate.

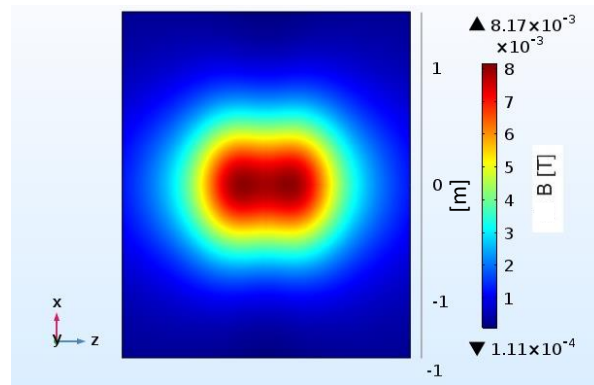


**Figure 26** – Magnet flux density profile at the location of a steel plate placed 1 m below the isocenter of a standard actively shielded MR main magnet as produced by a *COMSOL* model. The magnet consisted of seven inner coils and an additional two outer shielding coils. The current was adjusted such that the main field had a value of 0.5 T within 0.3 mT.

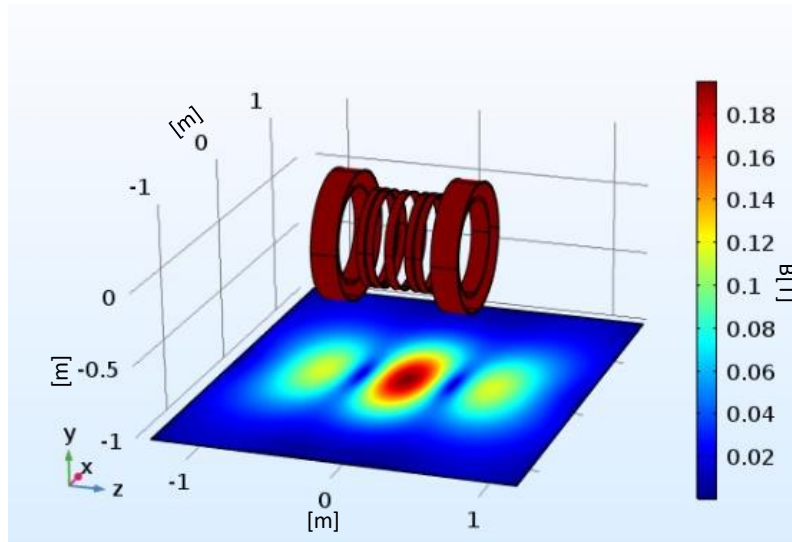


**Figure 27** – Magnet flux density profile at the location of a steel plate of magnetic susceptibility  $10^8$  ppm placed 1 m below the isocenter of a standard actively shielded MR main magnet as produced by a *COMSOL* model. The magnet consisted of seven inner coils and an additional two outer shielding coils. The current was adjusted such that the main field had a value of 0.5T within 0.3 mT. Color axis has been limited to 0.2 T to observe magnetic flux density as the location of the plate.

Figures 28-30 show the resulting change in field in the imaging region for plates of differing linear magnetic material.

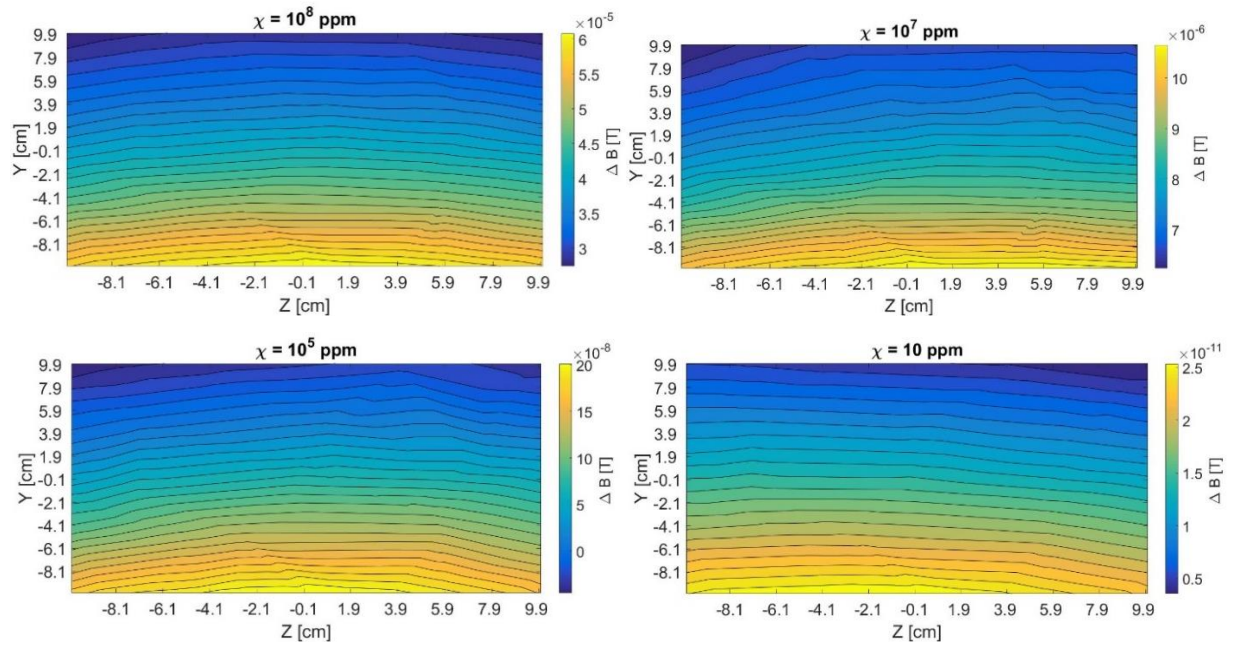


**Figure 28** – Change in magnetic flux density in the  $x = 0$ ,  $Y$ - $Z$  plane due to the presence of a linear magnetic plate of susceptibility: (top, left)  $10^8$  ppm, (top, right)  $10^7$  ppm, (bottom, left)  $10^5$ , (bottom, right) 10 ppm; at a distance of  $y = -1$  m to a standard actively shielded MR main magnet of field strength 0.5 T. Change in magnetic flux density calculated by subtracting the magnetic flux density results of the simulation without a plate from the simulation with a plate.

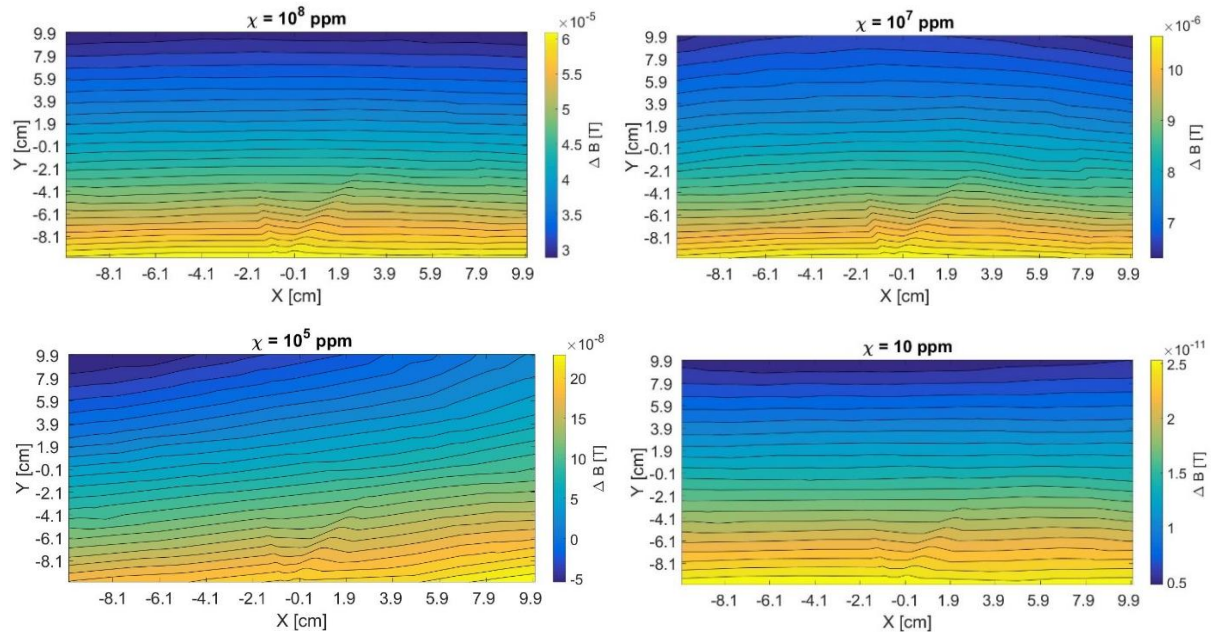


**Figure 29** - Change in magnetic flux density in the  $z = 0$ ,  $X$ - $Y$  plane due to the presence of a linear magnetic plate of susceptibility: (top, left)  $10^8$  ppm, (top, right)  $10^7$  ppm, (bottom, left)  $10^5$ , (bottom, right) 10 ppm; at a distance of  $y = -1$  m to a standard actively shielded MR main magnet of field strength 0.5 T. Change in magnetic flux density calculated by subtracting the magnetic flux density results of the simulation without a plate from the simulation with a plate.

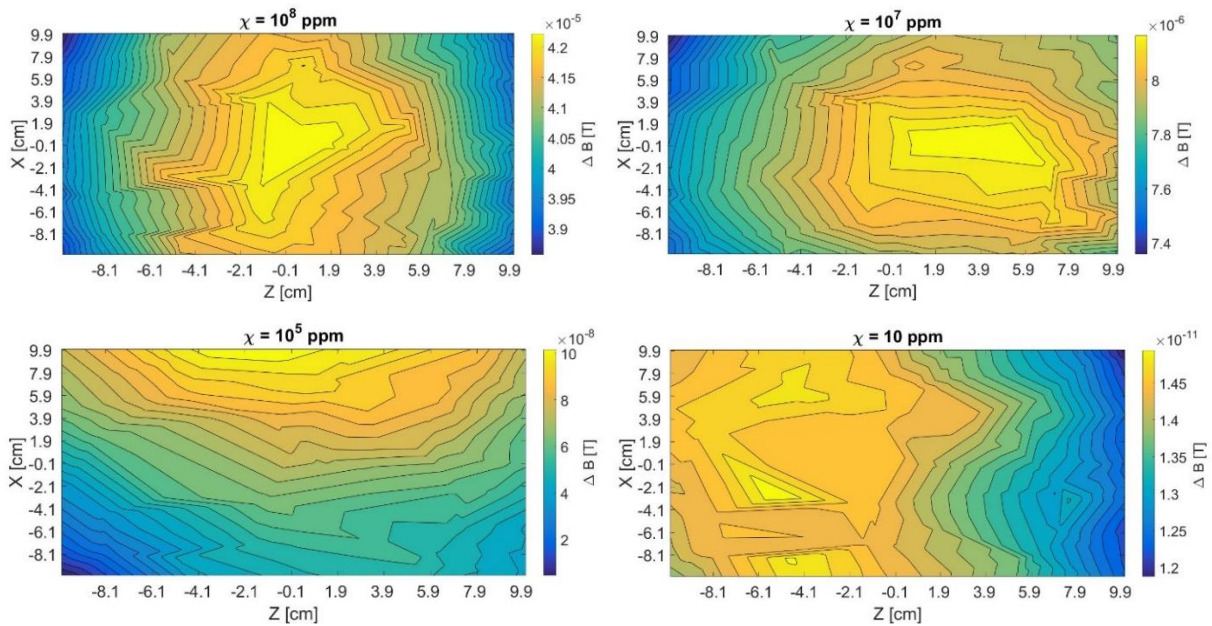


**Figure 30** - Change in magnetic flux density in the  $y = 0$ ,  $X-Z$  plane due to the presence of a linear magnetic plate of susceptibility: (top, left)  $10^8$  ppm, (top, right)  $10^7$  ppm, (bottom, left)  $10^5$ , (bottom, right) 10 ppm; at a distance of  $y = -1$  m to a standard actively shielded MR main magnet of field strength 0.5 T. Change in magnetic flux density calculated by subtracting the magnetic flux density results of the simulation without a plate from the simulation with a plate.

Figure 31 shows the resulting change in field in the imaging region for a plate of non-linear magnetic material.

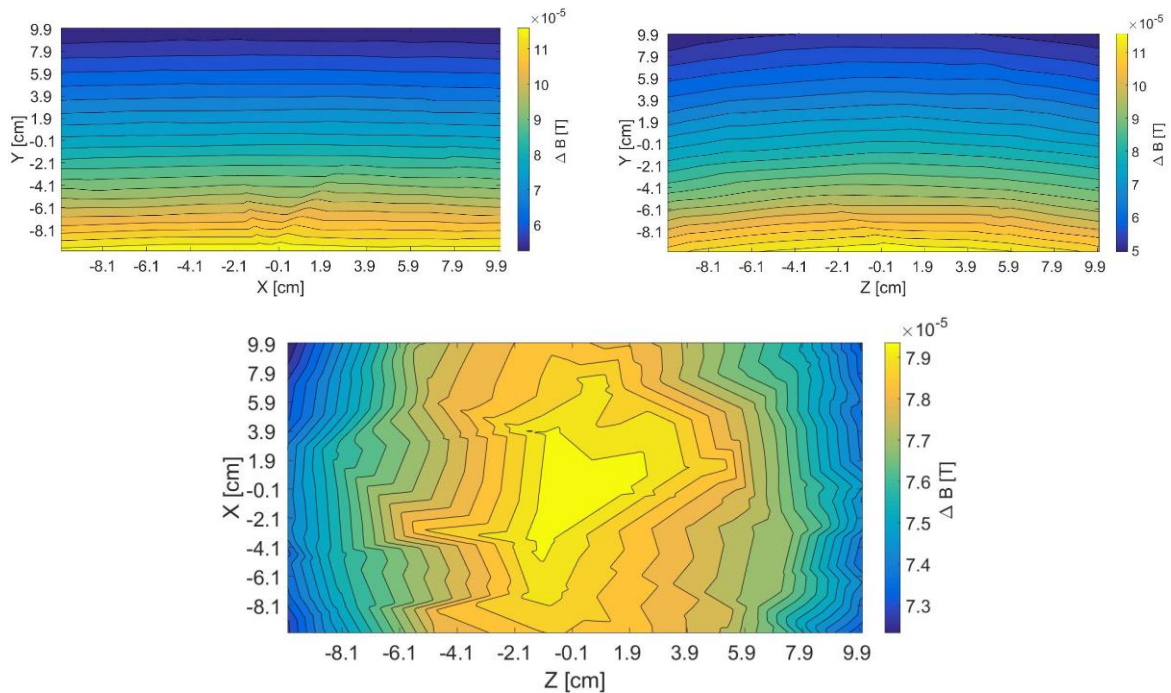


**Figure 31** - Change in magnetic flux density due the presence of a non-linear magnetic plate. (top, left)  $z = 0$ ,  $X$ - $Y$  plane (top, right)  $x = 0$ ,  $Y$ - $Z$  plane (bottom)  $y = 0$ ,  $X$ - $Z$  plane; at a distance of  $y = -1$  m to a standard actively shielded MR main magnet of field strength 0.5 T. Change in magnetic flux density calculated by subtracting the magnetic flux density results of the simulation without a plate from the simulation with a plate.

### E.3 Discussion

The percent difference between simulation results and an analytic solution for a Helmholtz coil that was simulated in *COMSOL* was less than 0.4%. A small difference was expected as the analytic solution is the solution for a perfect theoretical Helmholtz coil with infinitely small current loops. The physical properties of the simulation - ie. current applied to a physical loop in space, positional uncertainty in the simulation nodes along the  $z$  axis, etc – are the cause for this difference between the simulation data and analytic solution. As a small percent difference was expected, any simulation producing percent difference up to 1% difference would have been accepted. This pilot test produced sufficiently small differences in analytic and simulated results, and justified the use of *COMSOL* for modeling of a more realistic MR magnet.

The resulting magnetic flux density profile of the modeled MR main magnet produces a small region of homogeneity at the isocenter and that the individual coils produce local regions of increased magnetic flux density as expected. The magnetic flux density along the  $z$  axis of the magnet is symmetric about the isocenter and quickly drops as it extends to the region outside the bore, again as it should.

With a model of a MR main magnet in place, a steel plate was added to the simulation of the MR magnet to investigate the effect of different magnetic materials on the homogeneity of the field. Even a distance of 1 m, the steel plate experiences magnetic flux density from the MR magnet. The magnetic flux density profile at the location of the plate is highest at the center of the plate since it is located directly below the coils of the magnet. This magnetic flux density will induce a magnetization in the steel plate. This magnetization will induce an additional component of magnetic flux density which is the source of the field inhomogeneities presented in Figures 28-31. This effect increases as magnetic susceptibility increases and changes the magnetic flux density profile at the location of the plate. Figure 27 shows how the field profile changes, shown with a linear magnetic plate with magnetic susceptibility  $10^8$  ppm. The magnetic flux density is still highest at the center of the plate, but it is more concentrated and has a higher value than the magnetic flux density at the same location without the presence of the steel. This increased magnetic flux density will cause greater field inhomogeneities.

Four linear magnetic material plates were modeled with magnetic susceptibilities 10 ppm,  $10^5$  ppm,  $10^7$  ppm and  $10^8$  ppm. The resulting field inhomogeneity in the  $y$ - $z$  and  $x$ - $y$  plane show the magnetic flux density decrease along a gradient of  $+y$ , with a higher field inhomogeneity towards the steel plate,  $-y$ . This is consistent with the magnetization of the steel plate creating magnetic flux density as the source of the field inhomogeneities, since less inhomogeneity would be expected at location further away from the plate. The magnitude of this field inhomogeneity is proportional to magnetic susceptibility and ranges from  $10^{-11}$  to  $10^{-5}$  T, or  $20^{-5}$  to 200 ppm. This is also expected as increased magnetic susceptibility causes increased magnetization. The increased magnetization causes higher magnetic flux density which results in larger field inhomogeneities. Despite being unnecessary to shim for inhomogeneities in the  $20^{-5}$  ppm range, these plots allow for an appropriate shim to be modeled to account for the profile of the inhomogeneity, most relevant to cases where inhomogeneity reaches the 0.01 ppm or higher. In

$Y$ - $Z$  plates with magnetic susceptibilities  $10^7$  ppm and 10 ppm, and in  $X$ - $Y$ , the plate with magnetic susceptibility  $10^5$  ppm, all have slight asymmetries to the field inhomogeneity profile. This is not expected. Since the magnetic is symmetric about the isocenter, and the plate is also symmetric about the isocenter, it is expected that the field inhomogeneity would be symmetric about the isocenter; as is the case with all other profiles. This asymmetry could potentially be the result of unique magnetization profiles of the plate due to slight variance in the spatial windings of the coils of the magnet, and could thus accurately be representing the real life inhomogeneities of these specific cases. However, it is also a possibility that these small asymmetries are due to errors in the simulation or the result of gridding and plotting parameters.

In the  $x$ - $z$  plane, for a magnetic susceptibility of  $10^8$  ppm, the field inhomogeneity is highest in the center and decreases radially. Looking at the  $\mathbf{B}$  field at the plate in Figure 27, the magnetic flux density is also highest in the center of the plate and radially decreasing. The field inhomogeneity seen for the plate of magnetic susceptibility of  $10^8$  ppm in the  $x$ - $z$  plane is consistent with this result. The resulting field inhomogeneity for a magnetic susceptibility of  $10^7$  ppm follows this trend with a slight distortion in the right half of the imaging region. This asymmetry could again be the result of unique magnetization profiles of the plate due to slight variance in the spatial windings of the coils of the magnet, or due to errors in the simulation or the result of gridding and plotting parameters. For magnetic susceptibilities  $10^5$  ppm and 10 ppm, the trend seen for the case of the plate of magnetic susceptibility  $10^8$  ppm is completely lost. It is not obvious if this is due to a computational error or if the field inhomogeneity caused by the plate is not sufficient in this plane to be observed for susceptibilities this low.

For the case of a platform of non-linear magnetic material, the field inhomogeneity along  $y$ - $x$  and  $y$ - $z$  is a gradient with higher field inhomogeneity as you move towards the steel plate, with a maximum field inhomogeneity of 0.1 mT. This is the approximately the same magnitude of field inhomogeneity as per the plate of  $10^8$  ppm as expected since a non-linear magnetic material would have similar properties to a plate of extremely high magnetic susceptibility. The field inhomogeneity in  $x$ - $z$  is highest at isocenter, with a maximum inhomogeneity of 1 mT, decreasing radially, again matching the results of the plate of susceptibility  $10^8$  ppm.

## E.4 Conclusion

The objective of this project was to simulate the effects that relatively large amounts of magnetic material, placed outside a realistic model of an MRI magnet, would have on the homogeneity of that magnet. The field inhomogeneity due to the steel plate within the imaging region was shown to be a linear gradient along  $x$ - $y$  and  $y$ - $z$  with a maximum field inhomogeneity of 0.1 mT, 200 ppm, in the case of a non-linear magnetic steel. In  $x$ - $z$ , the inhomogeneity was radially decreasing with a maximum inhomogeneity of 1 mT, 2000 ppm, at the isocenter in the case of a non-linear magnetic steel. The inhomogeneities caused by this plate are far too large for proper magnetic resonance imaging and must be corrected with passive shimming if such a shielding method is used.

## Appendix F: Investigation of Systematic Errors in NMR Field Probes

Similar to Appendix E, this Appendix describes a project related to, but separate from the primary thesis work described in Chapters 2 through 4. The objective of this project was to simulate the effects that different construction materials would have on the field uniformity within specialized nuclear magnetic resonance (NMR) magnetic field probes. This project was conducted as part of an industry-sponsored internship with the same industry partner as for the work in Appendix E. The objective of the industry partner was to understand the effect that different construction parameters could have on a magnetic field measurement system they were developing, and to optimize the fabrication of that system.

The reason this Appendix is included in this thesis is that this project also leveraged many of the same simulation tools as those developed to model magnetic forces on medical devices. To the extent that these tools become validated for the application described in this appendix, this project would serve to further support the validity of the tools for use in the medical device application described in Chapters 2 through 4. It was anticipated that much more experimental data would be acquired through the process of the construction and testing of this field measurement system, and thereby provide much stronger validation data for the simulation methods than what could have been obtained in the work described in Appendix E.

Nuclear magnetic resonance (NMR) field probes are small devices used together with a NMR detection system to measure magnetic field strength at specific points in space [68]–[70]. They allow the detection of a NMR free induction decay (FID) signal from a small sample within the detector, and the instantaneous change in frequency of that FID is related to the instantaneous magnetic field over the small sample [70]. The detectors are typically copper wire-wound solenoids around a small glass vial filled with water [69,70]. Chemical compounds, such as copper sulphate, are added to the water to decrease T1 (the longitudinal relaxation time constant of magnetization [70]). Decreased T1 allows for more rapid recovery of the system following each measurement, thereby allowing faster sampling and more signal averaging over time.

Accurate to the order of ppm for magnetic fields above 0.05 T, NMR probes can practically measure with a spatial resolution on the order of a millimeter [68]–[71].

One challenge in NMR field probe design is to maximize the field uniformity over the water sample within the probe. With increasing field variation over the sample there is a more rapid loss of signal within each measurement, due to decay of the net transverse magnetization by dephasing. Minor susceptibility differences between the air, the glass, the copper, and the water can cause small but significant field variations over the sample, thereby decreasing the effectiveness of the probe. Susceptibility matching an encapsulating material formed around the entire sample and probe has been shown in literature to reduce this field variation [72], but this procedure has not been systematically investigated. Additionally, the presence of materials with nonzero magnetic susceptibility, such as the encapsulating epoxy, will cause a net field offset and shift in the NMR signal which must be understood and taken into account when interpreting the measured fields.

In addition to the effect of overall susceptibility matching with the epoxy, there is an additional potential for field broadening due to magnetic susceptibility boundaries caused by the presence of air bubbles or voids within the epoxy. These small air bubbles or voids, which occur commonly in epoxy during the encapsulation process, can be thought of as inhomogeneous regions of zero magnetic susceptibility. These voids become a source of both field broadening and field offset over the sample. The effect of air bubble or void formation during the encapsulation process of NMR probe construction has yet to be systematically analyzed and discussed in the literature.

This Appendix seeks to investigate and quantify the above effects with the objective of optimizing NMR field probe design and construction. As part of an industry-sponsored internship project (MITACS Accelerate program, partnered with Synaptive Medical Inc., Toronto, Ontario, Canada), the systematic uncertainties involved in the construction and use of a spatial array of NMR field probes for magnetic field measurements at 0.5 T were studied. A prototype probe array was constructed in collaboration with the industry sponsor; however, physical testing with the system was delayed and therefore experimental validation of the system could not be included in this thesis.

## F.1 Methods

All design, modeling and simulations were performed in *COMSOL Multiphysics* using the ‘Magnetic Fields, No Current (mfnc)’ package.

Three NMR field probe constructions were modeled for the purposes of this investigation. One contained a glass vial containing a sample of copper sulphate doped water, the next a 4-turn copper solenoid with wire thickness 0.225 mm, and the last contained both the glass vial complete with sample and the copper solenoid. Figure 33 below shows an example of a probe construction that is the basis of the modeling variations investigated and described in the following paragraphs.

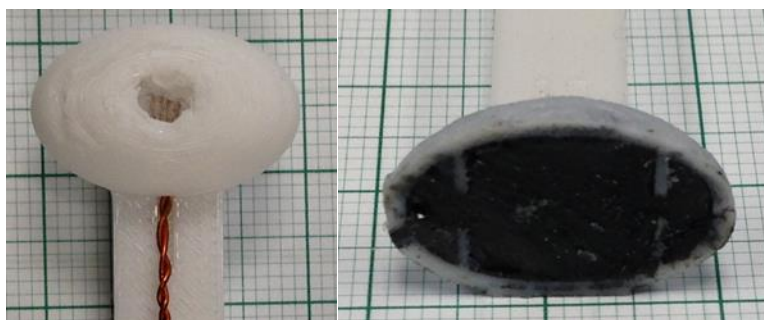


**Figure 32** - Nuclear magnetic resonance (NMR) field probe. Field probe contains copper solenoids that wrap around glass vials filled with copper sulphate doped water samples. The sample and solenoid are held in place in an epoxy filled ellipsoid. (Left) Field probe shown with the copper solenoid leads exiting the epoxy ellipsoid that contains the solenoid and sample vial. (Right) NMR field probe cut in cross section showing the epoxy-filled region.

The glass vial was modeled to be a hollow cylinder of outer radius 1.4 mm, wall thickness 0.2 mm and height 15 mm. The hollow cylinder was constructed in the geometry by a combination of two cylinder domains and the ‘Difference’ function, and material was set to glass (quartz). The copper sulphate doped water sample was modeled with another cylinder geometry - radius 1.2 mm, height 15 mm - which filled the hollow glass cylinder and this domain was set to water. The magnetic susceptibility of this material was changed to -9.04 ppm to represent the magnetic susceptibility of the doped sample [38], [44]. The 4-turn copper solenoid was modeled using the

‘Helix’ geometry with major radius 1.626 mm, minor radius 0.225 mm, axial pitch 0.9 mm and no radial pitch. A 0.001 mm gap was left between the copper solenoid domain and the vial domain in order to avoid meshing errors. The center of the solenoid was positioned to align with the center of the glass vial. The material of the solenoid domain was set to copper, and the magnetic susceptibility was changed to -9.57 ppm as *COMSOL* initially defined copper as having a magnetic susceptibility of 0 [38], [44], [45].

All probe variations had their respective elements encapsulated by an epoxy ellipsoid. The ellipsoid was created in the geometry with major and minor radii of 15 and 10 mm, respectively. This geometry was fixed on the existing probe prototypes already fixed by the industry partner. A blank material was added to this domain and the relative permeability of this domain was varied as described in F.1.1.1.

All simulations were performed in a static magnetic field of 0.5 T which was employed using ‘Background Magnetic Field – Reduce field –  $H_x = 0.5 / \mu_0_{const}$ ,  $H_y = H_z = 0$ ’ within ‘Magnetic Fields, No Current (mfnc)’. The field strength was chosen to match the magnet with which the field array was to be ultimately tested and used. The entire simulation was constructed within a spherical infinite element domain of air. Meshing of the probe elements was performed with free tetrahedrals, while the outer domains of the spherical infinite element domain employed a swept mesh.

Simulation data was exported from the simulations and all data analysis was performed in *MATLAB*.

### F.1.1 Methods for Investigation of Effects due to the Susceptibility of Epoxy

In order to investigate the effects due to variations in epoxy susceptibility, and thus determine an optimal magnetic susceptibility of epoxy, three NMR probes were modeled (see Figure 33).

- Probe i) was modeled containing the glass vial, complete with sample, surrounded by the copper solenoid.
- Probe ii) was modeled containing the glass vial, complete with sample, but was lacking the copper solenoid.

- Probe iii) was modeled containing only the copper solenoid.

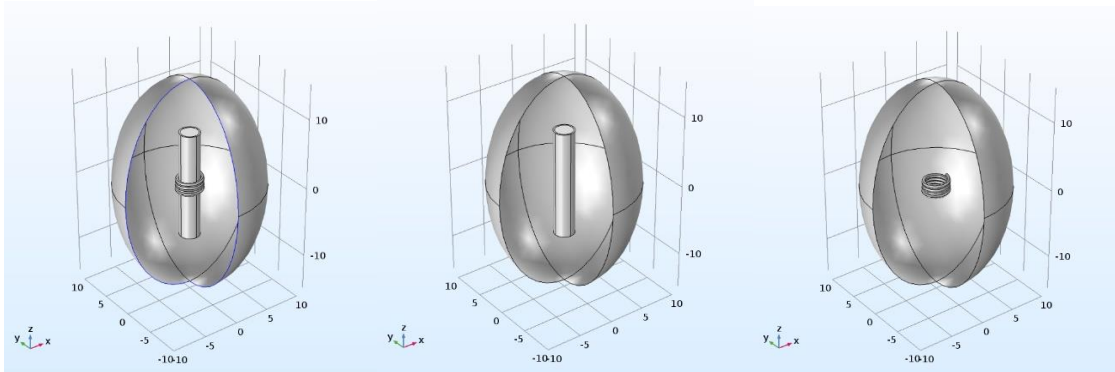


**Figure 33** – *COMSOL* geometry of three NMR probe designs. Within an epoxy ellipsoid: (from left to right) probe i) was modeled with a glass vial containing a sample of copper sulphate doped water, surrounded by a 4 turn copper solenoid of wire thickness 0.225 mm; probe ii) was modeled with only a glass vial containing a sample of copper sulphate doped water; probe iii) was modeled containing only a 4 turn copper solenoid with wire thickness 0.225 mm.

For each probe model, a simulation was run with the epoxy material defined with a specific value of relative permeability. Within *MATLAB*, the magnitude of the  $\mathbf{B}$  field within the water domain was isolated. The weighted variance,  $s_w^2$ , of this data was calculated using the sensitivity profile of the solenoid, Figure 34, as a weighting factor. The sensitivity profile of the solenoid is defined as the sensitivity of the solenoid to the measurement of magnetic flux density at any given point within the sample vial. By the Principle of Reciprocity, the detection sensitivity profile of the solenoid has the same form as the field produced by that solenoid at any point in space were the solenoid to be carrying 1 Ampere of current. This sensitivity profile was produced in *MATLAB* using an elements array and Biot-Savart law to model the field due to a solenoid of the same dimensions of the solenoid modeled in *COMSOL*. The magnetic flux density was found at every point within the isolated data set. Normalizing to the maximum magnetic flux density creates the sensitivity profile. This sensitivity profile was used to produce a weight,  $w_i$ , for each value of  $\mathbf{B}$  in the data set,  $x_i$ . The weighted average,  $\bar{x}_w$ , of the data was then computed using equation (F.1). The weighted average along with the weights is then used to calculate the weighted variance, equation (F.2).

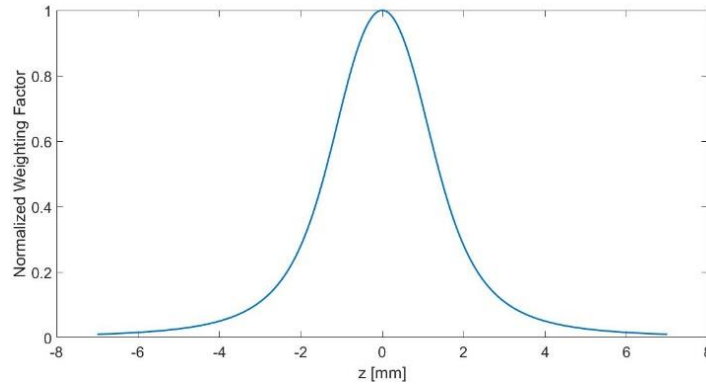


**Figure 34** – Sensitivity profile of a solenoid modeled within *COMSOL* along the  $z$ -axis. Sensitivity profile produced by solving for the magnetic flux density using Biot-Savart law at every data point with an elements array in *MATLAB*. Normalizing to the maximum magnetic flux density gives the sensitivity profile. This sensitivity profile was used to produce a weight,  $w_i$ , for each value of  $B$  in the data set,  $x_i$ .

$$\bar{x}_w = \sum_{i=1}^N \frac{w_i x_i}{\sum_{i=1}^N w_i} \quad (\text{F.1})$$

$$s_w^2 = \frac{\sum_{i=1}^N w_i (x_i - \bar{x}_w)^2}{\sum_{i=1}^N w_i} \quad (\text{F.2})$$

The field broadening,  $\sigma$ , is then defined as the square root of the weighted variance.

$$\text{field broadening } (\sigma) = \sqrt{s_w^2} \quad (\text{F.3})$$

For each probe model, simulations were performed using susceptibilities of epoxy from -20 to 1.2 ppm. Optimal susceptibility for epoxy was chosen as that which minimized field variation over the sample volume.

Although the main concern for field probe performance is field broadening, the epoxy will also in general create a net field offset over the sample. This effect does not need to be minimized in probe design, but it does need to be accounted for in interpreting the results when using a probe. To investigate and characterize the field offset due to the epoxy encapsulation, the data from the simulations for probe i) was taken and the field offset was calculated by subtracting the weighted mean of the  $B$  field data from the applied field of  $B = 0.5 T$ ; equation (F.4).

$$\text{field offset} = 0.5 T - \bar{x}_w \quad (\text{F.4})$$

## F.1.2 Methods for Investigation of Effects Due to Voids Within the Epoxy

In order to investigate the effect of a void within the epoxy, probe i) from F.1. was used. A single 1-mm spherical void geometry (“air bubble”) was investigated and added to the model with the material of that domain was set to air.

Numerical simulations were evaluated varying the positions of the air bubble and the field variation was calculated using the same method as F.1.1 for each position. First, the void was placed at multiple positions in the  $z=0$  plane at a constant radial distance of 5 mm with respect to the center of the sample ( $x,y=0$ ), at angles of  $0^\circ$ ,  $45^\circ$ ,  $90^\circ$ ,  $135^\circ$ ,  $180^\circ$ ,  $225^\circ$ , and  $270^\circ$  (Figure 35).

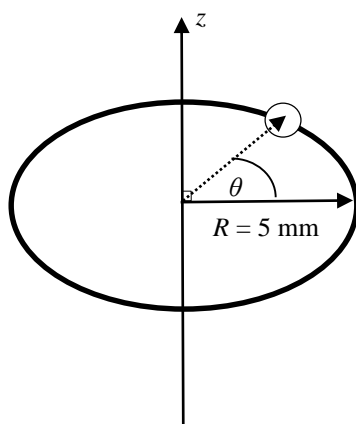


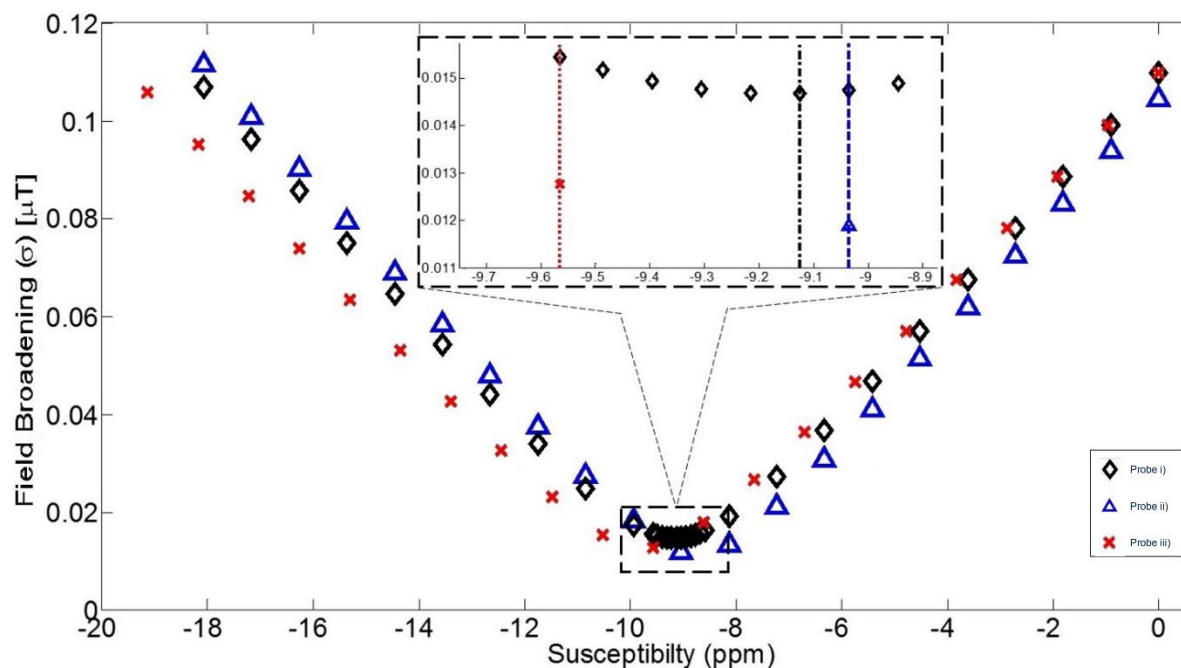
**Figure 35** – Path of an air bubble of spherical radius 1 mm moving along a circle of radius of 5 mm fixed in the  $z = 0$ ,  $X$ - $Y$  plane at an angle,  $\theta$ , within an NMR probe. *COMSOL* simulation computed for angles of  $0^\circ$ ,  $45^\circ$ ,  $90^\circ$ ,  $135^\circ$ ,  $180^\circ$ ,  $225^\circ$ , and  $270^\circ$ .

Next, the void was placed along 21 positions in  $z$ , from  $z = -10$  to  $10$  mm, at a fixed location of  $x = 5$  mm,  $y = 0$  mm in the  $X$ - $Y$  plane. All simulations were computed with a value of  $-9.5658$  ppm for the magnetic susceptibility of epoxy.

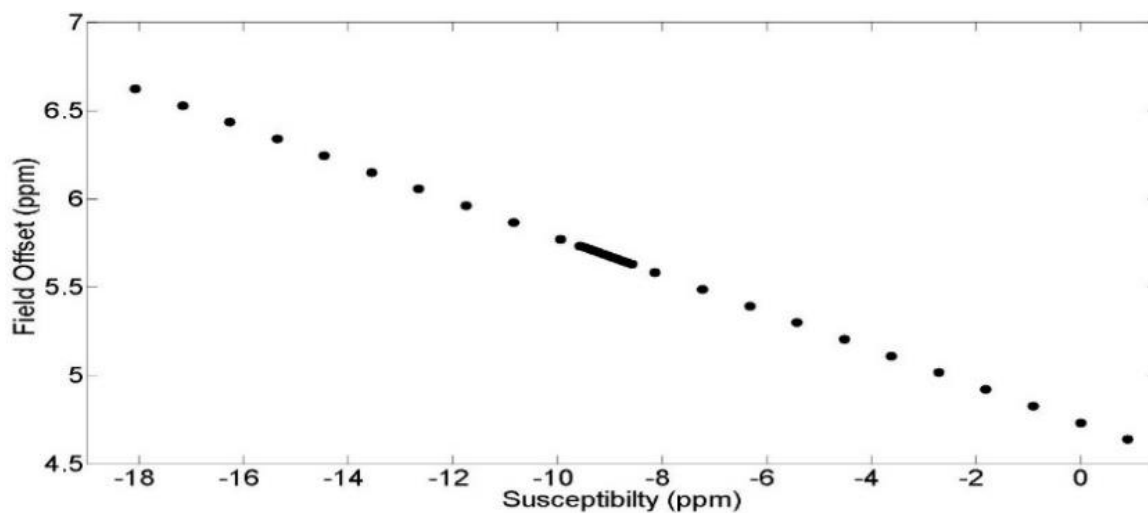
## F.2 Results

Figure 36 and Figure 37 show the resulting field variation and field offset as a function of varying epoxy magnetic susceptibility, respectively. The field variation is observed to be minimized for a susceptibility of approximately  $-9$  ppm. For the optimal susceptibility range of approximately  $-9$  ppm, the field offset within the sample is approximately  $5.7$  ppm.

Figure 38 shows the resulting field broadening due the void at the various locations within the probe.



**Figure 36** - Field broadening as a function of magnetic susceptibility of epoxy for the three NMR probe models modelled. Within an epoxy ellipsoid: Probe i) was modeled with a glass vial containing a sample of copper sulphate doped water, surrounded by a 4 turn copper solenoid; Probe ii) was modeled with only a glass vial containing a sample of copper sulphate doped water; Probe iii) was modeled containing only a 4 turn copper solenoid. The value of magnetic susceptibility that resulted in a minimum field broadening is represented by a vertical black, blue and red line for probes i), ii) and iii) respectively.



**Figure 37** - Field offset as a function of magnetic susceptibility of epoxy for NMR Probe i). Within an epoxy ellipsoid, Probe i) was modeled with a glass vial containing a sample of copper sulphate doped water, surrounded by a 4 turn copper solenoid.

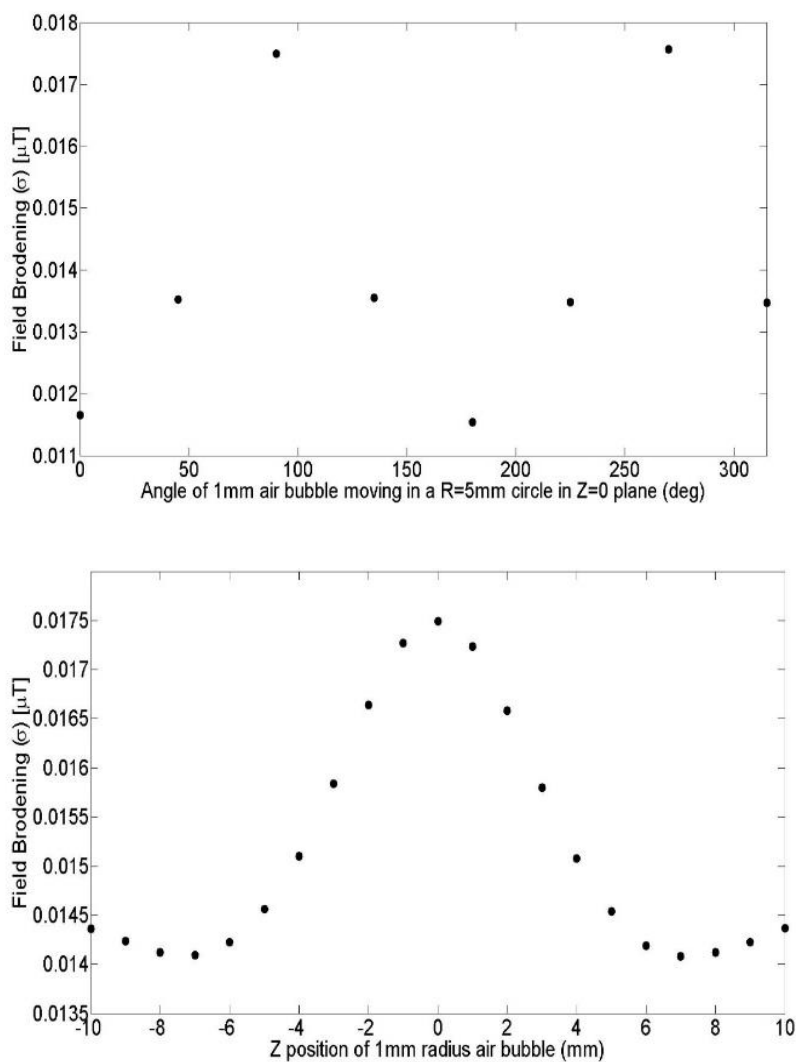


**Figure 38** – Resulting field broadening due to a void at various locations within a NMR probe. The NMR probe was modeled with a glass vial containing a sample of copper sulphate doped water, surrounded by a 4 turn copper solenoid, all encapsulated in epoxy ellipsoid (i.e. “Probe i”). (Top) Resulting field broadening due to spherical void of radius 1 mm moving along a circle of radius of 5 mm fixed in the  $z = 0$ ,  $X$ - $Y$  plane at an angle of  $0^\circ$ ,  $45^\circ$ ,  $90^\circ$ ,  $135^\circ$ ,  $180^\circ$ ,  $225^\circ$ , and  $270^\circ$ . (Bottom) Resulting field broadening due to the spherical void of radius 1 mm at different  $z$  positions while remaining fixed at a position of  $x = 5$  mm,  $y = 0$  mm in the  $X$ - $Y$  plane.

## F.3 Discussion

It was found that the optimal susceptibility for the epoxy encapsulation (approximately -9 ppm) lies between the susceptibility of the doped water sample and copper. This result is perhaps not surprisingly in that it is consistent with the hypothesis that minimum field broadening will occur in a uniform magnetic environment. When the epoxy susceptibility is optimized, there is a ten-fold improvement in field broadening compared to having the probe in air alone (i.e. no encapsulation). This basic effect is well-known and is the reason probe encapsulation is commonly used and reported in the literature [72]. The results presented here go further, specifically demonstrating that field broadening is doubled when susceptibility varies from the optimal value by as little as 2 ppm. The small variation in the susceptibility of the epoxy significantly affects probe performance of the probe and must be considered when optimizing the construction of the probe. This work allows one to rationally choose the tolerance in the susceptibility of the encapsulation material for a probe.

In addition to a field broadening, a field offset was expected to be present due to the epoxy and this was represented in the simulation results. The absolute field offset was observed to decrease as susceptibility increases. A field offset does not degrade probe performance as long as it is taken into account when interpreting the field results. It is therefore effectively a straight-forward matter of calibration. Broadening cannot be calibrated for; therefore, the main concern in the construction of the probes should be to susceptibility match the epoxy to the optimal value regardless of the field offset incurred.

Introducing an air bubble at a constant  $(x,y)$  value but at varying positions in  $z$  shows that the broadening is not surprisingly most severe when the bubble is closest to the solenoid. The effect of a single void or “air bubble” was shown to result in field variations that at worst were more than approximately twice the largest field variations caused by poor susceptibility matching of the epoxy. Even in the best situation examined, a single void will cause a field variation of 5 times that of optimally matched epoxy. This indicates that avoiding voids in the encapsulation process is of paramount importance. Methods currently used to eliminate voids during construction such as vacuum potting are critical and additional efforts to systematically ensure the successful elimination of voids are warranted. Without void elimination measures, the

effectiveness of susceptibility-matched epoxy is severely compromised. The effect of multiple voids within a probe has not yet been investigated.

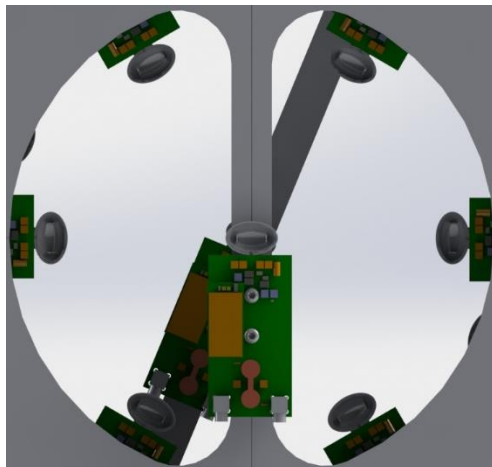


**Figure 39-** Computer design of an array of nuclear magnetic resonance (NMR) field probes that make up an effective ‘field camera’ which is used to acquire accurate spatial variation of time varying fields in MR systems at discrete points in space. Seven probes can be seen here (6 around the circumference of the circle and one at the centre).

In the process of conducting this work, several NMR probes were constructed and sent to the industry partner (Synaptive Medical Inc.). The epoxy ellipsoids were 3D-printed and vacuum potted with epoxy 3150, and catalyst 150 from Epoxy Etc. (<http://www.epoxies.com/>). Epoxy was mixed and susceptibility matched using titanium powder as specified by the industry partner. The field camera (see Figure 39 above) constructed from the probes has been constructed and tested; however, at the time of writing these data were not yet available.

## F.4 Conclusion

The systematic errors within NMR probes were investigated and it was shown that: (1) epoxy susceptibility should be matched to the other construction materials used, and (2) every effort should be expended to minimize the presence of voids or “air bubbles” during encapsulation.

## Curriculum Vitae

**Name:** Spencer Baird Parent

**Post-secondary Education and Degrees:** Western University  
London, Ontario, Canada  
2010-2014 B.Sc.  
Honours Specialization Medical Physics

Western University  
London, Ontario, Canada  
2014-Present M.Sc.  
Medical Biophysics

**Honours and Awards:** Deans Honour List  
2010

**Related Work Experience:** Summer Research Student  
Western University  
2014

**Conference Proceedings:** “Analytic Validation of a Computational Model of Magnetic Force in Linear Magnetic Materials”  
Abstract Submission  
International Society of Magnetic Resonance in Medicine, (2017)  
Hawaii, USA

“Computational Analysis of Main Field Homogeneity in Presence of

Non – Linear Magnetic Steel”

Abstract Submission

International Society of Magnetic Resonance in Medicine, (2017)

Hawaii, USA

“Investigation of Systematic Errors in NMR Field Probes”

Poster Presentation

International Society of Magnetic Resonance in Medicine, (2015)

Singapore

“Investigation of Systematic Errors in NMR Field Probes”

Poster Presentation

London Health Research Day, (2015)

London, Ontario

“Evaluation of orthopedic device compatibility for 1.5 and 3-Tesla MRI”

Oral Presentation

Western University Physics Undergraduate Conference, (2014)

London, Ontario